National Technical University of Athens
School of Electrical and Computer Engineering
Division of Electromagnetics, Electrooptics and Electronic Materials

Electromagnetic Superradiation in Cylindrical Geometries

Diploma Thesis

Konstantinos Delimaris

Supervisor: Constantinos Valagiannopoulos
Assistant Professor, National Technical University of Athens

Athens, May 2025

National Technical University of Athens
School of Electrical and Computer Engineering
Division of Electromagnetics, Electrooptics and Electronic Materials

Electromagnetic Superradiation in Cylindrical Geometries

Diploma Thesis

Konstantinos Delimaris

Supervisor: Constantinos Valagiannopoulos
Assistant Professor, National Technical University of Athens

Approved by the examination committee on May 30, 2025.

Constantinos Valagiannopoulos	Elias Glytsis	Anna Tasolamprou
.....	.....	.....
Assistant Professor School of ECE N.T.U.A.	Professor School of ECE N.T.U.A.	Assistant Professor Department of Physics U.O.A.

Athens, May 2025

National Technical University of Athens
School of Electrical and Computer Engineering
Division of Electromagnetics, Electrooptics and Electronic Materials

Περίληψη

Διαπιστώνεται ότι κακοί ισοτροπικοί ακτινοβολητές (γραμμικές πηγές), τόσο TM αλλά και TE πόλωσης, ενισχύουν σημαντικά τη ραδιοεκπομπή τους όταν τοποθετούνται εσωτερικά κυλινδρικών συνόρων που αποτελούνται από πλασμονικά (plasmonic) κελύφη ή από σωληνοειδείς μεταεπιφάνειες, οι οποίες μπορούν να κατασκευαστούν με υλικά που έχουν χρησιμοποιηθεί σε προηγούμενες εργασίες. Τέτοιες διεγέρσεις επιτρέπουν την αναλυτική αντιμετώπιση του προβλήματος, ενώ παράλληλα προσφέρουν σημαντική φυσική διαίσθηση για τη συμπεριφορά των διατάξεων. Ο παραμετρικός χώρος εξετάζεται εκτενώς, με σκοπό την εξαγωγή των βέλτιστων δομικών και υλικών χαρακτηριστικών κάθε εξεταζόμενης διάταξης. Στις περισσότερες από τις βέλτιστες σχεδιάσεις, η θέση του εκπομπού είναι τέτοια ώστε να προσαρμόζει την αλληλεπίδραση μεταξύ πολλαπλών εισερχόμενων και εξερχόμενων ρυθμών, με αποτέλεσμα την επίτευξη ισχυρών ομοιοκατευθυντικών ή διπολικών διαγραμμάτων ακτινοβολίας, διαφορετικά για κάθε πόλωση. Τα παρατηρούμενα χαρακτηριστικά ακτινοβολίας κάθε επιλεγμένης σχεδίασης επιβεβαιώνονται με χρήση λογισμικού προσομοίωσης (COMSOL Multiphysics). Οι παρουσιαζόμενες υπερακτινοβολούσες (superradiating) διατάξεις μεταφέρουν την έννοια της φωτονικής υπεραντινοβολίας (superradiance) στην κλασική ηλεκτροδυναμική, αξιοποιώντας τα αναπτυσσόμενα είδωλα των πηγών για την επίτευξη ισχυρών εκπομπών και για τις δύο πολώσεις ταυτόχρονα, παρά το γεγονός ότι περιλαμβάνουν μόνο ένα ενεργό στοιχείο. Οι ακτινοβολίες που παρατηρούνται όχι μόνο είναι ισάξιες, αλλά συχνά υπερτερούν εκείνων που έχουν αναφερθεί σε προηγούμενες εργασίες, ενώ οι κυλινδρικές γεωμετρίες παρουσιάζουν μικρότερη ευαισθησία σε μη τοπικά φαινόμενα και είναι ευκολότερες στην κατασκευή σε σύγκριση με τις παραδοσιακές πλασμονικές κεραίες. Οι παραπάνω ιδιότητες καθιστούν τις προτεινόμενες διατάξεις επιθυμητές, καθώς μπορούν να χρησιμοποιηθούν ως υπεραποδοτικά στοιχεία σε πληθώρα οπτικών εφαρμογών, που εκτείνονται από το σχεδιασμό στοιχειοκεραιών και την ασύρματη μεταφορά ενέργειας στο μακρινό πεδίο έως τη κατασκευή βιοαισθητήρων και σχημάτων αναλογικής επεξεργασίας σήματος βασισμένα στην πόλωση. Επιπλέον, η παρούσα εργασία μπορεί να επεκταθεί με την προσθήκη μη γραμμικοτήτων στις κυλινδρικές μεταεπιφάνειες, προκειμένου να κατασκευαστούν στοιχεία μνήμης με μειωμένη ευαισθησία στο θόρυβο.

Λέξεις - Κλειδιά: Ηλεκτρομαγνητική θεωρία, Φωτονική, Αντίστροφη σχεδίαση, Μεταεπιφάνειες, Νανοσωλήνες, Ηλεκτρομαγνητικές αλληλεπιδράσεις, Ασύρματη μεταφορά ισχύος.

Abstract

Poor isotropic emitters (line sources), of both TM and TE polarization, are found to substantially enhance their radiative power when located internally to cylindrical boundaries involving plasmonic shells or tubular metasurfaces that can be constructed using materials that have been utilized in previous works. Such excitations allow for the analytical treatment of the problem while also providing important physical intuition for the behavior of the setups. The parametric space is extensively searched, in order to extract the optimal structural and textural characteristics of each studied configuration. In most of the optimal designs, the placement of the antenna tailors the interference between multiple in-going and out-going modes to give strong omnidirectional or bipolar patterns, different for each wave polarization. The observed radiation characteristics of each of the selected designs are validated using a commercial electromagnetic solver (COMSOL Multiphysics). The reported superradiating setups carry over the concept of photonic superradiance to classical electromagnetics by utilizing the developed source images in achieving powerful emissive responses for both polarizations concurrently, despite incorporating just a single active element. Not only are these responses on par with, or even greater than the ones reported in previous works but the cylindrical geometries also are less sensitive to nonlocal effects and are easier to fabricate compared to traditional plasmonic antennas. The aforementioned properties make the proposed configurations desirable, since they can be employed as ultra-efficient components in a plethora of optical applications spanning from array design and far-field wireless power transfer to radiative biosensing and polarization-enabled analog signal processing. Moreover, this work can be extended by adding nonlinearities to the cylindrical metasurfaces so as to construct memory elements having suppressed vulnerability to noise.

Keywords: Electromagnetic theory, Photonics, Inverse design, Metasurfaces, Nanotubes, Electromagnetic interactions, Wireless power transfer.

Acknowledgements

As my journey at NTUA is coming to an end, I would like to thank my wonderful family and friends for their endless support, love and patience throughout the years. To all of you, I am forever grateful.

I would also like to express my gratitude to my advisor, Prof. C. Valagiannopoulos, for his guidance during my undergraduate studies. Our research endeavors have had an immense impact on my character and the way I approach scientific problems.

Finally, a heartfelt thank you to Dr. G. Zouros for introducing me to the world of scientific research and for the support throughout my time at NTUA.

Athens, May 2025
Konstantinos Delimaris

Contents

List of Figures

Κεφάλαιο 1

Εκτεταμένη Περίληψη στα Ελληνικά

1.1 Σκοπός της Εργασίας

Στην παρούσα Εργασία, μελετώνται δισδιάστατες ηλεκτρομαγνητικές διατάξεις που αποτελούνται από κυλινδρικά σύνορα και διεγείρονται από γραμμικές πηγές TM και TE πόλωσης. Συγκεκριμένα, ο σκοπός μας είναι η εύρεση των βέλτιστων δομικών και υλικών χαρακτηριστικών των υπό μελέτη γεωμετριών που οδηγούν σε ραγδαία αύξηση της εκπεμπόμενης ισχύος της πηγής στο μακρινό πεδίο, σε σχέση με την ισχύ που αυτή εκπέμπει όταν βρίσκεται μόνη της στον κενό χώρο. Με τον τρόπο αυτό, βρίσκουμε υπεραχτινοβολούσες (superradiating) ηλεκτρομαγνητικές διατάξεις.

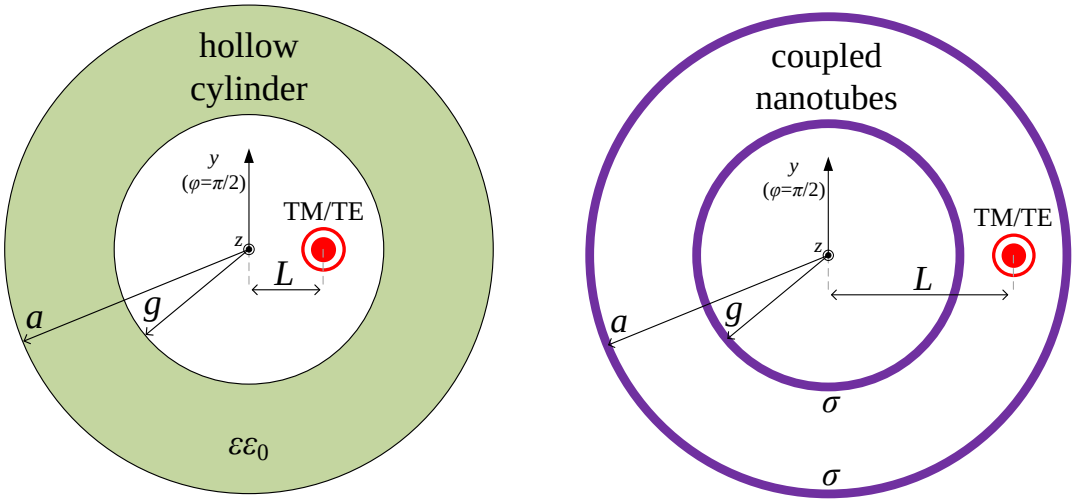

Σχήμα 1.1: Δύο αντιπροσωπευτικές διατάξεις που χρησιμοποιήθηκαν για την ενίσχυση της ακτινοβολίας της πηγής. Ορίζονται από κυλινδρικά σύνορα εσωτερικής ακτίνας $r = g$ και εξωτερικής $r = a$. (α′) Ένας μη συμπαγής κύλινδρος με κέλυφος από υλικό με μιγαδική διηλεκτρική σταθερά ε. (β′) Ένα ζεύγος συζευγμένων νανοσωλήνων με μιγαδική επιφανειακή αγωγιμότητα σ. Η πηγή τοποθετείται στο κενό.

Δύο αντιπροσωπευτικές από τις διατάξεις αυτές φαίνονται στο Σχ. 1.1. Στο Σχ. 1.1(α′), απεικονίζεται ένας μη συμπαγής κύλινδρος όπου εσωτερικά ($0 \leq r < g$) ε-

ίναι κενός και το κέλυφος του αποτελείται από υλικό μιγαδικής σχετικής διηλεκτρικής σταθεράς ε. Αντίστοιχα στο Σχ. 1.1(β′), η διάταξη αποτελείται από δύο κυλινδρικές μεταπιφάνειες ακτινών g και a αντίστοιχα, με κοινή μιγαδική αγωγιμότητα σ. Αυτές και άλλες παρόμοιες διατάξεις μελετώνται στην εργασία. Σε κάθε περίπτωση, η πηγή τοποθετείται σε χωρίο με κενό χώρο, ώστε να γίνεται μία δίκαια σύγκριση της εκπεμπόμενης ισχύος με την ισχύ που εκπέμπει η πηγή όταν βρίσκεται μόνη της. Επιπλέον, η πηγή τοποθετείται στον οριζόντιο άξονα, σε απόσταση L από τον άξονα συμμετρίας της γεωμετρίας, ή ισοδύναμα σε κυλινδρικές συντεταγμένες στη θέση $(r, \varphi) = (L, 0)$. Επιπλέον, η διέγερση είναι μονοχρωματική, με μήκος κύματος λ.

1.2 Αναλυτική Λύση των Προβλημάτων

Είναι γνωστό ότι οι γραμμικές πηγές TM πόλωσης θα παράγουν ηλεκτρικό πεδίο που έχει μόνο z συνιστώσα E_z με βάση το σύστημα αξόνων που φαίνεται στο Σχ. 1.1. Αντίστοιχα, οι TE πηγές θα παράγουν μαγνητικό πεδίο $\mathbf{H} = H_z\hat{\boldsymbol{z}}$. Για τον λόγο αυτό, θεωρούμε το μέγεθος F στην ανάλυση μας, για το οποίο ισχύει ότι $F = E_z$ στις TM περιπτώσεις και $F = H_z$ στις αντίστοιχες TE. Είναι γνωστό ότι το πεδίο που εκπέμπεται από την πηγή κατά τη z διεύθυνση ισούται με [1]:

$$F_{\text{inc}} = \sum_{n=-\infty}^{+\infty} H_n^{(2)}(k_0 \max(L, r)) J_n(k_0 \min(L, r)) e^{\mathrm{i}n\varphi}, \tag{1.1}$$

όπου $H^{(2)}$ είναι η συνάρτηση Hankel β′ είδους και J η συνάρτηση Bessel. Από την άλλη, το αντίστοιχο μέγεθος εξωτερικά της διάταξης ($a < r < +\infty$), δίνεται από:

$$F_{\text{rad}} = \sum_{n=-\infty}^{+\infty} C_n H_n^{(2)}(k_0 r) e^{\mathrm{i}n\varphi}, \tag{1.2}$$

όπου οι C_n είναι άγνωστοι μιγαδικοί συντελεστές, οι οποίοι μπορούν να βρεθούν από την εφαρμογή των συνοριακών συνθηκών. Συγκεκριμένα σε μία επιφάνεια στην οποία είναι κάθετο το μοναδιαίο διάνυσμα $\hat{\boldsymbol{n}}$, ισχύει ότι $\hat{\boldsymbol{n}} \times (\mathbf{E}_+ - \mathbf{E}_-) = \mathbf{0}$ και $\hat{\boldsymbol{n}} \times (\mathbf{H}_+ - \mathbf{H}_-) = \boldsymbol{J}_S$, όπου $\boldsymbol{J}_S = \mathbf{0}$ στην περίπτωση διηλεκτρικών, ενώ $\boldsymbol{J}_S = -\sigma\hat{\boldsymbol{n}} \times (\hat{\boldsymbol{n}} \times \mathbf{E})$ στην περίπτωση μεταεπιφανειών.

Για την εύρεση της εκπεμπόμενης ισχύος′(ανά μονάδα μήκους z λόγω της κυλινδρικής γεωμετρίας), εφαρμόζουμε το θεώρημα Poynting σε έναν κύκλο ακτίνας $r > a$ που περικλείει την πηγή:

$$P = \int_0^{2\pi} \left(\frac{1}{2} \boldsymbol{E} \times \boldsymbol{H}^* \right) \cdot \hat{\boldsymbol{r}} r \mathrm{d}\varphi, \tag{1.3}$$

Επιλέγουμε ο κύκλος αυτός να έχει άπειρη ακτίνα, ώστε να εκμεταλλευτούμε την ασυμπτωτική έκφραση των συναρτήσεων Hankel για μεγάλα ορίσματα [2] καθώς και το γεγονός ότι στο μακρινό πεδίο, η εκπεμπόμενη ακτινοβολία συμπεριφέρεται (τοπικά) ως επίπεδο κύμα $|\boldsymbol{E}| = \eta_0 |\boldsymbol{H}|$. Υπολογίζοντας το ολοκλήρωμα για $F = F_{\text{inc}}$ και $F = F_{\text{rad}}$ από τις σχέσεις (1.1) και (1.2), καταλήγουμε στην παρακάτω σχέση, που συνδέει την εκπεμπόμενη ισχύ παρουσία της διάταξης με την ισχύ που εκπέμπει η πηγή όταν βρίσκεται μόνη της:

$$\frac{P_{\text{rad}}}{P_{\text{inc}}} = \sum_{n=-\infty}^{+\infty} |C_n|^2. \tag{1.4}$$

Η σχέση αυτή αποτελεί την μετρική μας για την εργασία αυτή και επιθυμούμε να την μεγιστοποιήσουμε, ώστε να καταλήξουμε σε υπερακτινοβολούσες διατάξεις. Επομένως, ορίζουμε το μέγεθος:

$$\rho = \max_{L}\{P_{\mathrm{rad}}/P_{\mathrm{inc}}\} \tag{1.5}$$

για τις διατάξεις με ένα μόνο κυλινδρικό σύνορο ενώ για πιο πολύπλοκες διατάξεις με δύο σύνορα, όπως αυτές του Σχ. 1.1, γίνεται μία επιπλέον βελτιστοποίηση με βάση το εσωτερικό σύνορο, δηλαδή:

$$\rho_{\max} = \max_{g}\{\rho\}. \tag{1.6}$$

Τα δύο αυτά μεγέθη παρουσιάζονται στο υπόλοιπο της εργασίας ως συναρτήσεις της εξωτερικής ακτίνας a και του υλικού, ώστε να προκύψουν συμπεράσματα για τη συμπεριφορά της εκάστοτε διάταξης.

1.3 Τέλεια Αγώγιμοι Κύλινδροι

Η πρώτη προς μελέτη διάταξη αποτελείται από έναν τέλεια αγώγιμο (PEC) κύλινδρο ακτίνας a και την πηγή τοποθετημένη σε απόσταση $L > a$ από τον άξονα του κυλίνδρου. Η βελτίωση της εκπεμπόμενης ισχύος $P_{\mathrm{rad}}/P_{\mathrm{inc}}$ στο επίπεδο $(a/\lambda,\, L/a)$ φαίνεται στο Σχ. 1.2.

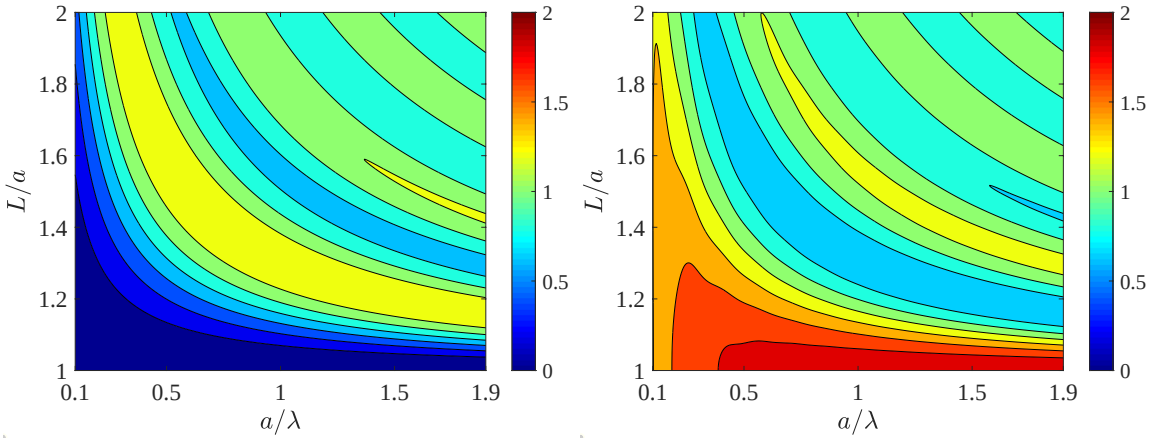

(α′) (β′)

Σχήμα 1.2: Η σχετική εκπεμπόμενη ισχύς $P_{\mathrm{rad}}/P_{\mathrm{inc}}$ στην περίπτωση τέλεια αγώγιμου κυλίνδρου ακτίνας a συναρτήσει της ηλεκτρικής ακτίνας a/λ και της κανονικοποιημένης θέσης της πηγής L/a. (α′) TM κύματα, (β′) TE κύματα.

Στο Σχ. 1.2(α′) φαίνονται τα αποτελέσματα για την TM διέγερση. Παρατηρούμε ότι η εκπεμπόμενη ισχύς μηδενίζεται όταν η πηγή πλησιάζει τον κύλινδρο ενώ η μέγιστη τιμή που μπορεί να φτάσει είναι περίπου $1.4P_{\mathrm{inc}}$. Αντίθετα, όπως φαίνεται από το Σχ. 1.2(β′), οι TE πηγές μεγιστοποιούν την ισχύ τους κοντά στον κύλινδρο, πετυχαίνοντας τιμή $2P_{\mathrm{inc}}$. Τα αποτελέσματα αυτά μπορούν να επαληθευθούν λύνοντας το απλούστερο πρόβλημα της σκέδασης από ένα άπειρο τέλεια αγώγιμο επίπεδο με χρήση θεωρίας ειδώλων, το οποίο αποτελεί καλή προσέγγιση καθώς $d = L - a \to 0$. Η βελτίωση της

εκπομπής σε αυτήν την περίπτωση ισούται με:

$$\frac{P_{\text{rad}}}{P_{\text{inc}}} \cong \begin{cases} 1 - J_0(2k_0 d), & \text{TM} \\ 1 + J_0(2k_0 d), & \text{TE} \end{cases}, \tag{1.7}$$

όπου $d = L - a$.Παρατηρούμε ότι όντως σε αυτήν την περίπτωση, η εκπεμπόμενη ισχύς μηδενίζεται όταν η TM πηγή πλησιάζει τον αγωγό ενώ το αντίθετο ισχύει για την TE πηγή, η οποία διπλασιάζει την ισχύ της. Με άλλα λόγια, το TM είδωλο εξουδετερώνει την πηγή ενώ το TE είδωλο την ενισχύει. Επιπλέον, μεγιστοποιώντας τον άνω κλάδο καταλήγουμε όντως σε τιμή περίπου ίση με 1.4.

1.4 Συμπαγείς Κύλινδροι

Καθώς η χρήση τέλεια αγώγιμα κυλίνδρου δεν οδηγεί σε αρκετά ισχυρή ακτινοβόληση, συνεχίζουμε την αναζήτηση βέλτιστων διατάξεων. Η επόμενη διάταξη είναι και πάλι σχετικά απλή και αποτελείται από έναν συμπαγές κύλινδρο ακτίνας a, από υλικό με μιγαδική σχετική διηλεκτρική σταθερά ε. Η πηγή και πάλι τοποθετείται σε απόσταση L από τον άξονα του κυλίνδρου. Όσον αφορά τη διηλεκτρική σταθερά, καθώς επιθυμούμε τη μεγιστοποίηση της ισχύος στα πλαίσια αυτής της Εργασίας, το σωστό θα ήταν οι διατάξεις μας ιδανικά να μην είχαν απώλειες ($\text{Im}[\varepsilon] = 0$). Παρ΄ όλα αυτά, ενδεχομένως η επιλογή αυτή να οδηγούσε σε αριθμητικά προβλήματα ως απόρροια μη ρεαλιστικών συντονισμών σε περιπτώσεις ENZ υλικών και υλικών με $\varepsilon = -1$. Επομένως, επιλέγουμε ένα μικρό φανταστικό μέρος ($\text{Im}[\varepsilon] = -0.03$) για όλες τις περιπτώσεις που ακολουθούν.

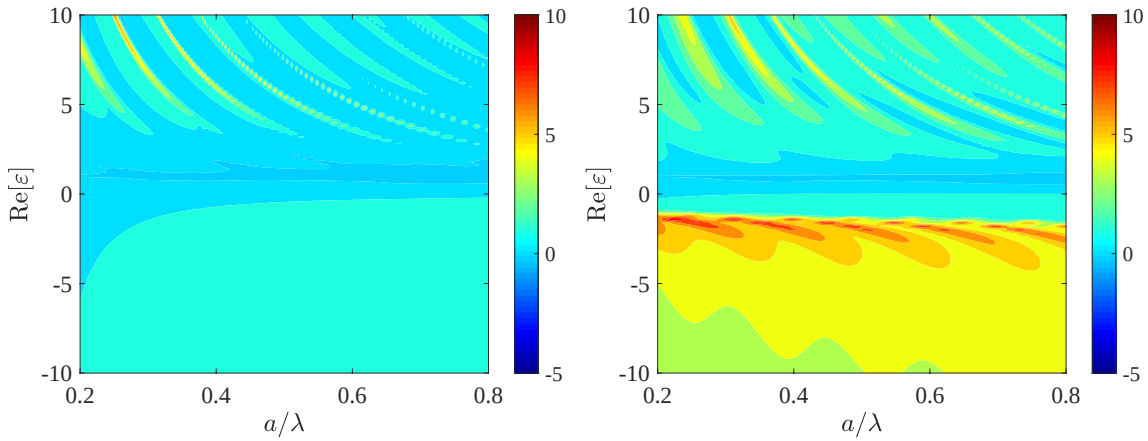

Σχήμα 1.3: Η μετρική ρ από την σχέση (1.5) (σε dB), για $L > a$, ως συνάρτηση της οπτικής ακτίνας a/λ ενός συμπαγούς κυλίνδρου και του πραγματικού μέρους της σχετικής διηλεκτρικής του σταθεράς $\text{Re}[\varepsilon]$, υπό διέγερση: (α′) TM πόλωσης, (β′) TE πόλωσης. Χρησιμοποιούνται μικρές απώλειες ίσες με $\text{Im}[\varepsilon] = -0.03$.

Παρατηρούμε ότι και στις δύο πολώσεις η ενίσχυση πλέον είναι έως και 10 dB, αρκετά μεγαλύτερη από την προηγούμενη περίπτωση. Ειδικότερα, όσον αφορά την TM πόλωση (Σχ. 1.3(α′)), οι μέγιστες τιμές επιτυγχάνονται σε διηλεκτρικές ($\text{Re}[\varepsilon] > 0$) παραμετρικές λωρίδες, για μικρά σχετικές ακτίνες a/λ. Από την άλλη, στην περίπτωση της TE πόλωσης (Σχ. 1.3(β′)) παρατηρούμε αυξημένη επίδοση στις πλασμονικές

($\mathrm{Re}[\varepsilon] < 0$) διατάξεις, ενώ συνεχίζουν να υπάρχουν παρόμοιες παραμετρικές λωρίδες σε περιπτώσεις διηλεκτρικών ($\mathrm{Re}[\varepsilon] > 0$) κυλίνδρων.

1.5 Μη Συμπαγείς Κύλινδροι

Με σκοπό την επίτευξη ακόμα υψηλότερων επιδόσεων, επιστρατεύουμε τη γεωμετρία του Σχ. 1.1(α′), τοποθετώντας την πηγή στο εσωτερικό ($0 \leq L \leq g$). Με τον τρόπο αυτό, η διάταξη "αγκαλιάζει" την πηγή, δημιουργώντας μία συντονισμένη κοιλότητα. Η θέση της πηγής είναι τέτοια ώστε το είδωλο που προκύπτει μέσα στο κέλυφος να μεγιστοποιεί την εκπεμπόμενη ακτινοβολία. Στο Σχ. 1.4 απεικονίζεται σε dB η μετρική $\rho_{\max}$ στο επίπεδο (a/λ, $\mathrm{Re}[\varepsilon]$), υποθέτοντας τις ίδιες μικρές απώλειες όπως προηγουμένως. Παρατηρούμε ενίσχυση έως και 25 dB και για τις δύο πολώσεις στις πλασμονικές σχεδιάσεις. Στις περιπτώσεις αυτές, παρατηρείται η ανάπτυξη ενός ζεύγους evanescent ρυθμών στο κέλυφος, οι οποίοι το ενεργοποιούν αποδοτικότερα από τους ταλαντωτικούς ρυθμούς στις διηλεκτρικές περιπτώσεις [3]. Όσον αφορά την TM πόλωση (Σχ. 1.4(α′)), παρατηρούμε δύο παραμετρικές περιοχές υψηλών επιδόσεων στο ημιεπίπεδο των πλασμονικών σχεδιάσεων. Από την άλλη, στην TE πόλωση (Σχ. 1.4(β′)), παρατηρούνται 3 τέτοιες περιοχές, οι οποίες είναι πιο εκτεταμένες και αντιστοιχούν σε υψηλότερες εκπεμπόμενες ακτινοβολίες. Τέλος, οι παραμετρικές λωρίδες που είχαν βρεθεί για διηλεκτρικά στο Σχ. 1.3 συνεχίζουν να υπάρχουν και εδώ.

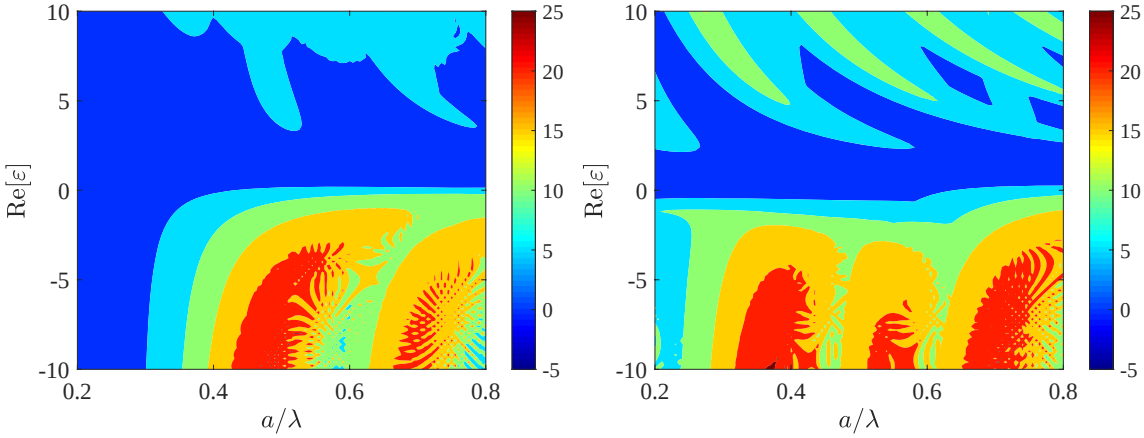

Σχήμα 1.4: Αποτελέσματα για συμπαγή κύλινδρο εσωτερικής ακτίνας g και εξωτερικής a. Η μετρική $\rho_{\max}$ από την σχέση (1.6) σε dB, συναρτήσει της οπτικής ακτίνας a/λ και του πραγματικού μέρους της σχετικής διηλεκτρικής σταθεράς $\mathrm{Re}[\varepsilon]$ υπό: (α′) TM διέγερση, (β′) TE διέγερση. Η πηγή τοποθετείται στο εσωτερικό ($0 \leq L < g$).

Στο Σχ. 1.5 απεικονίζουμε τη συχνότητα εμφάνισης των πιο πετυχημένων σχεδιάσεων ($\rho_{\max} > 24$ dB) συναρτήσει του πηλίκου g/a. Κατά την αναζήτηση των διατάξεων αυτών, παρατηρούμε ότι αρκετές από αυτές επιλέγουν κεντρική τροφοδοσία ($L = 0$) για τη βέλτιστη λειτουργία τους. Για το λόγο αυτό, στο Σχ. 1.5(α′) απεικονίζουμε την κατανομή αυτών των σχεδιάσεων. Είναι σημαντικό να σημειώσουμε ότι τα σημεία που αντιστοιχούν στα TM κύματα προκύπτουν από την αριστερότερη πλασμονική νησίδα του Σχ. 1.5(α′) ($0.45 < a/\lambda < 0.55$), ενώ τα αντίστοιχα TE για

$0.65 < a/\lambda < 0.75$. Παρατηρούμε ότι οι TM κεντρικά τροφοδοτούμενες διατάξεις απαιτούν παχύτερα κελύφη για βέλτιστη λειτουργία από τις αντίστοιχες TE. Εκτός από τις κεντρικά διεγερμένες σχεδιάσεις, προκύπτουν υψηλές επιδόσεις όταν $L \cong g/2$ για TM κύματα και $L \cong g$ για TE. Οι περιπτώσεις αυτές παρουσιάζονται στο Σχ. 1.5(β′). Εδώ πλέον οι TE πηγές χρειάζονται παχύτερα κελύφη και $0.3 < a/\lambda < 0.45$, ενώ οι TM πηγές μικρότερα κελύφη και $0.65 < a/\lambda < 0.75$.

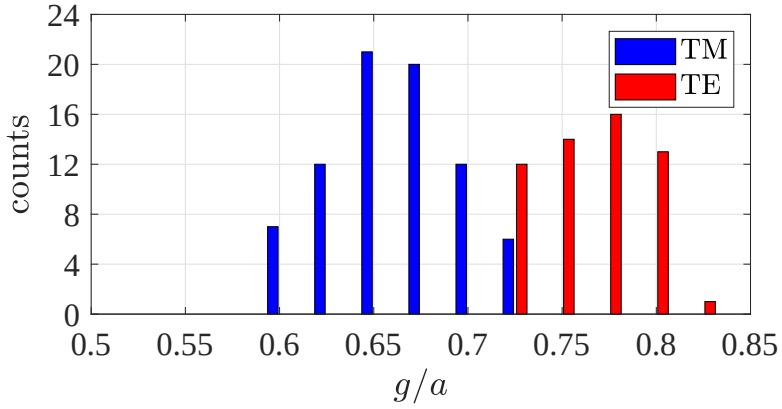

(α′)

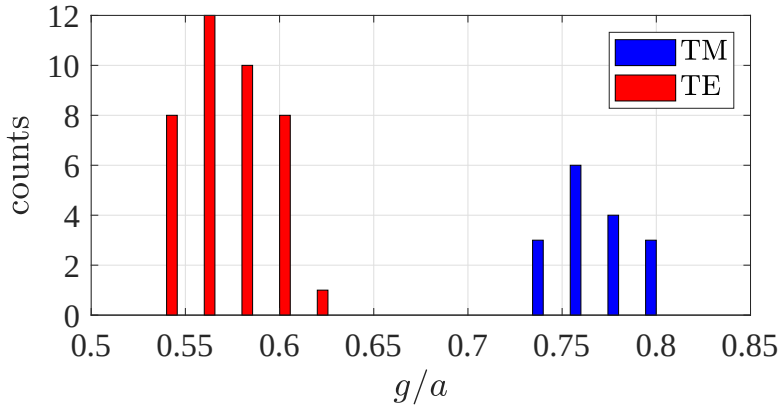

(β′)

Σχήμα 1.5: Ο αριθμός των επιτυχημένων ($\rho_{\max} > 24$ dB) υπεραχτινοβολούντων διατάξεων, από το Σχ.1.4, συναρτήσει του πηλίκου g/a και για τις δύο πολώσεις. (α′) Κεντρική διέγερση ($L = 0$), (β′) Μη κεντρική διέγερση ($L \cong g/2$ για TM κύματα, $L \cong g$ για TE κύματα).

Στο σημείο αυτό, είναι σημαντικό να μελετήσουμε τη συμπεριφορά μη συμπαγών κυλίνδρων με υψηλότερες απώλειες ($\mathrm{Im}[\varepsilon] = -0.3$) καθώς και με εξωτερική τροφοδοσία ($L > a$). Στα Σχήματα 1.6(α′) και 1.6(β′) φαίνονται τα αποτελέσματα για τις διατάξεις με υψηλές απώλειες, για TM και TE κύματα αντίστοιχα. Παρατηρούμε ότι ενώ υπάρχει μείωση των επιδόσεων σε σχέση με το Σχ. 1.5, όπως αναμενόταν, οι παραμετρικές περιοχές διατηρούν τη μορφή τους. Επομένως, οι διατάξεις είναι αρκετά εύρωστες σε Ωμικά φαινόμενα. Επιπλέον, από τα Σχήματα 1.6(γ′) και 1.6(δ′), όπου παρουσιάζονται τα αποτελέσματα για την εξωτερική διέγερση, καθίσταται προφανές ότι οι επιδόσεις είναι χαμηλότερες ενώ τα διαγράμματα είναι παρόμοια με αυτά του Σχ. 1.3.

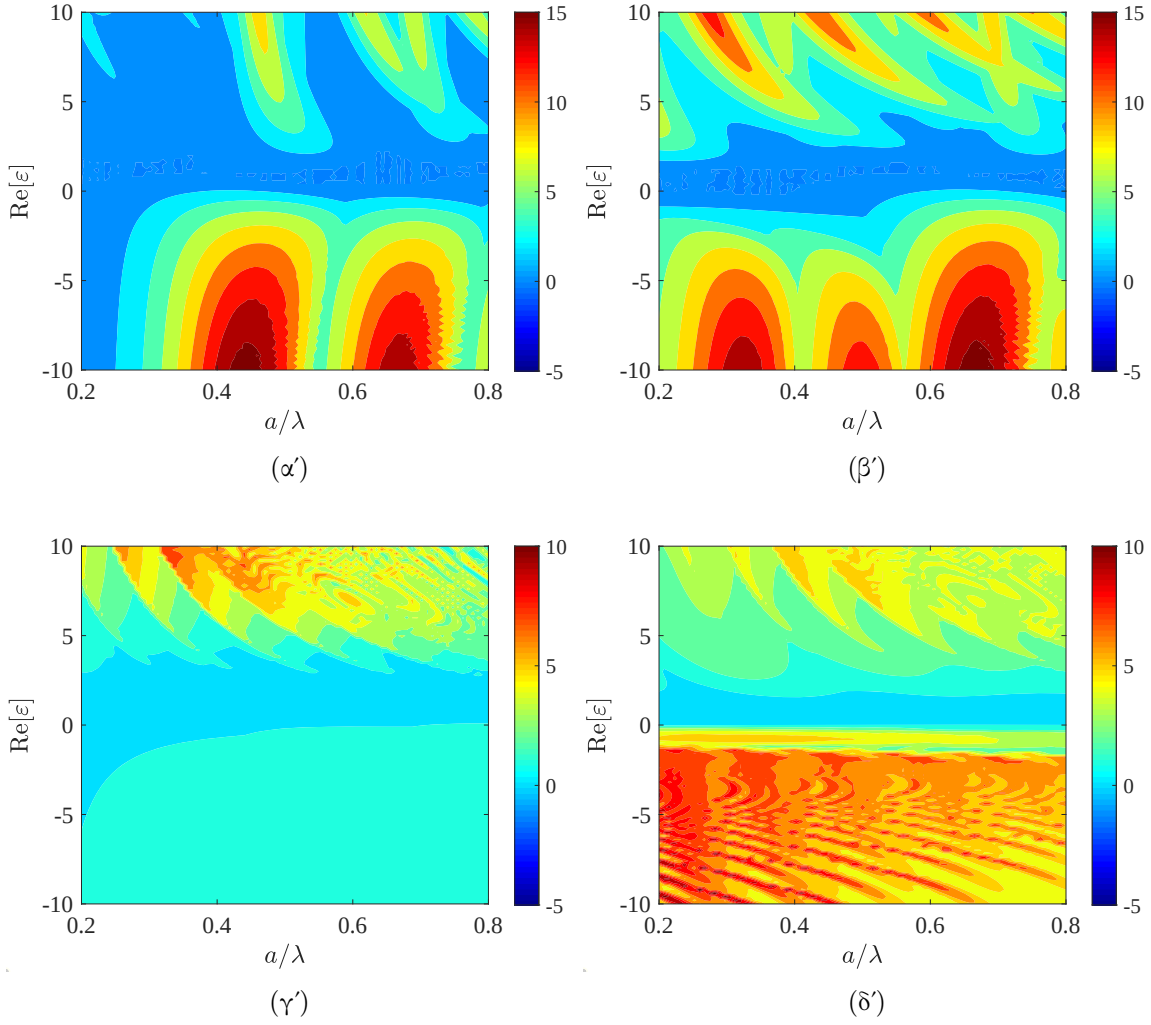

Σχήμα 1.6: Η μετρική $\rho_{\max}$, σε dB, στο επίπεδο $(a/\lambda,\ \mathrm{Re}[\varepsilon])$ για: (α′) υψηλότερες απώλειες ($\mathrm{Im}[\varepsilon] = -0.3$) για TM κύματα, (β′) υψηλότερες απώλειες ($\mathrm{Im}[\varepsilon] = -0.3$) για TE κύματα, (γ′) εξωτερική TM διέγερση ($L > a$), (δ′) εξωτερική TE διέγερση ($L > a$).

1.6 Συζευγμένοι Νανοσωλήνες

Η επόμενη προς μελέτη διάταξη είναι η πιο αποτελεσματική ανάμεσα σε όλες τις οποίες μελετάμε στην Εργασία αυτή και αποτελείται από δύο ομόκεντρους νανοσωλήνες, ακτίνας g και a και μιγαδικής επιφανειακής αγωγιμότητας σ, όπως φαίνεται στο Σχ. 1.1(β′). Για να είναι βέβαια η σύγκριση με τις προηγούμενες διατάξεις δίκαιη, θα πρέπει και πάλι να συμπεριλάβουμε μικρές σταθερές απώλειες. Χρησιμοποιώντας τον τύπο [4]: $\sigma\eta_0 = \mathrm{i}k_0 d\,(\varepsilon - 1)$, όπου η_0 η κυματική αντίσταση του κενού και d το πάχος της μεταεπιφάνειας, μπορούμε να συνδέσουμε την αγωγιμότητα ενός νανοσωλήνα με μία αντίστοιχη διηλεκτρική σταθερά ε. Επιλέγοντας $d/\lambda = 0.1$, για $\mathrm{Im}[\varepsilon] = -0.03$, προκύπτει $\mathrm{Re}[\sigma\eta_0] \cong 0.019$.

Πριν μελετήσουμε όμως το ζεύγος μεταεπιφανειών, θα είχε ενδιαφέρον να δούμε τη συμπεριφορά ενός μόνου νανοσωλήνα ακτίνας a, ο οποίος διεγείρεται από πηγή στο εσωτερικό ($L < a$). Στο Σχ. 1.7(α′), όπου παρουσιάζονται τα αποτελέσματα για την TM πόλωση, παρατηρούμε την επίτευξη υψηλών μεγίστων πάνω σε παραμετρικές λω-

ρίδες ενώ εξωτερικά αυτών, η πηγή πρακτικά μπλοκάρεται. Παρόμοια συμπεράσματα προκύπτουν και από το Σχ. 1.7(β′) που αντιστοιχεί στην TE πόλωση. Όμως, στην περίπτωση αυτή επιτυγχάνονται υψηλές επιδόσεις σε μεγαλύτερο μέρος των παραμετρικών λωρίδων. Είναι προφανές ότι χρήση ενός μόνου νανοσωλήνα μπορεί να οδηγήσει σε σχεδιάσεις οι οποίες δίνουν επιδόσεις αντίστοιχες με αυτές της περιπλοκότερης διάταξης του Σχ. 1.1(α′).

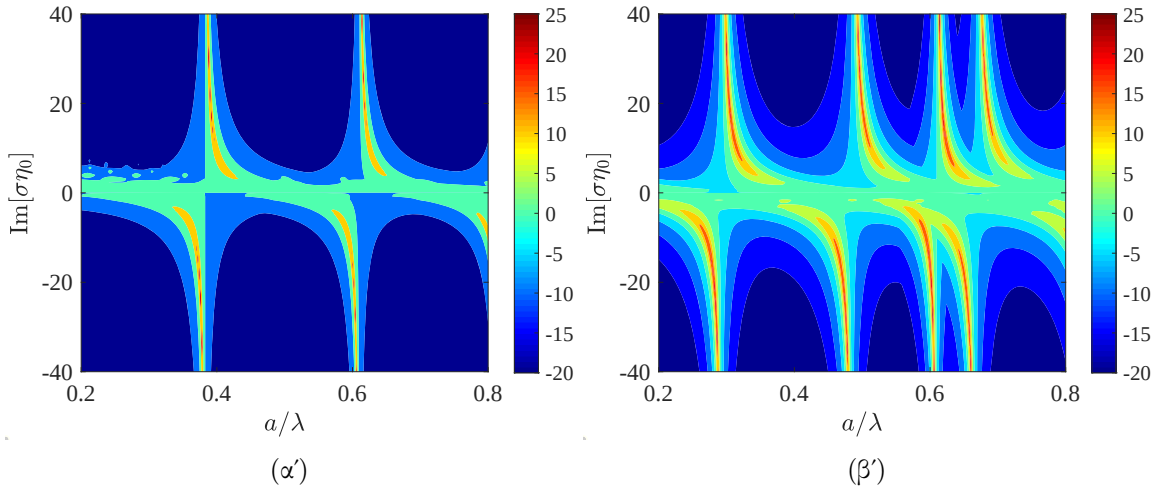

Σχήμα 1.7: Αποτελέσματα για έναν νανοσωλήνα ακτίνας a και μιγαδικής επιφανειακής αγωγιμότητας σ. Η μετρική ρ (σε dB) απεικονίζεται στο επίπεδο $(a/\lambda,\ \mathrm{Im}[\sigma\eta_0])$, στην περίπτωση: (α′) TM πόλωσης, (β′) TE πόλωσης. Υποθέτουμε σταθερές χαμηλές απώλειες: $\mathrm{Re}[\sigma\eta_0] \cong 0.019$.

Προχωράμε τώρα στην πιο αποδοτική από τις διατάξεις, αυτή των ομόκεντρων μεταπιφανειών, στις οποίες η πηγή τοποθετείται μεταξύ των δύο συνόρων $g < L < a$. Με τον τρόπο αυτό, δημιουργείται μία κοιλότητα συντονισμού, μέσα στην οποία η πηγή τοποθετείται με τρόπο τέτοιο ώστε οι πολλαπλοί ρυθμοί που αναπτύσσονται να συμβάλλουν θετικά. Τα αποτελέσματα του Σχήματος 1.8 ότι πράγματι, μιλάμε για τις μεγαλύτερες επιδόσεις, με βελτίωση της ισχύος μέχρι και 3 τάξεις μεγέθους. Παρατηρούμε και στις δύο πολώσεις (Σχ. 1.8(α′) για TM, Σχ. 1.8(β′) για TE) την ύπαρξη εκτενών παραμετρικών περιοχών στις οποίες επιτυγχάνονται πολύ υψηλές επιδόσεις, τόσο για διηλεκτρικές όσο και για πλασμονικές διατάξεις. Στην TM περίπτωση παρ′ όλα αυτά, οι μέγιστες τιμές είναι λίγο μικρότερες από τις αντίστοιχες στην TE πόλωση, ενώ διατηρείται μια περιοχής μπλοκαρίσματος της πηγής για πλασμονικές σχεδιάσεις μικρής εξωτερικής ηλεκτρικής ακτίνας a/λ.

1.7 Επιλεγμένες Διατάξεις

Καθώς οι καλύτερες επιδόσεις επιτυγχάνονται στις διατάξεις με ζεύγος νανοσωλήνα, θα ήταν ενδιαφέρον να επιλέξουμε τις καλύτερες σχεδιάσεις και για τις δύο πολώσεις (TM και TE) και για διηλεκτρικά ($\mathrm{Im}[\sigma\eta_0] > 0$) και πλασμονικά ($\mathrm{Im}[\sigma\eta_0] < 0$) υλικά. Παρατηρώντας το Σχ. 1.8, βλέπουμε ότι για $a/\lambda = 0.62$ είναι δυνατόν να πετύχουμε εξαιρετικά μεγάλη εκπεμπόμενη ισχύ και για τις δύο πολώσεις αλλά και για τους δύο τύπους υλικών. Όσον αφορά την τιμή του φανταστικού μέρους της αγωγιμότητας, αποφεύγουμε να χρησιμοποιήσουμε τιμές που βρίσκονται στα άκρα του διαστήματος

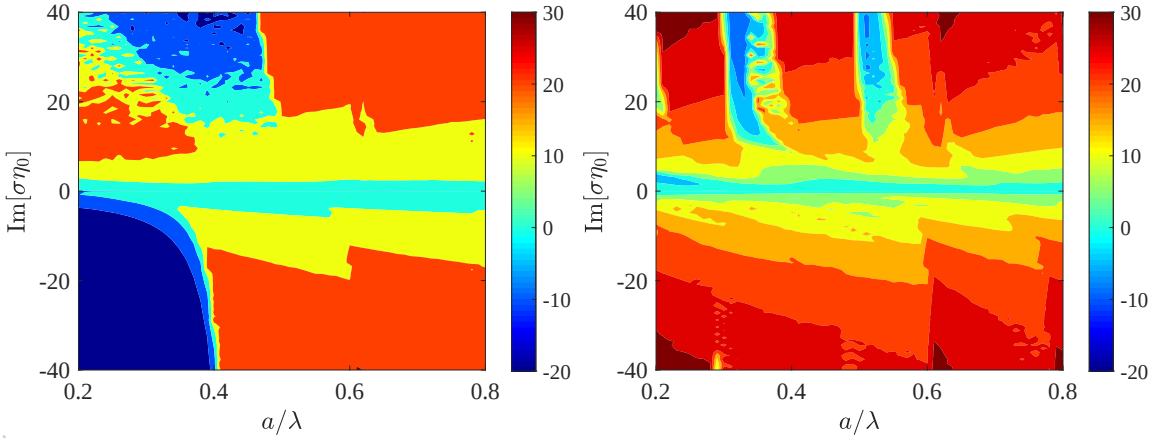

Σχήμα 1.8: Αποτελέσματα για ένα ζεύγος ομόκεντρων, συζευγμένων νανοσωλήνων, ακτινών g και a και μιγαδικής επιφανειακής αγωγιμότητας σ, με την πηγή ανάμεσα τους ($g < L < a$). Η μετρική $\rho_{\max}$ (σε dB), παρουσιάζεται στο επίπεδο (a/λ, Im$[\sigma\eta_0]$), στην περίπτωση: (α′) TM πόλωσης, (β′) TE πόλωσης. Υποθέτουμε σταθερές χαμηλές απώλειες: Re$[\sigma\eta_0] \cong 0.019$.

$[-40, 40]$, οπότε επιλέγουμε Im$[\sigma\eta_0] = \pm 20$. Στο Σχ. 1.9 απεικονίζεται η αύξηση της εκπεμπόμενης ισχύος στις περιπτώσεις αυτές στο επίπεδο $(g/L, L/a)$. Παρατηρώντας τα διαγράμματα αυτά, βλέπουμε ότι οι TE πηγές προτιμούν να βρίσκονται κοντά στα σύνορα $r = g$ ή $r = a$. Από την άλλη, οι TM πηγές προτιμούν να απέχουν το ίδιο από αυτά. Το αποτέλεσμα αυτό μπορεί να εξηγηθεί με χρήση της θεωρίας ειδώλων, όπως αναφέραμε και στην περίπτωση του τέλεια αγώγιμου κυλίνδρου. Ειδικότερα, σε περιπτώσεις υψηλής αγωγιμότητας όπου προσομοιάζεται η PEC περίπτωση, τα TM είδωλα εξουδετερώνουν την πηγή καθώς αυτή πλησιάζει το σύνορο, ενώ τα TE την ενισχύουν.

Στο σημείο αυτό, έχει σημασία να μελετήσουμε ορισμένα τεχνικά χαρακτηριστικά των επιλεγμένων διατάξεων, συγκεκριμένα τη συμπεριφορά τους σε διεγέρσεις μεταβαλλόμενου μήκους κύματος καθώς και τα παραγόμενα διαγράμματα ακτινοβολίας στο επίπεδο xy.

Για τον σκοπό αυτό, στο Σχ. 1.10 παρουσιάζουμε την εκπεμπόμενη ισχύ στις περιπτώσεις του Σχ. 1.9. Επιπλέον, έχουμε μελετήσει και τη συμπεριφορά των αντίστοιχων διατάξεων με αυξημένες απώλειες (Re$[\sigma\eta_0] \cong 2.8$) καθώς και τις περιπτώσεις της μη βέλτιστης πόλωσης. Από την παρατήρηση του Σχ. 1.10 καθίσταται προφανές ότι σε όλες τις περιπτώσεις υπάρχει ένα συντονισμός στο βέλτιστο σημείο λειτουργίας λ_0, όσον αφορά τις βέλτιστες σχεδιάσεις (με μικρές απώλειες και διεγερμένες από την προτιμούμενη πόλωση). Όπως αναμενόταν, οι απώλειες μειώνουν την οξύτητα του συντονισμού και τη μέγιστη τιμή. Επιπλέον, παρατηρούμε ότι οι πλασμονικές διατάξεις έχουν την ιδιότητα να ενισχύουν και την πόλωση για την οποία δεν είναι βελτιστοποιημένες. Το αντίθετο ισχύει για τις διηλεκτρικές διατάξεις. Το γεγονός αυτό θα φανεί και από τα παραγόμενα διαγράμματα ακτινοβολίας που προκύπτουν από την αναλυτική λύση αλλά και από προσομοιώσεις.

Προκειμένου να μελετήσουμε την αζιμουθιακή κατανομή της ισχύος στο μακρινό πεδίο για τις 4 επιλεγμένες υπερακτινοβολούσες διατάξεις, ορίζουμε ένα αζιμουθιακά

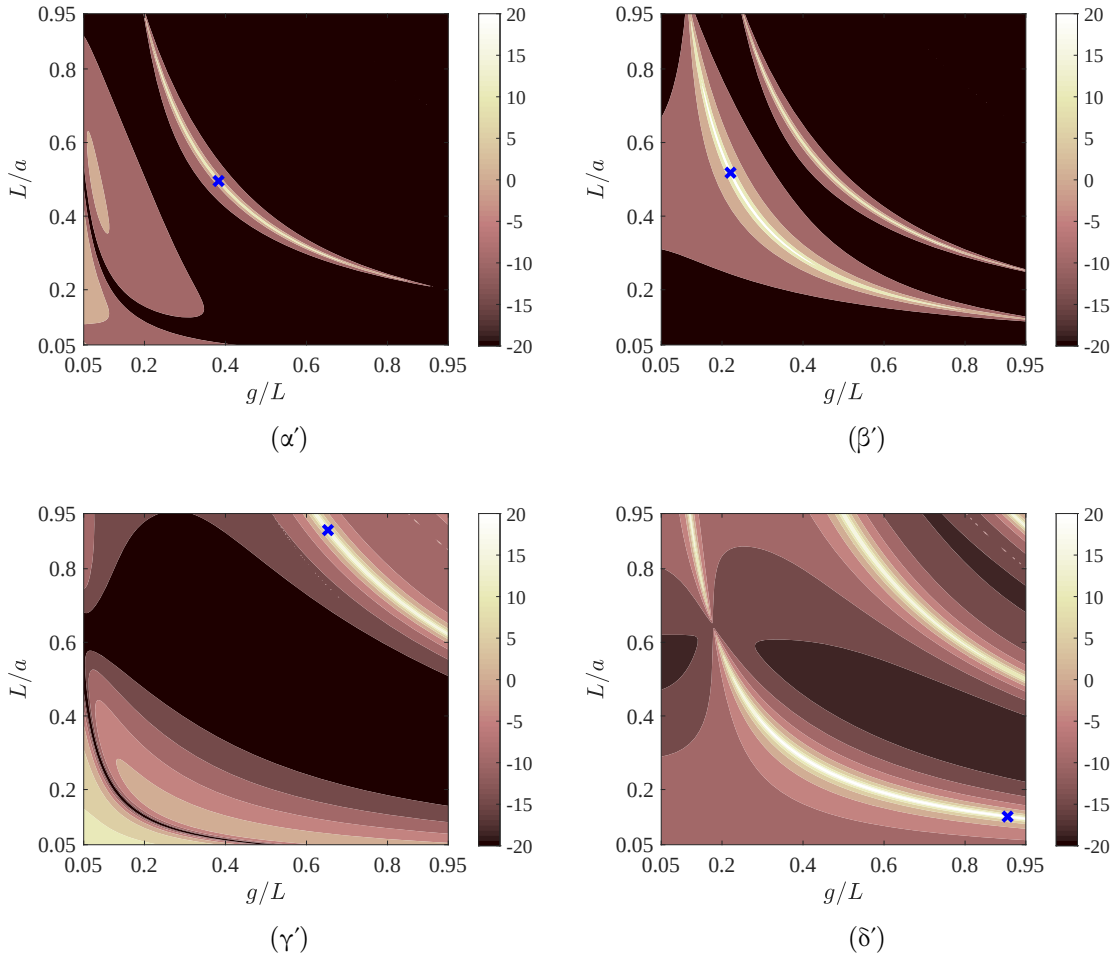

Σχήμα 1.9: Η σχετική εκπεμπόμενη ισχύς $P_{\rm rad}/P_{\rm inc}$ (σε dB), στο επίπεδο των παραμέτρων $(g/L, L/a)$ για $a/\lambda = 0.62$. (α′) $\mathrm{Im}[\sigma\eta_0] = 20$, TM πόλωση, (β′) $\mathrm{Im}[\sigma\eta_0] = -20$, TM πόλωση, (γ′) $\mathrm{Im}[\sigma\eta_0] = 20$, TE πόλωση, (δ′) $\mathrm{Im}[\sigma\eta_0] = -20$, TE πόλωση. Οι μπλε σταυροί δείχνουν τα σημεία των βέλτιστων σχεδιάσεων.

εξαρτώμενο προφίλ ισχύος $p(\varphi)$ του οποίου η μέση τιμή στο διάστημα $[0, 2\pi]$ ισούται με την σχετική ισχύς $P_{\rm rad}/P_{\rm inc}$, δηλαδή:

$$\frac{P_{\rm rad}}{P_{\rm inc}} = \frac{1}{2\pi}\int_0^{2\pi} p(\varphi)\mathrm{d}\varphi. \tag{1.8}$$

Με εφαρμογή του θεωρήματος Poynting, με τον ίδιο τρόπο που περιγράφτηκε στην αρχή αυτής της εκτεταμένης περίληψης, προκύπτει ότι:

$$p\left(\varphi\right) = \left|\sum_{n=-\infty}^{+\infty} \mathrm{i}^n C_n e^{\mathrm{i}n\varphi}\right|^2. \tag{1.9}$$

Στο Σχ. 1.11 έχουμε απεικονίσει το μέγεθος αυτό σε πολικό διάγραμμα, για τις ίδιες ακριβώς διατάξεις με το Σχ. 1.10. Παρατηρώντας τα διαγράμματα αυτά, είναι σαφές ότι τα διαγράμματα ακτινοβολίας σε 3 από τις 4 βέλτιστες διατάξεις είναι είτε ομοιοκατευθυντικά είτε διπολικά. Αυτό δεν είναι απόρροια μιας κεντρικής τροφοδοσίας, καθώς $L \neq 0$. Αντιθέτως, στις διατάξεις αυτές οι αζιμουθιακές αρμονικές ανώτερης τάξης

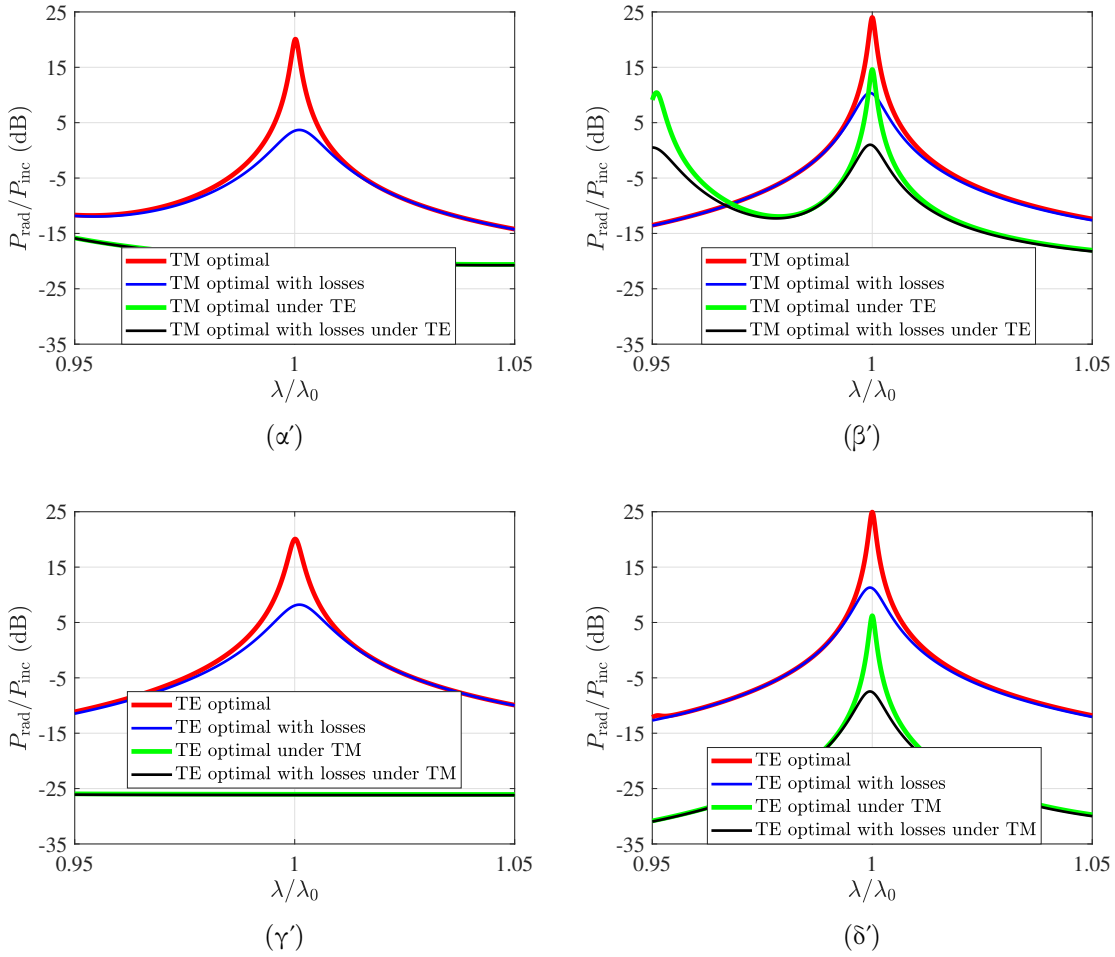

Σχήμα 1.10: Η σχετική εκπεμπόμενη ισχύς των επιλεγμένων σχεδιάσεων $P_{\rm rad}/P_{\rm inc}$ (σε dB) συναρτήσει του κανονικοποιημένου μήκους κύματος λ/λ_0, γύρω από το βέλτιστο σημείο λειτουργία $\lambda = \lambda_0$, στις περιπτώσεις του: (α′) Σχ. 1.9(α′), (β′) Σχ. 1.9(β′), (γ′) Σχ. 1.9(γ′), (δ′) Σχ. 1.9(δ′).

$|n| \geq 2$ καταπιέζονται μέσα στην κοιλότητα στην οποία βρίσκεται η πηγή, ενώ ταυτόχρονα οι ρυθμοί $n \leq |1|$ αλληλεπιδρούν βέλτιστα με τα τοιχώματα, οδηγώντας σε εξαιρετικά ισχυρά ομοιοκατευθυντική ή διπολική ακτινοβολίας προς το μακρινό πεδίο. Βλέπουμε επίσης ότι οι πλασμονικές διατάξεις ενισχύουν και τη μη βέλτιστη πόλωση με απλά διαγράμματα ακτινοβολίας, αντίθετα από αυτά των βέλτιστων σχεδιάσεων. Παρ΄ όλα αυτά, η γεωμετρία του Σχ. 1.11(γ′) είναι η μοναδική που περιέχει και μεγαλύτερης τάξης αρμονικές στο εξωτερικό πεδίο.

Τα αποτελέσματα αυτά είναι σημαντικό να επαληθευτούν μέσω προσομοιώσεων, ώστε να επιβεβαιώσουμε την ορθότητα αυτών των πολύ απλών διαγραμμάτων ακτινοβολίας που τελικά προκύπτουν. Για τον σκοπό αυτό, προσομοιώνουμε τις διατάξεις με χρήση του COMSOL Multiphysics [5], και παράγουμε την κατανομή των πεδίων κάθε πόλωσης.

Στο Σχ. 1.12 παρουσιάζονται τα αποτελέσματα των προσομοιώσεων για τη διάταξη του Σχ. 1.9(γ′). Συγκεκριμένα, στο Σχ. 1.12(α′) παρουσιάζεται η κατανομή του πεδίου όταν η πηγή είναι ελεύθερη, στο 1.12(β′) όταν υπάρχει μόνο το εσωτερικό σύνορο, στο 1.12(γ′) όταν υπάρχει μόνο το εξωτερικό, ενώ τέλος η πλήρης διάταξη προσομοιώνεται

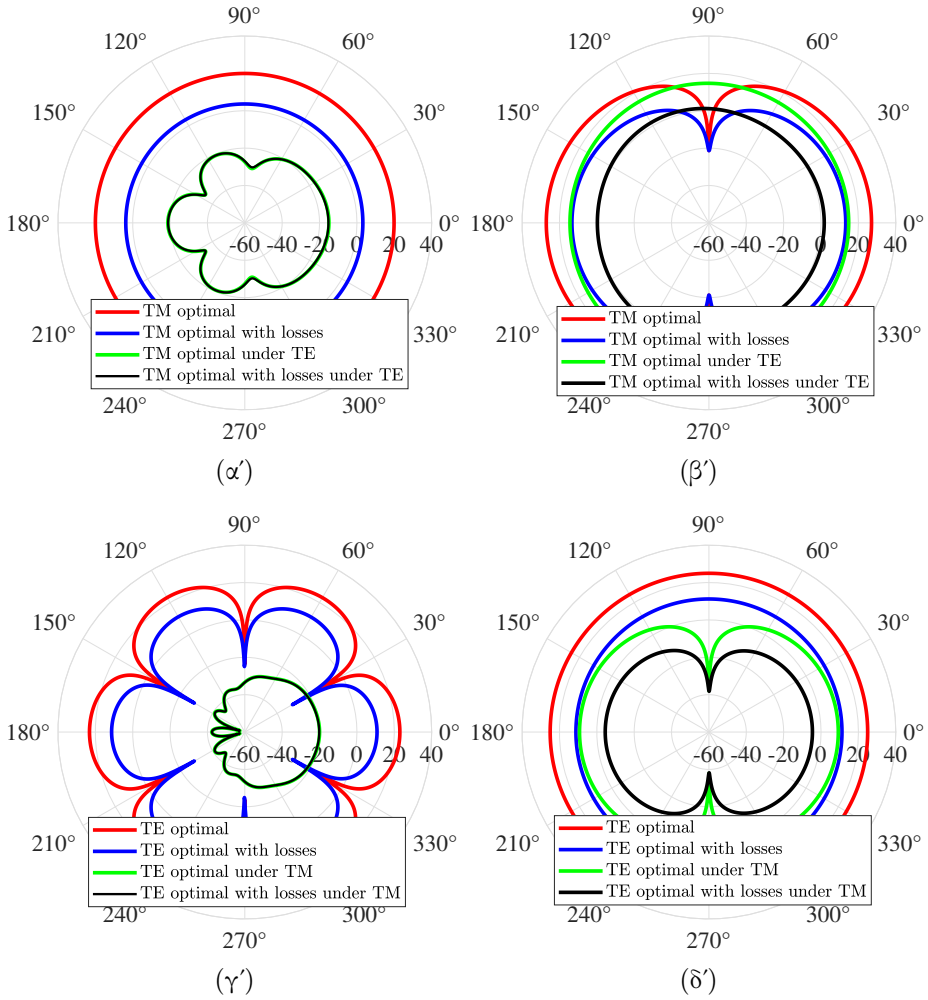

Σχήμα 1.11: Το αζιμουθιακό προφίλ ισχύος $p(\varphi)$ από τη Σχέση (1.9) (σε dB), σε πολικό διάγραμμα συναρτήσει της αζιμουθιακής γωνίας φ, για τις σχεδιάσεις από τα: (α′) Σχ. 1.9(α′), (β′) Σχ. 1.9(β′), (γ′) Σχ. 1.9(γ′), (δ′) Σχ. 1.9(δ′) και τις αντίστοιχες διατάξεις με μεγαλύτερες απώλειες, κάτω και από τις δύο πολώσεις.

στο Σχ. 1.12(δ′). Είναι προφανές ότι η πλήρης, βελτιστοποιημένη διάταξη οδηγεί σε ραγδαία αύξηση της εκπεμπόμενης ακτινοβολίας, τάξης μεγέθους μεγαλύτερης από τις περιπτώσεις χρήσης ενός μόνο συνόρου και της ελεύθερης πηγής. Επιπλέον, το διάγραμμα ακτινοβολίας του Σχ. 1.12(δ′) επιβεβαιώνει το αντίστοιχο θεωρητικό του Σχ. 1.11(δ′).

Στο Σχ. 1.13, έχουμε προσομοιώσει την κατανομή του πεδίου για την περίπτωση του Σχ. 1.9(β′), τόσο υπό την βέλτιστη TM πόλωση (ηλεκτρικό πεδίο E_z), τόσο και υπό TE πόλωση (μαγνητικό πεδίο H_z). Παρατηρώντας τα Σχ. 1.13(α′) και 1.13(β′), συμπεραίνουμε ότι η βέλτιστη πόλωση οδηγεί σε διπολικό διάγραμμα, ενώ η TE σε ομοιοκατευθυντικό, όπως ακριβώς προβλεπόταν από το Σχ. 1.11(β′). Επιπλέον, βλέπουμε ότι η βέλτιστη πόλωση οδηγεί σε πολύ μεγαλύτερες τιμές ακτινοβολίας στο μακρινό πεδίο, από τη μη βέλτιστη.

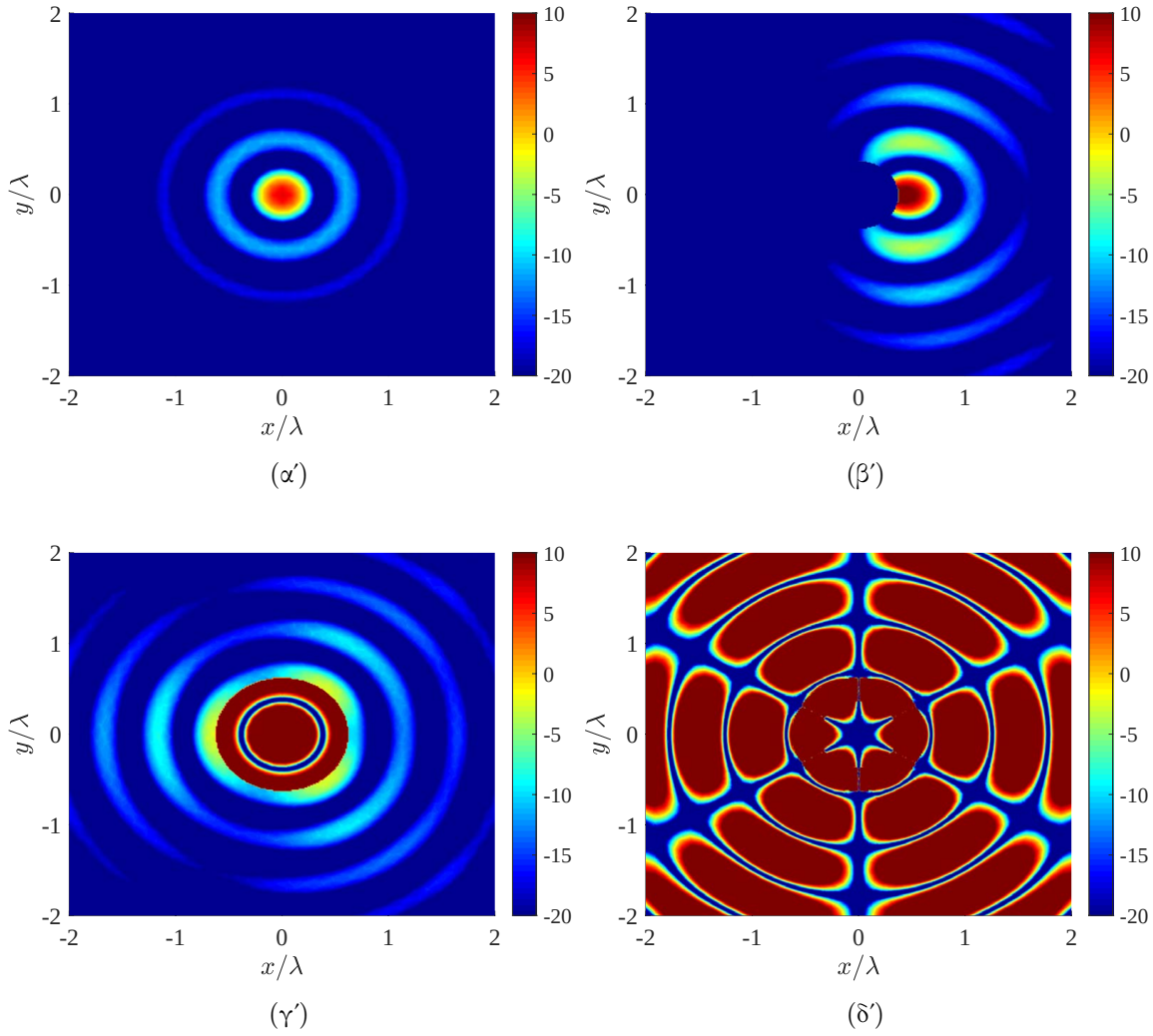

Σχήμα 1.12: Αποτελέσματα προσομοιώσεων για μία απο τις επιλεγμένες, TE-διεγερμένες, διηλεκτρικές γεωμετρίες. Η απόλυτη τιμή του πραγματικού μέρους της μοναδικής συνιστώσας του μαγνητικού πεδίου $|\mathrm{Re}[H_z(x,y)]|$, σε dB, στο επίπεδο xy, στην περίπτωση του Σχ. 1.9(γ′), όταν: (α′) η πηγή είναι ελεύθερη στο κενό, (β′) υπάρχει μόνο το εσωτερικό σύνορο, (γ′) υπάρχει μόνο το εξωτερικό σύνορο, (δ′) υπάρχει η πλήρης, βελτιστοποιημένη διάταξη.

1.8 Συμπεράσματα

Εν κατακλείδι, στην Εργασία αυτή έχει πραγματοποιηθεί μια εκτεταμένη αναζήτηση συνδυασμών δομικών και υλικών χαρακτηριστικών απλών κυλινδρικών γεωμετριών που οδηγούν σε σημαντική αύξηση της εκπεμπόμενης ισχύς μίας TM ή TE γραμμικής πηγής, σε σχέση με την ισχύ που αυτή εκπέμπει όταν βρίσκεται μόνη της στον ελεύθερο χώρο. Παρατηρούμε ότι υπερακτινοβολούσες διατάξεις μπορούν να βρεθούν όταν η πηγή τοποθετείται εσωτερικά ενός μη συμπαγούς κυλίνδρου και μεταξύ δυο συζευγμένων μεταεπιφανειών. Στις περιπτώσεις αυτές, η αλληλεπίδραση του πομπού με τα περιβάλλοντα σύνορα οδηγεί σε έως και 3 τάξεις μεγέθους ενίσχυση της ακτινοβολούμενης ισχύος στο μακρινό πεδίο. Τα διαγράμματα ακτινοβολίας των βέλτιστων διατάξεων που προκύπτουν μπορούν να είναι ομοιοκατευθυντικά ή διπολικά, διαφορε-

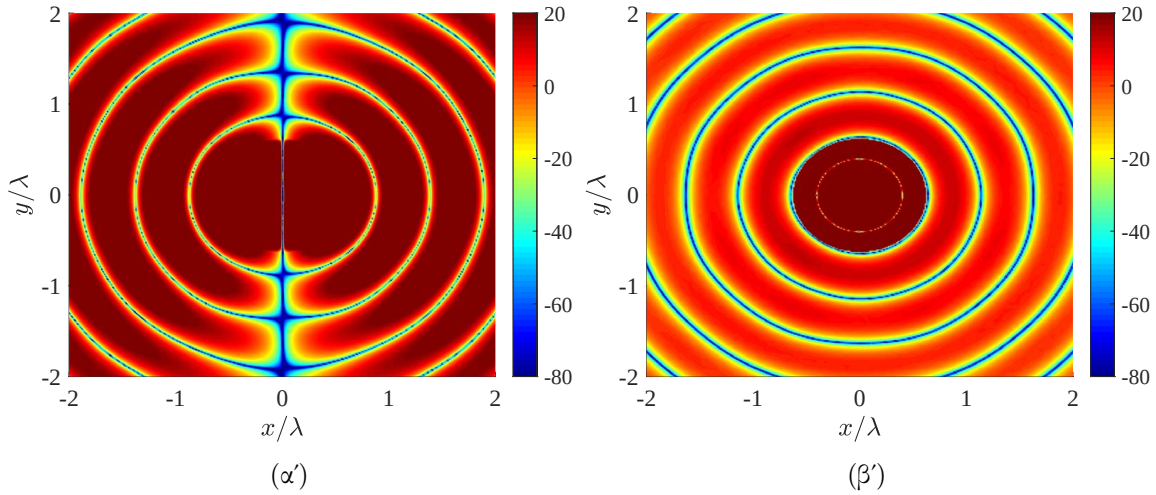

Σχήμα 1.13: Αποτελέσματα προσομοιώσεων για την πλασμονική διάταξη, βελτιστοποιημένη για TM διέγερση του Σχ. 1.9(β′), όταν χρησιμοποιείται: (α′) TM πηγή, αναπαριστώμενο μέγεθος $|\mathrm{Re}[E_z(x,y)]|$ σε dB, (β′) TE πηγή, αναπαριστώμενο μέγεθος $|\mathrm{Re}[H_z(x,y)]|$ σε dB.

τικά για κάθε πόλωση. Το χαρακτηριστικό αυτό καθιστά τις διατάξεις αυτές ιδανικές για κωδικοποίηση βάση της πόλωσης σε ένα αναλογικό σχήμα επεξεργασίας σήματος. Οι επιλεγμένες πλασμονικές μας σχεδιάσεις έχουν διάφορα πλεονεκτήματα απέναντι σε παραδοσιακές πλασμονικές κεραίες (διατάξεις dimer και bowtie). Πιο συγκεκριμένα, έχουν τη δυνατότητα να ενισχύουν ταυτόχρονα και τις δύο πολώσεις, επιτρέπουν ευκολότερη κατασκευή και επιδεικνύουν μειωμένη ευαισθησία σε μη τοπικά φαινόμενα.

Επιπλέον, η παρούσα Εργασία μπορεί να επεκταθεί για την κατασκευή διατάξεων με χαρακτηριστικά που απαιτούνται σε διάφορες εφαρμογές. Συγκεκριμένα, η προσθήκη μη γραμμικοτήτων στις μεταεπιφάνειες θα βοηθούσε στη μοντελοποίηση στοιχείων μνήμης με αυξημένη ευρωστία εναντίον του θορύβου [6]. Επιπλέον, μια πεπερασμένη ή άπειρη στοιχειοκεραία [7], αποτελούμενη από τις βέλτιστες διατάξεις αυτής της Εργασίας, θα μπορούσε να χρησιμοποιηθεί σε εφαρμογές που απαιτούν την παραγωγή συγκεκριμένων διαγραμμάτων ακτινοβολίας, με χρήση απλών, ισοτροπικών ακτινοβολητών όπως αυτούς που θεωρήσαμε στην παρούσα Εργασία.

Chapter 2

Introduction

The concept of superradiant states, namely the coherent radiation from molecules within the volume of a gas has been first elaborated [8] as the summation of constructively interacting spontaneous emissions towards photon production. The principles of such a collective emission by atoms, leading to radiating resonances, instead of exponentially decaying intensities when working independently from each other, have been summarized in the quantum regime with the use of generic multilevel systems [9] and beam masers [10]. This effect can be interpreted in an optical manner in electromagnetically dense media [11], mesoscopic systems [12] and on-chip photonic crystal resonators [13]. Interestingly, the case of superradiance has been demonstrated in the simple case of two artificial atoms [14], as well as in arrays of quantum emitters [15] and random clouds of self-assembled quantum dots [16]. One may also visualize these superradiant regimes by regarding the material molecules as tiny antennas, operating in-phase with each other; such an interference produces power proportional to the square of particle population size [17], that pushes the performance of lasing [18] and imaging [19] to unprecedented levels.

Superradiation can be present even in non-quantum systems, like epsilon-near-zero plasmonic channels [20], nanofibers [21] and nanowaveguides [22]. Importantly, similar classical regimes have been detected in photonic crystals [23], materials operating near their band gaps [24] and plasmonic nanocavities [25]. Interfaces where surface plasmons are hosted constitute a privileged ground for the investigation of superradiation, since strong local fields are developed. In this way, the placement of numerous collaborating emitters near the boundaries of metallic nanoparticles [26], graphene [27] or nanowires [28] can send a large portion of the localized power far away. Moreover, significant radiation enhancement has been reported by randomly positioned nanorods in the vicinity of active, conjugately matched layers [29] and conversion of evanescent waves from poor emitters into propagating ones with the use of properly shaped hyperbolic metamaterial nanoprisms [30]. Finally, superradiation has also found extensive biomedical applications, from efficient radio-treatment of cancer with nanoparticles [31] to enhanced operation of Magnetic Resonance Imaging [32].

Several concepts involving the radiation, absorption and scattering mechanisms of objects interacting with electromagnetic waves, have been formulated in cylindrical geometries. In particular, nanorods have provided fertile ground towards designing biocompatible components via strong plasmonic fields [33] as well as efficient hybrid solar cells by tuning the exhibited bandgaps [34]. Moreover, short cylin-

drical dimers have been employed as optical nanoantennas producing high surface enhanced fluorescence [35] while ultraviolet lasing is achieved by nanowire arrays in room temperature [36]. Importantly, two major strategies in materializing transformation optics cloaks have been experimentally tested between circular boundaries, where exotic electromagnetic properties are emulated by spheroidal metallic inclusions [37] or concentric cylindrical lattices [38]. Nanotubes, namely, rolled monolayers of two-dimensional media, make an additional distinct category of cylindrical geometries that have been proven excellent candidates as supercapacitor electrodes for compact energy storage [39] and chemical sensors of high sensitivity [40]. Similarly, metasurfaces built on conformal curved films [41] are highly versatile in developing arbitrarily shaped multi-functional optical instruments [42] while golden microwedges patterning cylindrical lenses provide rollable substrates for tunable plasmonic devices [43]. Finally, cylindrical geometries with tunable interfaces can host a wide range of electromagnetic phenomena such as epsilon-near-zero originated waveguiding [44] and hyperbolic dispersion [45].

In this thesis, we have considered several cylindrical geometries to increase the far-field of a poor emitter resulting in electromagnetic superradiation. Starting from simpler and moving to more complicated structures with circular boundaries, we report significant enhancement for the radiation of filamentary currents in both polarizations. Similar aims have been well-served with the use of active quantum wells [46], hyperbolic resonators [47] and external DC biases [48], [49]. The most successful results are obtained when placing the free-standing source internally to plasmonic shells or between two concentric nanotubes, where multiple in-going and out-going modes optimally interfere with each other. The nanotubes can be well approximated by optically thin cylindrical layers of dense media like gallium phosphide or silver in the visible spectrum; they behave as homogenizable rolled metasurfaces. Several superradiating designs can give emission improvement of up to 3 orders of magnitude, by developing extremely powerful omnidirectional or bipolar modes different for each wave polarization, both in the far and the near region. The observed radiation is on par with or even greater than previous relevant works.

Additionally, the designs in which plasmonic materials are employed offer several advantages over traditional plasmonic nanoantennas. The most widespread plasmonic antennas consist of a quantum emitter coupled to either a single metallic nanorod [50], [51], [52] or a pair of nanorods, through a gap between them [50], [51], [53]. While these designs can result in significant radiation enhancement, they are not capable of substantially boosting both excitation polarizations concurrently [51]; on the other hand, our proposed highly-performing setups enhance both TM and TE waves at the same time, to levels on par with, or greater than those reported in earlier works. Additionally, our best performers reveal strong omnidirectional or bipolar patterns, different for each polarization type. Consequently, not only can our designs be used for emission enhancement but they may also be utilized as polarization sensors, in an analog signal processing scheme. Furthermore, nanoantennas of the above-mentioned geometries are inherently bulky [54], [55] and their fabrication can be challenging [50]; in our work, we observe substantial amplification of the radiative power while also maintaining the geometries as simple as possible, allowing for a simplified fabrication of the photonic devices. Moreover, bowtie and narrow-gap dimer antennas can suffer from nonlocal effects, which may significantly decrease their radiation enhancement [56]. Specifically, in these setups, the source is

squeezed between sharp tips or nanogaps, resulting in strong field localization and steep field gradients, which in turn activate nonlocalities. This is not the case for our designs; the radiation enhancement is not due to extreme field localization at a geometric singularity but rather due to the constructive interference of low-order azimuthal modes within the cavity, stemming from a resonant coupling between the two metasurfaces. Thus, the proposed configurations are naturally less sensitive to nonlocal effects. Apart from the nanodimer geometries described above, some other configurations have previously been proposed in the literature for the construction of plasmonic antennas, using plasmonic nanopatches [57] or ring cavities [58]. However, while they can achieve significant emission enhancement, they both employ multiple quantum dots. In contrast, in our designs we use a single weak isotropic source. As a result, we can ensure coherent emission, owing to the single active part, while also observing comparable or improved performance using fewer resources.

As far as the chosen excitations (line sources) are concerned, they have served as well-established models in the study of a variety of problems in the literature, despite their idealized nature. Some of these cases include, but are not limited to, the design of cylindrical nanoparticles [59], the study of electromagnetic scattering from a DNG slab [60], as well as the analysis of the behavior of cylindrical invisibility cloaks [61]. Furthermore, line sources can serve as models for radiators that are two-dimensional in nature and are widely employed in modern technologies. More specifically, slot antennas can be modeled as line sources; in cases where the slots are narrow and long, they behave like a cylindrical wave emitter in the plane perpendicular to the slot. In a similar fashion, waveguide apertures can also be modeled as 2D cylindrical radiators. Additionally, line sources are not just an abstraction used for practicality in two-dimensional analyses; they help us capture the core physical mechanisms that govern the interaction between the source and the cylindrical geometries through simple, analytical formulas. Hence, the results obtained using this 2D model can often be translated and generalized to 3D scenarios or provide valuable intuition for them. For instance, if we were to use a dipole instead of a line source, the behavior that would be captured on the transverse plane would be similar to the one observed in our paper.

Chapter 3

Theoretical Framework

3.1 Maxwell's Equations

A detailed description of the operation of photonic devices, and in fact all electromagnetic phenomena, requires a rigorous formulation of the laws that govern electromagnetism. Originally developed by James Clerk Maxwell in 1873, the equations presented below describe the relation between the electromagnetic field and its sources. These equations read:

$$\nabla \times \boldsymbol{\mathcal{E}} = -\frac{\partial \boldsymbol{\mathcal{B}}}{\partial t} \tag{3.1}$$

$$\nabla \times \boldsymbol{\mathcal{H}} = \boldsymbol{\mathcal{J}} + \frac{\partial \boldsymbol{\mathcal{D}}}{\partial t} \tag{3.2}$$

$$\nabla \cdot \boldsymbol{\mathcal{D}} = \varrho \tag{3.3}$$

$$\nabla \cdot \boldsymbol{\mathcal{B}} = 0, \tag{3.4}$$

where $\boldsymbol{\mathcal{E}}$ is the electric field, $\boldsymbol{\mathcal{H}}$ the magnetic field, $\boldsymbol{\mathcal{D}}$ the electric flow density, $\boldsymbol{\mathcal{B}}$ the magnetic flow density, $\boldsymbol{\mathcal{J}}$ the surface current density and ϱ the charge density. All of the aforementioned quantities are, naturally, functions of space and time $(\mathbf{r}, t)$. Additionally, an equation describing the relation between the sources, known as the continuity equation,was also developed by Maxwell:

$$\nabla \cdot \boldsymbol{\mathcal{J}} + \frac{\partial \varrho}{\partial t} = 0. \tag{3.5}$$

The aforementioned set of equations is known as the differential form of Maxwell's equations. A representation in integral form also exists but it is not given here since it will not be utilized in the analysis of the examined structures. It can be proven that only two of Maxwell's equations are independent ((3.1), (3.2)), when the time-dependent case is considered [62]. Therefore, in order for the system of $\{\boldsymbol{\mathcal{E}}, \boldsymbol{\mathcal{H}}, \boldsymbol{\mathcal{D}}, \boldsymbol{\mathcal{B}}\}$ to be solvable, two additional equations are needed, known as the constitutive relations:

$$\boldsymbol{\mathcal{D}} = \varepsilon\varepsilon_0 \boldsymbol{\mathcal{E}} \tag{3.6}$$

$$\boldsymbol{\mathcal{B}} = \mu\mu_0 \boldsymbol{\mathcal{H}}, \tag{3.7}$$

where ε_0 is the permittivity and μ_0 the permeability of vacuum; ε and μ are called relative permittivity and relative permeability respectively. These two relative quantities describe the properties of the material in which the electromagnetic field is

measured. Generally, they can be functions of space, time or even the fields themselves. In anisotropic media, ε and μ are tensors. However, in this work only linear, isotropic, homogeneous and non-dispersive media are studied; therefore, ε and μ are constants. Moreover, all media studied in this thesis are non-magnetic; consequently, $\mu = 1$.

Maxwell's equations can be further simplified, when time harmonic sources are considered, i.e. the sources are sinusoidal functions of angular frequency ω. In this case, the produced fields are time harmonic themselves. Any time harmonic field $\boldsymbol{\mathcal{F}}(\boldsymbol{r}, \boldsymbol{t})$ may be described by the following equation [62]:

$$\boldsymbol{\mathcal{F}}(\boldsymbol{r}, t) = \mathrm{Re}[\boldsymbol{F}(\boldsymbol{r})\, e^{\mathrm{i}\omega t}], \tag{3.8}$$

where $\boldsymbol{F}(\boldsymbol{r})$ is a complex vector called the phasor of $\boldsymbol{\mathcal{F}}$. Working with phasors, it is easily proven that $\partial/\partial t \rightarrow \mathrm{i}\omega$. It is important to note that when the sources are not monochromatic, the quantity $\boldsymbol{F}(\boldsymbol{r})$ is the Fourier transform of $\boldsymbol{\mathcal{F}}(\boldsymbol{r}, t)$ [62]. In any case, Maxwell's equations are transformed as follows:

$$\nabla \times \boldsymbol{E} = -\mathrm{i}\omega \boldsymbol{B} \tag{3.9}$$

$$\nabla \times \boldsymbol{H} = \boldsymbol{J} + \mathrm{i}\omega \boldsymbol{D} \tag{3.10}$$

$$\nabla \cdot \boldsymbol{D} = \rho \tag{3.11}$$

$$\nabla \cdot \boldsymbol{B} = 0. \tag{3.12}$$

An additional constitutive relation, called microscopic Ohm's law, can be considered in the cases of lossy media, connecting the surface current $\boldsymbol{J}$ and the electric field $\boldsymbol{E}$ [63]. It reads:

$$\boldsymbol{J} = \sigma \boldsymbol{E}, \tag{3.13}$$

where σ is the conductivity (per unit length) of the medium. Substituting (3.13) in (3.10), a complex relative permittivity $\varepsilon' = \varepsilon - \mathrm{i}\sigma/(\omega\varepsilon_0)$ may be defined, transforming (3.10) to:

$$\nabla \times \boldsymbol{H} = \mathrm{i}\omega\varepsilon'\varepsilon_0 \boldsymbol{E}. \tag{3.14}$$

In what follows, the prime symbol may be dropped and the complex relative permittivity will be described as $\varepsilon = \mathrm{Re}[\varepsilon] + \mathrm{iIm}[\varepsilon]$.

3.2 The Helmholtz Equation

The Helmholtz Equation is the differential equation that describes waves in the frequency domain (or in the Fourier domain). It can easily be derived from Maxwell's equations. In particular, considering a source-free medium, with the properties discussed in the previous section (i.e. $\nabla \cdot \boldsymbol{E} = 0$, $\nabla \cdot \boldsymbol{H} = 0$), and by taking the curl of (3.9) and (3.14), we obtain:

$$(\nabla^2 + k^2)\boldsymbol{F} = \boldsymbol{0}, \tag{3.15}$$

where $\boldsymbol{F} = \boldsymbol{E}, \boldsymbol{H}$ and $k = \omega\sqrt{\varepsilon}$ is the wavenumber of the medium. In all problems presented in this thesis, the cylindrical coordinate system is utilized; i.e. $\boldsymbol{F} = \boldsymbol{F}(r, \varphi, z) = F_r(r, \varphi, z)\, \hat{\boldsymbol{r}} + F_\varphi(r, \varphi, z)\, \hat{\boldsymbol{\varphi}} + F_z(r, \varphi, z)\, \hat{\boldsymbol{z}}$, where $r = \sqrt{x^2 + y^2}$, $\varphi = \tan^{-1}(y/x)$. It is easily proven that for the z component of the fields, the following relation holds:

$$(\nabla^2 + k^2)F_z = 0. \tag{3.16}$$

The above equation is known as the scalar Helmholtz Equation. It is of particular importance in our study since in each considered setup two types of excitation will be studied; TM excitation ($\boldsymbol{E} = \hat{\boldsymbol{z}}E_z$, $H_z = 0$) and TE excitation ($\boldsymbol{H} = \hat{\boldsymbol{z}}H_z$, $E_z = 0$). In each scenario, the z components will be obtained by solving (3.16), while the other remaining components will be found using (3.9) and (3.10).

It becomes evident that a solution to (3.16) needs to be developed. To this end, we let $F_z = \psi$. Moreover, we notice that the solutions shall be independent of z ($\partial/\partial z = 0$), since the structures studied are all infinite along the z-axis. Consequently, ψ is a function of (r, φ) and (3.16) becomes:

$$\left(\frac{1}{r}\frac{\partial}{\partial r}\left(r\frac{\partial}{\partial r}\right) + \frac{1}{r^2}\frac{\partial^2}{\partial \varphi^2} + k^2\right)\psi(r,\varphi) = 0. \tag{3.17}$$

By the method of separation of variables (a detailed analysis is given in Appendix A), we obtain solutions of the form:

$$\psi_n(r,\varphi) = R_n(r)e^{\mathrm{i}n\varphi}, \tag{3.18}$$

where n is an integer since the field is 2π periodic with respect to φ. Furthermore, $R_n(r)$ is a solution to the Bessel equation:

$$\left(r\frac{\partial}{\partial r}\left(r\frac{\partial}{\partial r}\right) + (kr)^2 - n^2\right)R_n(r) = 0. \tag{3.19}$$

The general solution $R_n(r)$ of the above equation is a linear combination of either the Bessel function $J_n(kr)$, the Neumann function $Y_n(kr)$, the Hankel function of the first kind $H_n^{(1)}(kr)$ or the Hankel function of the second kind $H_n^{(2)}(kr)$ [62]. The solution that is selected each time is governed by the respective boundary conditions that we impose. Specifically, $H_n^{(2)}(kr) = J_n(kr) - \mathrm{i}Y_n(kr)$ represents cylindrical waves traveling outwards (when an $\exp(+\mathrm{i}\omega t)$ time dependence is used), while $H_n^{(1)}(kr) = J_n(kr) + \mathrm{i}Y_n(kr)$ represents cylindrical waves traveling inwards (using the aforementioned time dependence). Both $J_n(kr)$ and $Y_n(kr)$ are used to describe standing cylindrical waves. Naturally, the general solution ψ of (3.16) will be a superposition of all eigensolutions ψ_n:

$$\psi(r,\varphi) = \sum_{n=-\infty}^{+\infty} c_n R_n(r)\, e^{\mathrm{i}n\varphi}, c_n \in \mathbb{C}. \tag{3.20}$$

3.3 Boundary Conditions

Now that the form of the general solutions of the wave equation for both types of polarization has been established, we will examine the boundary conditions which are used to determine the unknown coefficients c_n.

Let us consider two media (Medium 1 and Medium 2), separated by an interface, as shown in Fig. 3.1. The unit vector $\hat{\boldsymbol{n}}$ is perpendicular to the interface and directed from Medium 1 to Medium 2. Let us also assume that in the general case, a surface current $\boldsymbol{J}_{\mathrm{S}}$ exists on the boundary. The two independent boundary conditions (regarding the electric and magnetic field respectively) can be found by

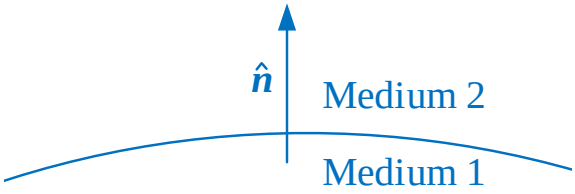

Figure 3.1: An interface between two different media (Medium 1 and Medium 2). The unit vector $\hat{\boldsymbol{n}}$ is normal to the interface.

a proper application of (3.9) and (3.10) (in integral form) [64]. The one concerning the electric field reads:

$$\hat{\boldsymbol{n}} \times (\boldsymbol{E}_2 - \boldsymbol{E}_1) = \boldsymbol{0}, \tag{3.21}$$

while the one concerning the magnetic field is given by:

$$\hat{\boldsymbol{n}} \times (\boldsymbol{H}_2 - \boldsymbol{H}_1) = \boldsymbol{J}_{\mathrm{S}}. \tag{3.22}$$

Note that the vector $\hat{\boldsymbol{n}} \times \boldsymbol{F}$, where $\boldsymbol{F}$ is a vector field, is the tangential component of $\boldsymbol{F}$ to the surface on which $\hat{\boldsymbol{n}}$ is normal. Therefore, we notice that the tangential component of the electric field is continuous, while the tangential component of the magnetic field is discontinuous, owning to the surface current $\boldsymbol{J}_{\mathrm{S}}$ that may exist on the boundary.

In some of the structures studied in this thesis, the interface between the two media will be a metasurface of complex surface conductivity σ. In this case, the developed surface current on the metasurface is proportional to the local electrical field [65]; specifically, $\boldsymbol{J}_{\mathrm{S}} = -\sigma \hat{\boldsymbol{n}} \times (\hat{\boldsymbol{n}} \times \boldsymbol{E})$, functioning as a voltage-controlled current source. Consequently, the condition describing the discontinuity of the magnetic field now reads:

$$\hat{\boldsymbol{n}} \times (\boldsymbol{H}_2 - \boldsymbol{H}_1) = -\sigma \hat{\boldsymbol{n}} \times (\hat{\boldsymbol{n}} \times \boldsymbol{E})\,. \tag{3.23}$$

Having established the boundary conditions that will be utilized in the calculation of the unknown coefficients, we will now proceed to study the fields produced by the type of source used in all examined problems, the infinite TM/TE line source.

3.4 The Infinite Line Source

We consider an infinite line source of TM or TE type that is parallel to the z axis and positioned at $\boldsymbol{r}' = x'\hat{\boldsymbol{x}} + y'\hat{\boldsymbol{y}}$ in free space, as shown in Fig. 3.2. Essentially, the line source is a thin wire, assumed to be infinite. In the case of TM-type (or electric current) sources, there is an electric current I_{e} (measured in A) along the wire and the produced electric field is parallel to the z axis. On the contrary, TE-type (or magnetic current) sources have a magnetic current I_{m} (measured in V) and produce a magnetic field parallel to the z axis. One could say that the magnetic current source is the dual of the electric one, since the former is fed by a magnetic current and produces a magnetic field parallel to it while the latter is fed by an electric current and produces a respective electric field.

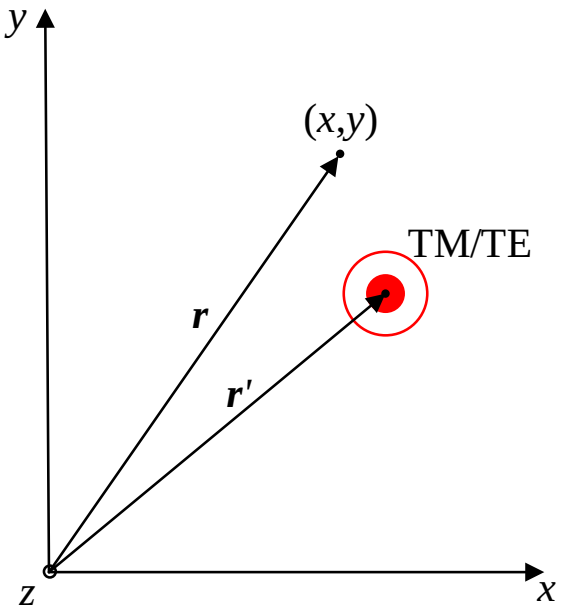

Figure 3.2: An infinite line source of TM/TE type, parallel to the z axis, positioned at $\boldsymbol{r}' = x'\hat{\boldsymbol{x}} + y'\hat{\boldsymbol{y}}$. The electromagnetic field is calculated at the observation point $\boldsymbol{r} = x\hat{\boldsymbol{x}} + y\hat{\boldsymbol{y}}$.

Regarding the fields that are radiated by the line source, these can easily be found for each respective type of source [64]. Specifically, a TM line source produces the following electric field:

$$\boldsymbol{E}_{\text{inc}}^{\text{TM}} = -\hat{\boldsymbol{z}}\frac{k_0\eta_0 I_{\text{e}}}{4}H_0^{(2)}\left(k_0|\boldsymbol{r}-\boldsymbol{r}'|\right), \tag{3.24}$$

where k_0 is the wavenumber of vacuum and η_0 its wave impedance. In a similar fashion, the magnetic field radiated from a magnetic line source is given by:

$$\boldsymbol{H}_{\text{inc}}^{\text{TE}} = -\hat{\boldsymbol{z}}\frac{k_0 I_{\text{m}}}{4\eta_0}H_0^{(2)}\left(k_0|\boldsymbol{r}-\boldsymbol{r}'|\right). \tag{3.25}$$

Although we mostly examine cylindrical structures (hence the cylindrical coordinate system is heavily utilized), it is important to note that the electromagnetic field of the line source can also be expressed in the cartesian coordinate system with a Sommerfeld integral [66]:

$$H_0^{(2)}\left(k_0|\boldsymbol{r}-\boldsymbol{r}'|\right) = \int_{-\infty}^{+\infty}\frac{\mathrm{i}e^{-\kappa(\beta)|y-y'|}e^{-\mathrm{i}\beta(x-x')}}{\pi\kappa\left(\beta\right)}\mathrm{d}\beta, \tag{3.26}$$

where $\kappa\left(\beta\right) = \sqrt{\beta^2 - k_0^2}$. Although this expression is not useful when cylindrical configurations are considered, it can be useful for computing the radiation of a line source in the vicinity of planar surfaces. We will utilize it later in this thesis to analyze the behavior of a line source near a planar metasurface, where the above representation will be crucial in understanding the physics behind said behavior. Nevertheless, the calculation of such integrals poses significant mathematical challenges (as a result of the two poles at $\beta = \pm k_0$).

In this thesis, we are primarily concerned about the power radiated into infinity in each examined structure. Therefore, it is essential to calculate the power radiated

by a single, free-standing line source, in order to find the enhancement in power that each configuration is able to produce. In what follows, the power (per unit length z) emitted from a line source that is alone in free space will be indicated as P_{inc}. P_{inc} can be found by applying Poynting's theorem over a circle of infinite radius r, centered at the origin:

$$P_{\text{inc}} = \lim_{r\to\infty} \int_0^{2\pi} \left(\frac{1}{2} \boldsymbol{E} \times \boldsymbol{H}^* \right) \cdot \hat{\boldsymbol{r}} r \mathrm{d}\varphi, \tag{3.27}$$

where $*$ indicates complex conjugation. The above integral can be easily evaluated, when the following points are taken into account. Firstly, note that the total power emitted by a line source will be the same independent of where it is positioned. Therefore, without loss of generality we can assume that the source is placed at the origin. Secondly, since the radius of the circle is infinite, we can use the asymptotic expansions of the Hankel functions for large arguments. In this case, we obtain the far-field equations. It can be proven that in the far-field region, the electromagnetic waves behave locally like plane waves [64]. Consequently, the complex Poynting vector in the far-field region is equal to:

$$\boldsymbol{N} = \frac{1}{2} \boldsymbol{E} \times \boldsymbol{H}^* = \frac{|\boldsymbol{E}|^2}{2\eta_0} \hat{\boldsymbol{r}} = \frac{|\boldsymbol{H}|^2 \eta_0}{2} \hat{\boldsymbol{r}}. \tag{3.28}$$

The Hankel function of the second kind and order zero, has the following asympotic expansion for large arguments $x \to \infty$: $H_0^{(2)}(x) \cong e^{-\mathrm{i}x} \sqrt{2\mathrm{i}/(\pi x)}$ [2]. This expression is indicative of the cylindrical wave nature of the $H_n^{(2)}$ function; it represents a wave traveling outwards ($e^{-\mathrm{i}x}$) with its amplitude decreasing as $1/\sqrt{x}$. Additionally, by inspection of (3.28), one observes that the power radiated from an infinite line source in the far-field region is invertly proportionate to r^2, as in all cylindrical waves.

By substituting (3.28) in (3.27), using the aforementioned asymptotic expansion and integrating over the circle, we obtain the following expressions for the radiated power:

$$P_{\text{inc}}^{\text{TM}} = \frac{k_0 \eta_0 I_{\text{e}}^2}{8}, \quad P_{\text{inc}}^{\text{TE}} = \frac{k_0 I_{\text{m}}^2}{8\eta_0}. \tag{3.29}$$

However, in this thesis we are only interested in the enhancement of power that is observed in each proposed structure, relative to a free-standing line source. Therefore, we are only interested in the relative quantity $P_{\text{rad}}/P_{\text{inc}}$, where P_{rad} is the total power radiated from the structure, when illuminated by a line source identical to the free-standing one, with the latter producing P_{inc}. As a result, the quantity $P_{\text{rad}}/P_{\text{inc}}$ will be independent of the electric or magnetic current used. Consequently, we pick the currents so that $\boldsymbol{E}_{\text{inc}}^{\text{TM}}$ and $\boldsymbol{H}_{\text{inc}}^{\text{TE}}$ are of unitary amplitude; by inspection of (3.24) and (3.25), we select $I_{\text{e}} = (1\text{V/m}) \times 4/(\text{k}_0\eta_0)$ and $I_{\text{m}} = (1\text{A/m}) \times 4\eta_0/\text{k}_0$. Taking this into account, in what follows, the incident power P_{inc} will be given by:

$$P_{\text{inc}}^{\text{TM}} = \frac{2}{k_0\eta_0} \times (1\text{V/m})^2, \quad P_{\text{inc}}^{\text{TE}} = \frac{2\eta_0}{k_0} \times (1\text{A/m})^2. \tag{3.30}$$

3.5 Calculation of the Relative Power

Up to this point, we have established the basic theoretical framework, upon which we have constructed the general solutions to the wave equation in cylindrical coordinates

and have calculated the power emitted from a line source that is alone in free space. In the final section of this chapter, we will describe the form of the configurations that will be examined in the rest of the thesis and introduce the metric that will be used in evaluating their performance.

In Fig. 3.3, we present two representative radiation-enhancing structures. Specifically, in Fig. 3.3(a), we show a hollow cylinder of internal radius g and external radius a filled with a material of complex relative permittivity ε, while in Fig. 3.3(b) we depict two concentric nanotubes at $r = g, a$ with the same complex surface conductivity σ. Both the setups are infinite along the z axis and excited by free-standing line sources positioned along axis $(r, \varphi) = (L, 0)$ that can be either of TM (electric field $\mathbf{E}$ parallel to z axis) or TE (magnetic field $\mathbf{H}$ parallel to z axis) type. Both of them produce cylindrical waves that oscillate with wavelength λ. All examined structures will be of similar kind; cylindrical geometries excited by a line source positioned at $(r, \varphi) = (L, 0)$ in vacuum.

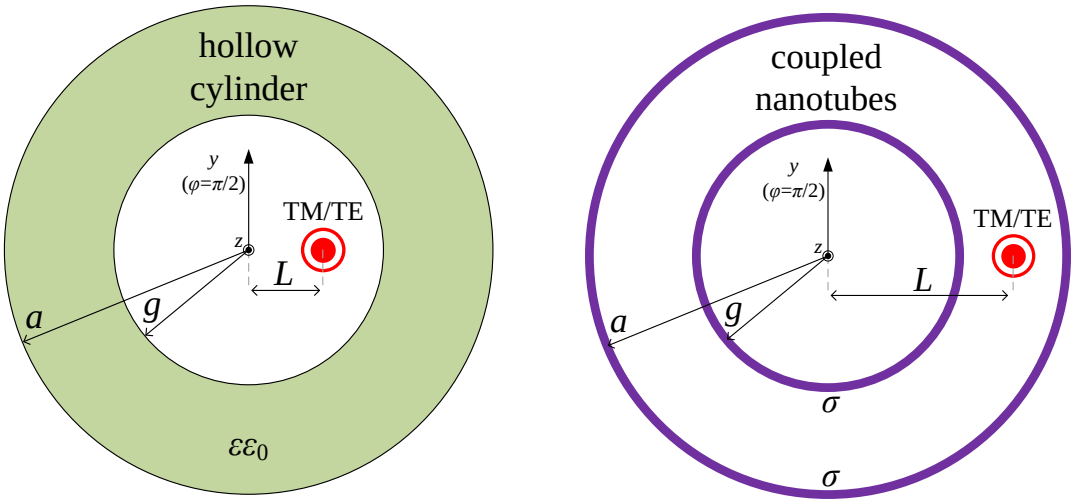

(a) (b)

Figure 3.3: Two representative radiation-enhancing structures excited by TM/TE line sources. Both are defined by cylindrical boundaries of internal radius g and external radius a. (a) A hollow cylinder with dielectric shell of relative complex permittivity ε. (b) A pair of coupled nanotubes with complex surface conductivity σ. The source must be positioned into vacuum.

As discussed in the previous section, we are interested in the relative power $P_{\text{rad}}/P_{\text{inc}}$ of each structure, where P_{rad} is the total power radiated by the setup and P_{inc} is the power emitted from the source when being alone in free-space. Therefore, we need to calculate the electromagnetic field in the region external to the structures ($r > a$ in Figs. 3.3(a) and 3.3(b)). In order to conveniently determine the fields in this region, we need to expand (3.24) and (3.25) in cylindrical eigenfunctions. The notation F will be utilized for the respective z-directed field: electric field $F = E_z^{\text{TM}}$ for TM waves, magnetic field $F = H_z^{\text{TE}}$ for TE waves. This can be done using the addition theorem of Hankel functions [64]. Specifically, (3.24) and (3.25) can be

written as [1]:

$$F_{\text{inc}} = \sum_{n=-\infty}^{+\infty} H_n^{(2)}(k_0 \max(L,r)) J_n(k_0 \min(L,r)) e^{\mathrm{i}n\varphi}, \tag{3.31}$$

where the fields are chosen to have unitary amplitude for the reasons described in the previous section. In each of the regions of the examined structures, the fields are expanded using the proper eigensolutions (i.e. the proper Bessel functions). Regarding the external region specifically, the total fields are given by:

$$F_{\text{rad}} = \sum_{n=-\infty}^{+\infty} C_n H_n^{(2)}(k_0 r) e^{\mathrm{i}n\varphi}, \tag{3.32}$$

where C_n are complex coefficients determinable by the boundary conditions. The above solution is selected so as to describe a cylindrical wave radiating outwards.

Now that the form of the radiating field outside the structure has been given, we can calculate the total radiated power P_{rad} in the same way that we calculated the incident one; by applying the Poynting theorem over a circle of infinite radius centered at the origin (as in (3.27)). Again, the asymptotic form of $H_n^{(2)}$ for large arguments will be used, yielding $F_{\text{rad}}(r \to \infty) = \sum_{n=-\infty}^{+\infty} C_n \sqrt{2\mathrm{i}/(\pi k_0 r)} e^{-\mathrm{i}k_0 r} e^{\mathrm{i}n\varphi}$. It is evident that for both polarizations, the solution will be proportional to the following integral:

$$I = \int_0^{2\pi} f(r,\varphi)\,\mathrm{d}\varphi, \tag{3.33}$$

where $f(r,\varphi) = |F_{\text{rad}}(r \to \infty, \varphi)|^2 r$.

Specifically, by substituting (3.28) in (3.27), we obtain $P_{\text{rad}}^{\text{TM}} = I/(2\eta_0)$ and $P_{\text{rad}}^{\text{TE}} = I\eta_0/2$. The integrand function $f(r,\varphi)$, using the proper asymptotic form of the Hankel function: $H_n^{(2)}(x) \cong \sqrt{2/(\pi k_0 r)} e^{-\mathrm{i}(x - n\pi/2 - \pi/4)}$ [2], is expanded as:

$$f(r,\varphi) = \frac{2}{\pi k_0} \sum_{n=-\infty}^{+\infty} \sum_{m=-\infty}^{+\infty} \mathrm{i}^{(n-m)} C_n C_m^* e^{\mathrm{i}(n-m)\varphi}. \tag{3.34}$$

Interchanging the orders of integration and summation, we obtain the following expression for I:

$$I = \frac{2}{\pi k_0} \sum_{n=-\infty}^{+\infty} \sum_{m=-\infty}^{+\infty} \mathrm{i}^{(n-m)} C_n C_m^* \int_0^{2\pi} e^{\mathrm{i}(n-m)\varphi} \mathrm{d}\varphi. \tag{3.35}$$

Using the orthogonality property of complex exponentials:

$$\int_0^{2\pi} e^{\mathrm{i}(n-m)\varphi} \mathrm{d}\varphi = \begin{cases} 2\pi, & n = m \\ 0, & n \neq m \end{cases}, \tag{3.36}$$

we arrive at:

$$I = \frac{4}{k_0} \sum_{n=-\infty}^{+\infty} |C_n|^2. \tag{3.37}$$

Consequently, the radiated power for TM polarization will be given by $P_{\text{rad}}^{\text{TM}} = (2/(k_0\eta_0)) \sum_{n=-\infty}^{+\infty} |C_n|^2$, while in the TE-excited scenario the total emitted power

is equal to $P_{\text{rad}}^{\text{TE}} = (2\eta_0/k_0)\sum_{n=-\infty}^{+\infty}|C_n|^2$. By inspection of (3.30), it becomes evident that in both cases, the relative power is easily found as:

$$\frac{P_{\text{rad}}}{P_{\text{inc}}} = \sum_{n=-\infty}^{+\infty}|C_n|^2. \tag{3.38}$$

Moving forward, our major objective will be to find structural and textural combinations for the considered layout so that the relative power $P_{\text{rad}}/P_{\text{inc}}$ takes substantial values, even for a single positioning of the dipole into a vacuum area. In other words, we aim at evaluating the quantity:

$$\rho = \max_{L}\left\{P_{\text{rad}}/P_{\text{inc}}\right\}, \tag{3.39}$$

for $0 \leq L < +\infty$, as long as the (TM or TE) exciting current is surrounded by air.

The proposed metric expresses the ability of the structure, built around the free-standing source, to efficiently transfer the emitted power to infinity. Therefore, we are searching for smart designs that, when put next to poor emitters, boost substantially their radiating power. In what follows, the complex coefficients C_n will be found by the boundary conditions (a more detailed analysis can be found in Appendix B) and the relative power will be obtained by (3.38). Then, the parametric space will be extensively searched, so as to arrive at substantial values of ρ.

It is important to note that ρ is not equal to the radiation efficiency, as defined in antenna theory [67]. Instead, it can (and should) be larger than unity, since the denominator P_{inc} in (3.39) refers to the field (3.31) produced by the source when being alone in free-space without taking into account the radiation-enhancing structure.

Chapter 4

PEC and Solid Rods

4.1 Infinite PEC Planes and PEC Cylinders

Now that we have established the theoretical framework needed for the evaluation of the performance of each proposed device, we are ready to start examining various configurations, starting from the simplest possible scatterer, a PEC cylinder. However, before moving to the case of the PEC Cylinder, it would be meaningful to solve an even simpler problem in order to obtain insight that will be useful for the rest of this thesis. Specifically, we would like to compute the power radiated from a line source positioned above an infinite PEC plane, as shown in Fig. 4.1.

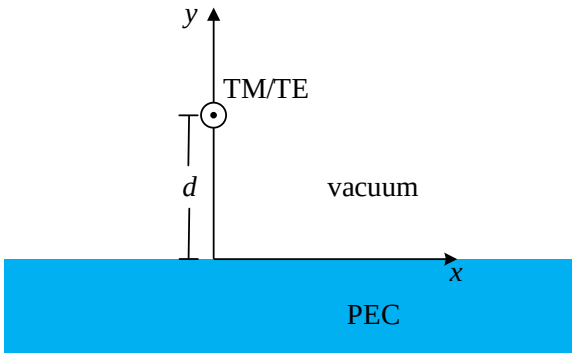

Figure 4.1: An infinite line source, positioned at distance d above an infinite PEC plane.

This problem can easily be solved by using image theory [64]. The images of each type of source into the PEC plane are presented in Fig. 4.2. More specifically, we observe that in order to satisfy the boundary condition $\hat{\boldsymbol{y}} \times \boldsymbol{E} = \boldsymbol{0}$ at the interface, one needs to consider a source fed by an opposite current in the TM case, while in the TE case a source fed by a current identical to that of the original source is needed. Both images are positioned at $y = -d$. It should be noted that the fields obtained in the two geometries of 4.2 is valid only in the upper half-plane, while the fields in the lower half-plane are zero, since it is occupied by a perfect electric conductor.

Once again, to calculate the total radiated power, we will find the fields in the far-field region and then apply Poynting's theorem. However, in the considered

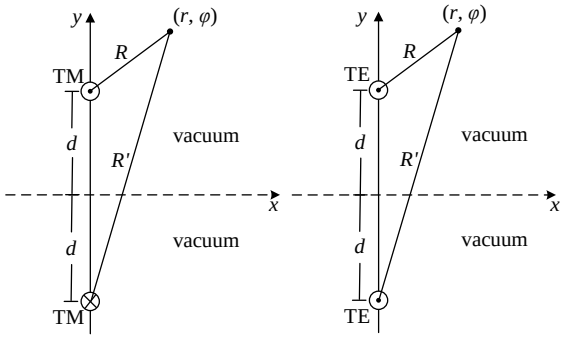

Figure 4.2: The developed images of the line source shown in Fig. 4.1, with respect to the infinite plane PEC. The left part depicts a TM source and the right part a TE source.

case the total power is concentrated solely on the upper half-plane ($0 \leq \varphi \leq \pi$); therefore, we need to integrate over a semi-circle of infinite radius, centered at the origin ($P_{\text{rad}} = \int_0^\pi \boldsymbol{N} \cdot \hat{\boldsymbol{r}} r \mathrm{d}\varphi$). Regarding the fields let us consider a point (r, φ), R the distance of the point from the original source and R' the distance of the point from the image source. When $r \to \infty$, the following approximation can be derived [64]: $R = r - d\sin\varphi$, $R' = r + d\sin\varphi$. Then, by considering the asymptotic form of the $H_0^{(2)}$ function, we obtain a far-field expression for the z components of the fields in the upper half-plane [64]:

$$F_{\text{rad}} = e^{-\mathrm{i}k_0 r}\sqrt{\frac{\mathrm{i}}{2\pi k_0 r}} \cdot \begin{cases} -\mathrm{i}\sin\left(k_0 d\sin\varphi\right), & \text{TM waves} \\ \cos\left(k_0 d\sin\varphi\right), & \text{TE waves} \end{cases} . \tag{4.1}$$

Using the local plane wave behavior in the far-field in the expression of the complex Poynting vector (3.28), we arrive at the following expression:

$$P_{\text{rad}} = \frac{2P_{\text{inc}}}{\pi} \cdot \begin{cases} \int_0^\pi \sin^2\left(k_0 d\sin\varphi\right)\mathrm{d}\varphi, & \text{TM waves} \\ \int_0^\pi \cos^2\left(k_0 d\sin\varphi\right)\mathrm{d}\varphi, & \text{TE waves} \end{cases} . \tag{4.2}$$

The above integrals may be calculated by utilizing an integral representation of the J_0 function [2]:

$$J_0\left(z\right) = \frac{1}{\pi}\int_0^\pi \cos\left(z\cos\varphi\right)\mathrm{d}\varphi, \tag{4.3}$$

after using proper trigonometric formulas in the integrand functions: $\sin^2 z = 1 - \cos^2 z = \left(1 - \cos(2z)\right)/2$. The resulting formula for the relative power is the following:

$$\frac{P_{\text{rad}}}{P_{\text{inc}}} \cong \begin{cases} 1 - J_0(2k_0 d), & \text{TM waves} \\ 1 + J_0(2k_0 d), & \text{TE waves} \end{cases} . \tag{4.4}$$

This formula captures the essence of the behavior of the images. Specifically, we notice that when the source is placed exactly on top of the interface ($d = 0$), the TM radiated power nullifies, while the TE radiated power is doubled (and maximized); this happens because the TM image is fed by an opposite current, while the TE image is fed by the current of the original source.

At this point we are ready to study the performance of a simple design consisting of a PEC cylinder of radius a, with the source positioned at distance L from its center

($L > a$), as shown in Fig. 4.3. Conclusions of particular importance can be derived using (4.4) for $d = L - a$. Indeed, (4.4) constitutes a good approximation for the PEC Cylinder case, when $a/\lambda \gg 1$ and $L \to a$; if the source is in the vicinity of the PEC interface. it "senses" the cylinder as an infinite planar surface.

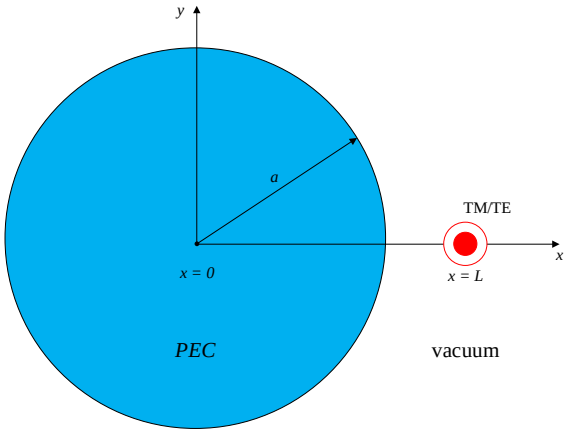

Figure 4.3: A PEC cylinder of radius a, centered at the origin. The source is positioned at distance L from the cylinder's center.

In Fig. 4.4(a), we depict the relative power $P_{\text{rad}}/P_{\text{inc}}$ emitted by the TM source on the $(a/\lambda, L/a)$ plane for the previous geometry. We observe a small enhancement of approximately 1.4. Additionally, we notice that $P_{\text{rad}} = 0$ when the source approaches the surface of the cylinder. Both of these facts can be explained by (4.4); $P_{\text{rad}} = 0$ when $L - a \to 0$ since $J_0(0) = 1$ and P_{rad} is maximized and equal to approximately 1.4 at the first point of minimization of J_0. On the other hand, Fig. 4.4(b) shows the relative power $P_{\text{rad}}/P_{\text{inc}}$ of a TE-polarized source on the same map. We notice that in this case, the maximum value of the total radiated power is double the incident one. In fact, this happens when the TE source is positioned directly on top of the PEC interface. Once again, (4.4) offers valuable insight; when $L - a \to 0$, the aforementioned formula predicts that $P_{\text{rad}}/P_{\text{inc}} = 1 + J_0(0) = 2$.

4.2 Solid Rods

It becomes evident that PEC structures cannot significantly enhance the radiated power of a line source. Therefore, we need to turn to other structural alternatives. Our next configuration is similar to that of the PEC cylinder; we now consider a solid cylinder of radius a, filled with a medium of complex relative permittivity $\varepsilon = \text{Re}[\varepsilon] + \text{iIm}[\varepsilon]$, as shown in Fig. 4.5. Once again, the source is positioned outside the cylinder, at distance L from its center. This thesis is primarily concerned with operating the devices at the optimal regime which results in maximal total radiation; thus, we need to consider lossless cases ($\text{Im}[\varepsilon] = 0$). However, in what follows small losses are used to avoid numerical issues that may arise in certain cases. Specifically, the use of lossless ENZ materials or materials with $\varepsilon = -1$ may lead to unrealistic resonances that we would like to avoid. Therefore, we employ a small and constant imaginary part ($\text{Im}[\varepsilon] = -0.03$) for the relative permittivity, in all of the cases that follow.

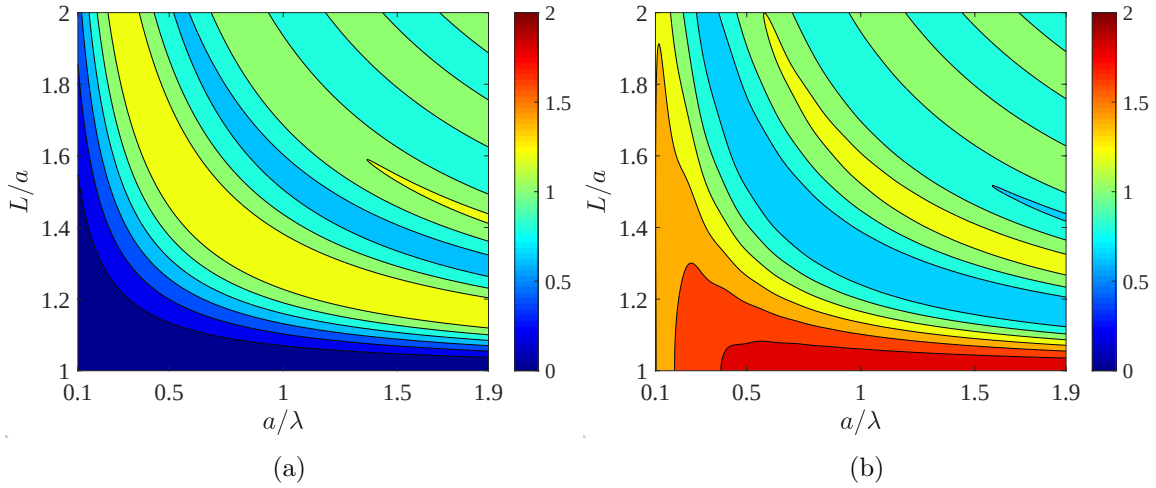

Figure 4.4: The relative power $P_{\text{rad}}/P_{\text{inc}}$ for a PEC cylinder of radius a represented with respect to the electrical size a/λ and normalized position of the source L/a. (a) TM waves, (b) TE waves.

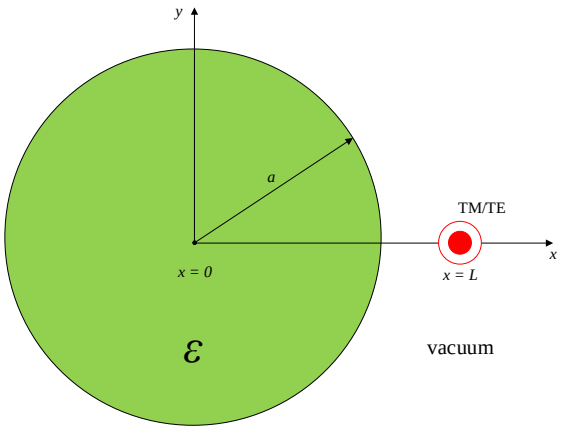

Figure 4.5: A solid cylinder of radius a, filled with a material of complex relative permittivity $\varepsilon = \text{Re}[\varepsilon] + \text{iIm}[\varepsilon]$, centered at the origin. The source is positioned at distance L from the cylinder's center.

In what follows, the performance of the structures will be evaluated using (3.39), by comparing the total enhancement of the radiated power for each feasible positioning of the source, for various combinations of materials and sizes of the cylindrical structure. It becomes evident that numerical convergence issues may now arise; specifically, we must select a sufficient number of terms n so as to achieve the desirable convergence. However, if the number of terms is too large, significant computational power may be needed. Therefore, n needs to be large enough to reach convergence, but not too large. Finding the optimal number of terms n requires testing, but a general rule one can follow is selecting n so that it is larger than the maximum optical size of the device used. In the case of the solid cylinder where $L > a$, the maximum optical size of each possible structure is $2\pi L/\lambda$. Therefore, if $a < L < L_{\max}$, one should select $n \geq \lceil 2\pi L_{\max}/\lambda \rceil$.

Unlike the PEC case, where only the size of the structure was of interest, apart

from the positioning of the source, now we have one extra variable to consider; the relative permittivity ε, and specifically its real part. To properly capture the performance of the geometry depicted in Fig. 4.5, we employ both plasmonic ($\mathrm{Re}[\varepsilon] < 0$, capacitive behavior) and dielectric ($\mathrm{Re}[\varepsilon] > 0$, inductive behavior) materials. The range of $\mathrm{Re}[\varepsilon]$ is selected so that it is large enough that allows for a detailed study of the performance while also being realistic for materials in the optical frequency range. Therefore, we choose to study cases in which $-10 \leq \mathrm{Re}[\varepsilon] \leq 10$. Additionally, the optical radius of the rod a/λ should not be too small, so that we can observe its influence, but not too large either ($a > \lambda$). Therefore, the range $0.2 < a/\lambda < 0.8$ is chosen. As far as the position L of the source is concerned, we should investigate cases where it effectively interferes with the cylinder; therefore, we set $1 < L/a < 3$.

In Fig. 4.6, we present the metric $\rho = \max_L\{P_{\mathrm{rad}}/P_{\mathrm{inc}}\}$ (in decibels), on the ($\mathrm{Re}[\varepsilon]$, a/λ) map, in the case of a line source placed at distance L from the center of a solid cylinder of radius a and complex permittivity $\varepsilon = \mathrm{Re}[\varepsilon] - 0.03\mathrm{i}$, for both polarizations separately. Specifically, in Fig. 4.6(a), where TM waves are studied, we notice improved performance, compared with the corresponding PEC case from Fig. 4.4(a). Indeed, $\rho > 2$ scores occur on the whole parametric plane while sharp peaks with $\rho \cong 10$ appear along hyperbolic parametric paths in dielectric cases. Moreover, in Fig. 4.6(b), where the TE-excited setups are depicted, one observes a significant improvement in performance when plasmonic ($\mathrm{Re}[\varepsilon] < 0$) designs are considered, while the behavior is similar to the TM case in dielectric ($\mathrm{Re}[\varepsilon] > 0$) setups. Therefore, we notice that plasmonic TE configurations exploit the constructive interaction of images better than Fig. 4.4(b). It is evident that the radiation enhancement ρ in the presence of a solid cylinder is not very large. Therefore, other structural alternatives should be investigated.

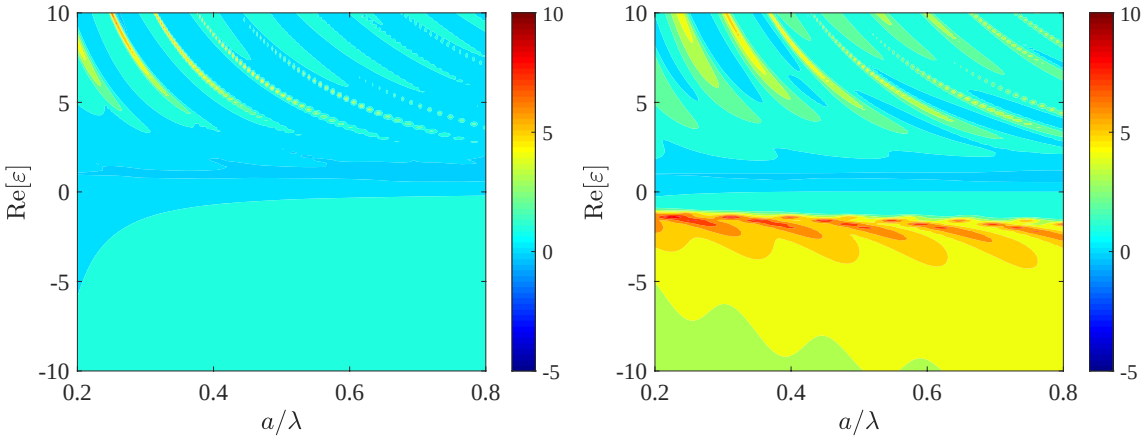

Figure 4.6: The metric ρ from (3.39) (in decibels), with $L > a$, represented with respect to the optical size a/λ of a solid cylinder and the real part of its relative permittivity $\mathrm{Re}[\varepsilon]$, in the case of: (a) TM polarization, (b) TE polarization. Small constant losses are assumed: $\mathrm{Im}[\varepsilon] = -0.03$.

Chapter 5

Hollow Radiators

Moving the search for the optimal radiators forward, we will now consider structures where the source is essentially embraced by the cylindrical structure. In this way, the modes developed within the resulting cavity can constructively interfere, leading to substantial radiation enhancement.

Towards this goal, we employ the structure presented in Fig. 5.1, where a hollow cylinder of internal radius g and external radius a is used. The shell is filled with a material of complex relative permittivity ε, whose imaginary part will once again be constant ($\mathrm{Im}[\varepsilon] = -0.03$) and equal to the value employed in the previous design (solid rod) for the reasons discussed in the previous chapter and in order to have a fair comparison between the solid rods and hollow cylinders. The source is placed within the cavity ($0 \leq L < g$), for the reasons described in the previous paragraph.

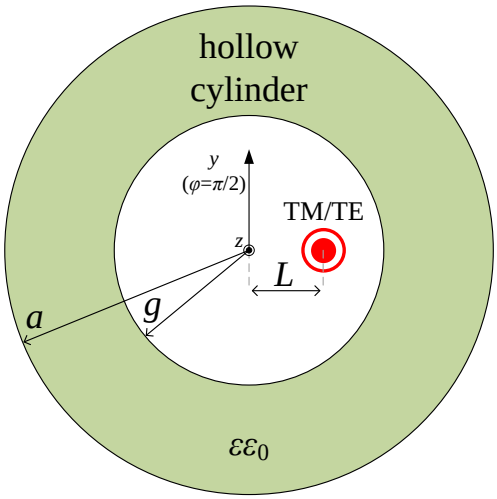

Figure 5.1: A hollow cylinder of internal radius g and external radius a, whose shell is filled with a material with complex relative permittivity ε. The source is placed inside the cavity ($0 \leq L < g$).

5.1 Maximal Radiation Maps

Compared to the previous chapter, we now have one extra variable to consider in the optimization scheme; the internal radius g of the hollow cylinder. Therefore,

our metric ρ needs to be modified. Specifically, ρ is now further maximized with respect to g; thus, we introduce a new metric:

$$\rho_{\max} = \max_{0<g/a<1} \{\rho\}. \tag{5.1}$$

In Fig. 5.2, we present the results for the hollow cylinder, for both TM and TE waves, on the (Re[ε], a/λ) map. As a product of a double optimization (with respect to both L/g and g/a), the processing power required to produce the final results is now increased. However, convergence is now achieved with significantly less terms, since our devices are smaller, having a total optical length of $2\pi a/\lambda \leq 1.6\pi$.

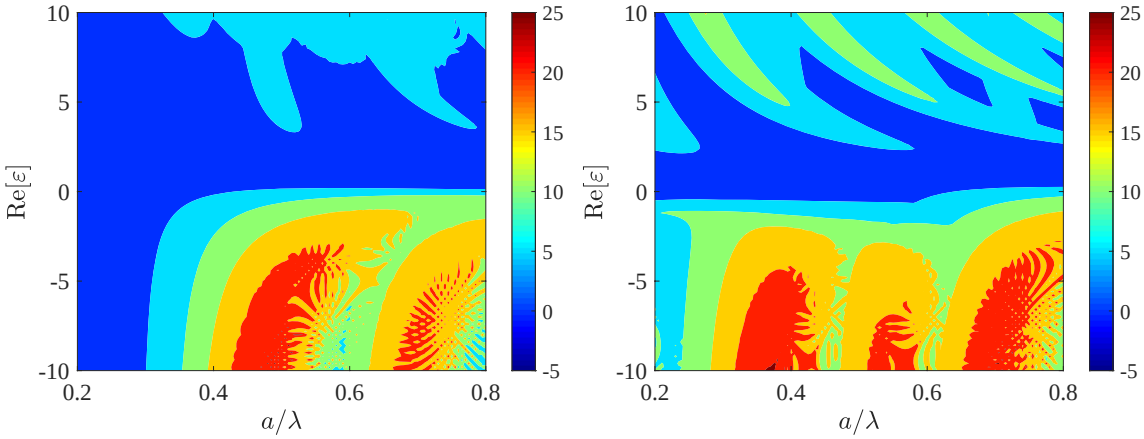

Figure 5.2: Results for a hollow cylinder of internal radius g and external radius a. The metric $\rho_{\max}$ (ρ further maximized with respect to g), in decibels, represented across the (a/λ, Re[ε]) map, in the case of: (a) TM waves, (b) TE waves. In both cases the source is placed internally to the hollow cylinder ($0 \leq L < g$).

In Fig. 5.2(a), we show the corresponding results in the case of a TM-polarized line source. We notice a huge enhancement compared to the previous cases (up to 25dB), which is achieved in two specific parametric regions corresponding to plasmonic (Re[ε] < 0) designs. In these cases specifically, a pair of evanescent modes is developed within the shell, which activate it more efficiently than the oscillating modes observed in dielectric cases [3]. Indeed, while the magnitude of the fields in the latter scenario is bounded by twice the magnitude of a single wave, exponentially varying fields can obtain much larger values and significantly boost emission. In Fig. 5.2(b), where TE waves are concerned, one observes 3 plasmonic hotspots (instead of 2) that correspond to significant radiation enhancement. In fact, these parametric regions are larger in size and correspond to a greater $\rho_{\max}$ compared to the ones in Fig. 5.2(a). Remarkably, the hyperbolic parametric regions first observed for dielectric cases in 4.6 are present in this case as well, appearing at similar a/λ.

5.2 Distribution of High Performers

At this point, it would be meaningful to investigate the influence of the two implicit optimization parameters (L/g, g/a) on the performance of our devices. Specifically,

we would like to observe at which L and g the highest enhancement occurs.

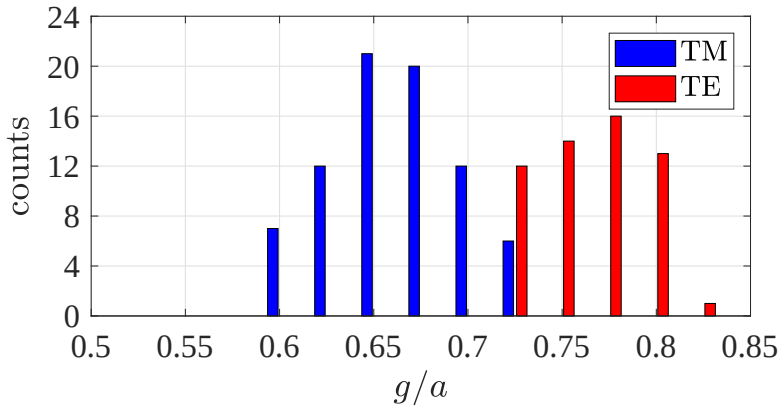

(a)

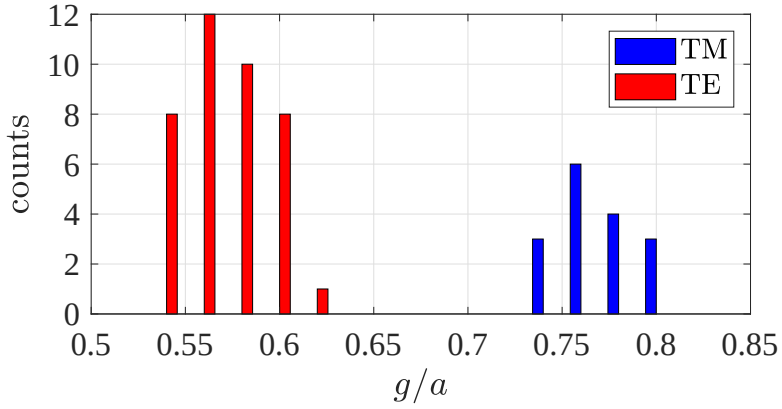

(b)

Figure 5.3: The number of successful ($\rho_{\max} > 24$ dB) superradiating designs, from Fig. 5.2, as a function of the internal radius g of the hollow cylinder over its external one a, for both polarizations. (a) Centered excitation ($L = 0$), (b) Off-centered excitation ($L \cong g/2$ for TM waves, $L \cong g$ for TE).

Suprisingly, a substantial number of our most promising ($\rho_{\max} > 24$ dB) designs occur when $L = 0$. Therefore, in Fig. 5.3(a), we have selected all of these designs and have calculated their frequency of appearance in various g/a. It is important to note that the points corresponding to TM waves are obtained from the left plasmonic cluster of Fig. 5.2(a) ($0.45 < a/\lambda < 0.55$), while the ones corresponding to TE polarization require much larger optical radii a/λ ($0.65 < a/\lambda < 0.75$). This is to be expected, since TE electric fields interact with the transverse size $2a$ of the structures which should not be too small; in contrast, TM electric fields oscillate along the infinite z direction and do not require larger a/λ. Additionally, we notice that TM-excited, centrally-fed setups need thicker shells to operate, while TE ones require thinner shells.

Apart from the centrally-fed ($L = 0$) high performers, there are also cases where significant enhancement is developed with asymmetrical excitation. The frequency of these designs is shown in Fig. 5.3(b). Remarkably, high performance is reached when $L \cong g/2$ for TM-excited configurations and when $L \cong g$ for TE-excited ones. In this case, TE designs require moderately-size cylinders ($0.3 < a/\lambda < 0.45$), which

in turn leads to thicker shells. Furthermore, the source is placed very close to the interface; this is to be expected, since this positioning enables it to constructively interfere with the developed images into the plasmonic shell, resulting in substantial emission enhancement. On the other hand, TM-illuminated setups now require larger optical radii ($0.65 < a/\lambda < 0.75$) and the source is positioned so that all the developed images into the thin shell contribute to the field enhancement.

5.3 Higher Losses and External Illumination

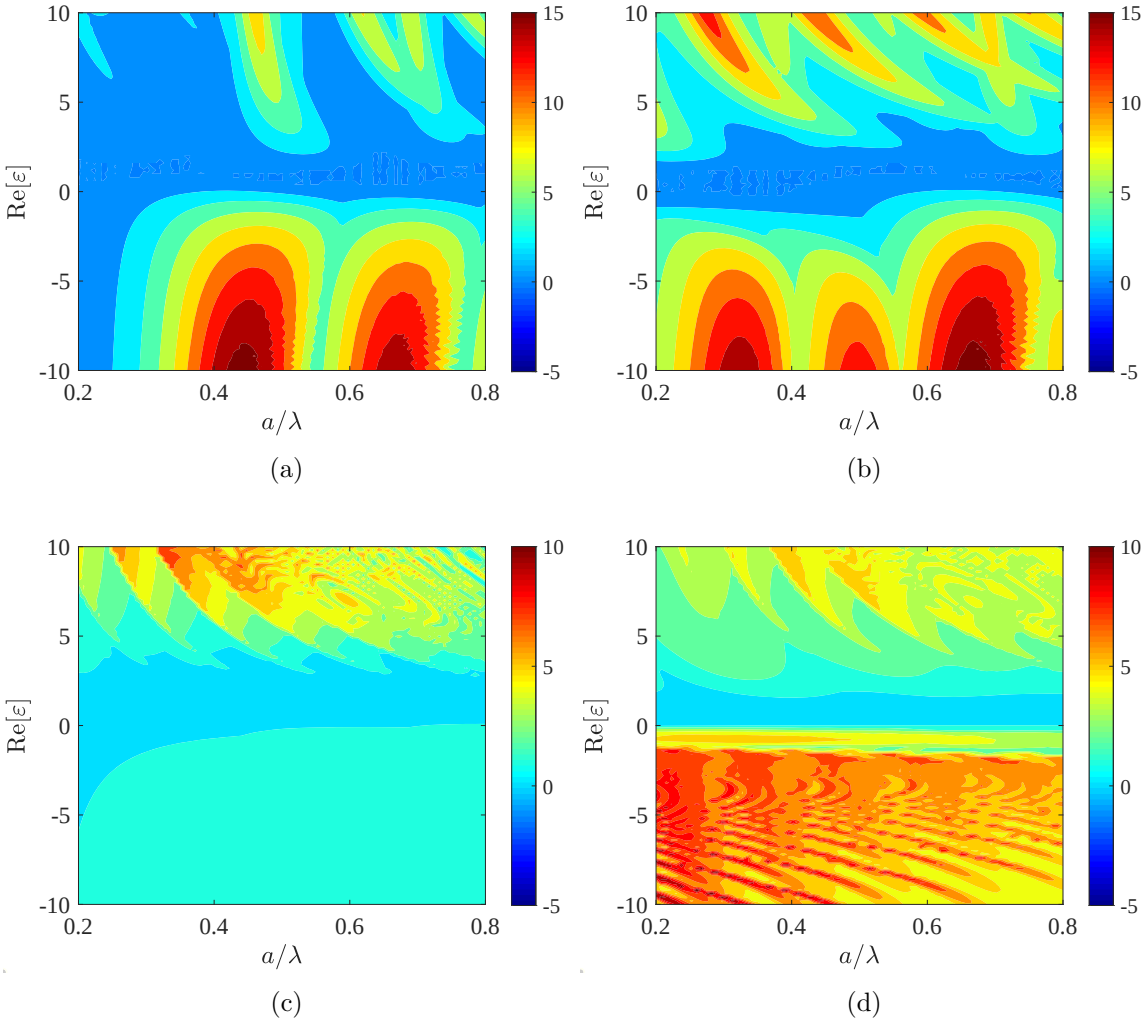

Figure 5.4: The metric $\rho_{\max}$ (ρ further maximized with respect to g), in decibels, represented across the (a/λ, Re[ε]) map for: (a) moderate losses (Im[ε] $= -0.3$) in TM waves, (b) moderate losses (Im[ε] $= -0.3$) in TE waves, (c) external illumination ($L > a$) under TM waves, (d) external illumination ($L > a$) under TE waves.

Up to this point, we have studied the performance of cylindrical radiators with low losses (Im[ε] $= -0.03$). Therefore, it would be interesting to see the effects of higher dissipation in the performance of the hollow cylinders. To this end, in Fig. 5.4(a), we have repeated the calculations of Fig. 5.2(a), however this time we have considered losses that are ten times higher (Im[ε] $= -0.3$). We notice that

substantial enhancement ($\rho_{\max} \cong 15$ dB) can be achieved; nevertheless, performance is significantly lower than the low-loss counterpart of Fig. 5.2(a). Similar conclusions can be drawn from Fig. 5.4(b), where the TE case is considered. It is important to note that the high-scoring plasmonic parametric regions of Figs. 5.2(a) and 5.2(b) remain unaltered, a feature that demonstrates the robustness of our designs in the presence of Ohmic effects. Additionally, the hyperbolic paths noticed in dielectric designs retain their values for the performance metric $\rho_{\max}$, despite the increased losses.

In Fig. 5.4(c), we switch back to low losses ($\mathrm{Im}[\varepsilon] = -0.03$), but this time we calculate $\rho_{\max}$ in the case of external ($L > a$) TM illumination. Remarkably, one observes that the resulting maximization map is very similar to Fig. 4.6(a), where the TM-excited solid rod was considered; as a result, we conclude that the modulation of the inner radius g does not significantly alter the performance of externally-excited TM setups. On the other hand, in Fig. 5.4(d), where the TE case is considered, we notice the presence of many bright spots in plasmonic ($\mathrm{Re}[\varepsilon] < 0$) designs, corresponding to higher scores than the ones in Fig. 5.2(b).

In any case the performance of both the high-loss and externally excited setups is significantly lower than the corresponding low-loss, internally excited cases for the both polarizations (TM/TE).

Chapter 6

Radiating Nanotubes

We have previously observed that positioning the source internally to cylindrical boundaries can lead to substantial enhancement of the outgoing radiation. For this reason, our next proposed structure will be comprised of two concentric metasurfaces of radii $r = g$ and $r = a$ respectively, with identical complex conductivity σ while the source will be positioned in the domain in-between the two nanotubes ($g < L < a$), as shown in Fig. 6.1.

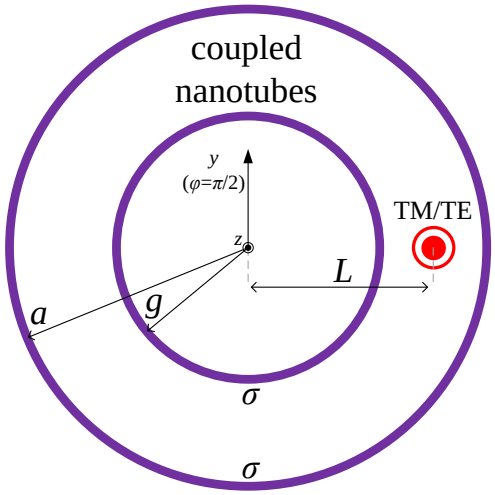

Figure 6.1: A pair of concentric nanotubes of radii g and a respectively, having identical surface conductivity σ. The source is positioned between the two metasurfaces ($g < L < a$).

Such positioning of the source serves an important purpose. Specifically, it is ideally placed in a resonant cavity created by the two metasurfaces, where it can mutually interract with both of them. As a result, the constructive interference between the azimuthal harmonics developed therein leads to the greatest enhancements observed in this work. In the following sections, it will become evident that the coupled nanotubes geometry offers the best performance out of all the studied radiators.

6.1 The Case of the Single Nanotube

Before moving on to the study of the coupled nanotubes, it would be interesting to study the behavior of a simpler structure, that employs only on metasurface of radius a, with the source positioned inside $0 < L < a$. Additionally, it is important to note that in these cases, the solution is derived using the boundary condition for the discontinuity of the φ and z components of the magnetic field $\mathbf{H}$, due to the presence of a surface current $\mathbf{J}_s = -\sigma\hat{\boldsymbol{r}} \times (\hat{\boldsymbol{r}} \times \mathbf{E})$, induced by the tangential electric field.

Furthermore, in order to have a fair comparison with the previously studied setups, the losses ($\mathrm{Re}[\sigma]$) are chosen using the following formula connecting the conductivity and permittivity for very thin dielectric slabs [4]:

$$\sigma\eta_0 = 2\pi \mathrm{i}\frac{d}{\lambda}(\varepsilon - 1), \tag{6.1}$$

where η_0 is the impedance of vacuum and d the thickness of the slab. Using $d = 0.1\lambda$ and the losses employed previously ($\mathrm{Im}[\varepsilon] = -0.03$), we obtain $\mathrm{Re}[\sigma\eta_0] \cong 0.019$. As far as the imaginary part is concerned, this is picked so as to correspond to the response of realistic materials illuminated by visible radiation [4].

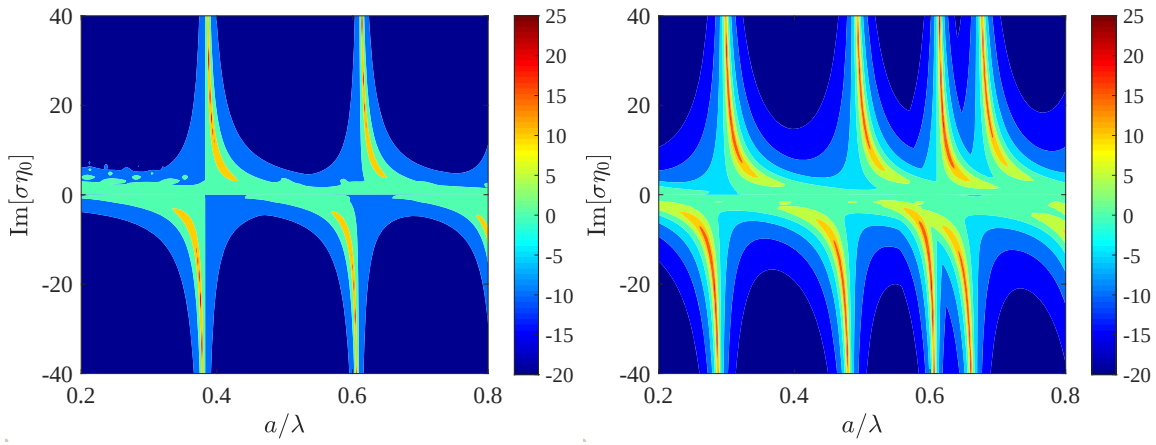

Figure 6.2: Results for a single nanotube of radius a and complex surface conductivity σ. The metric ρ (in decibels) depicted on the (a/λ, $\mathrm{Im}[\sigma\eta_0]$) plane, in the case of: (a) TM polarization, (b) TE polarization. Small constant losses are assumed: $\mathrm{Re}[\sigma\eta_0] \cong 0.019$.

In Fig. 6.2, we present the results for the case of the internally-excited single nanotube. We notice that despite its simplicity, the structure can significantly boost radiation, delivering significantly better results than a solid cylinder. In both Fig. 6.2(a) and 6.2(b) (regarding TM and TE waves respectively), we notice the presence of quasi-periodic strips corresponding to highly-performing designs, for both dielectric ($\mathrm{Im}[\sigma\eta_0] > 0$) and plasmonic ($\mathrm{Im}[\sigma\eta_0] < 0$) materials. Outside of these periodic domains, there are parametric regions where both TM and TE emitters are practically blocked. This effect is less intense in TE-excited setups, where higher scores can be achieved on average.

The nature of the highly-scoring parametric strips can be captured analytically in the case of centrally-fed ($L = 0$) setups, which are commonly the result of optimization, as observed in previous chapters. By maximizing the radiated power with respect to $\mathrm{Im}[\sigma\eta_0]$ and expanding for small a/λ we obtain:

$$\mathrm{Im}[\sigma\eta_0] = \begin{cases} -\frac{2Y_0(k_0a)/\pi}{k_0aJ_0(k_0a)|H_0(k_0a)|^2} & \text{, TM waves} \\ -\frac{2Y_1(k_0a)/\pi}{k_0aJ_1(k_0a)|H_1(k_0a)|^2} & \text{, TE waves} \end{cases} . \tag{6.2}$$

6.2 The Case of the Coupled Nanotubes

We now move on to the most highly-performing cylindrical configuration studied in this thesis, the pair of coupled nanotubes. In Fig. 6.3, we depict the metric $\rho_{\max}$ (ρ further maximized with respect to g) on the ($\mathrm{Im}[\sigma\eta_0]$, a/λ) plane, assuming the same small constants losses used in the previous case. In this case however, the source is free to move within the resonant cavity created by the two cylindrical metasurfaces ($g < L < a$).

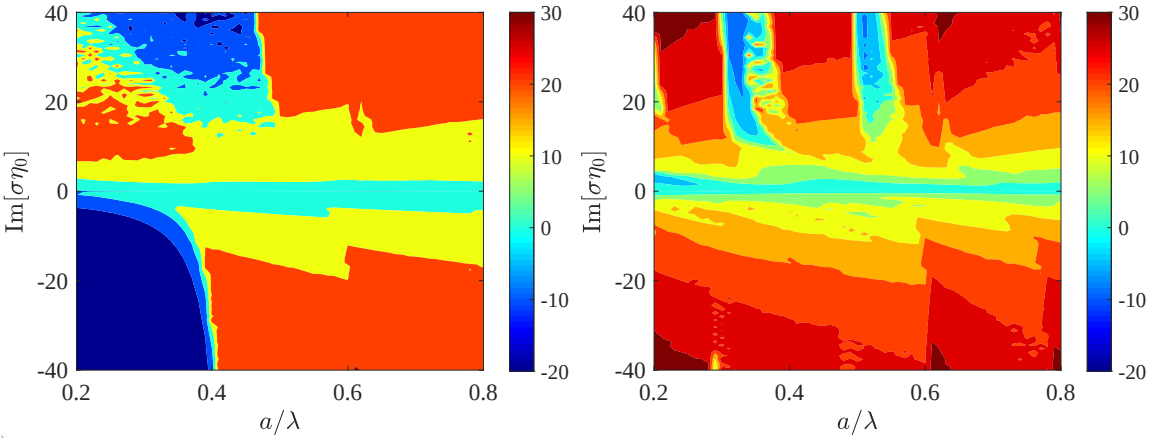

Figure 6.3: Results for concentric nanotubes of radii g, a and complex surface conductivity σ, with the source placed between them ($g < L < a$). The metric $\rho_{\max}$ (in decibels) depicted on the (a/λ, $\mathrm{Im}[\sigma\eta_0]$) plane, in the case of: (a) TM polarization, (b) TE polarization. Small constant losses are assumed: $\mathrm{Re}[\sigma\eta_0] \cong 0.019$.

In Fig. 6.3(a), where the TM-excited setups are studied, we notice significantly improved performance compared to Fig. 6.2(a). Specifically, the achieved scores are significantly higher while the parametric domains on which high performance is observed are more extensive. However, a significant blockage of outgoing radiation occurs for small ($a/\lambda < 0.4$), plasmonic ($\mathrm{Im}[\sigma\eta_0] < 0$) designs. In order to approximately capture the nature of this effect, we consider a centrally-fed system with $g = a/2$. The condition for maximal radiation, assuming thin tubes ($a/\lambda << 1$), now reads:

$$\mathrm{Im}[\sigma\eta_0] \cong \frac{A_1\ln(k_0a) - A_0}{k_0a\left[B_2\ln^2(k_0a) - B_1\ln(k_0a) - B_0\right]}, \tag{6.3}$$

where A_0, A_1, B_0, B_1, B_2 are positive constants, not shown here for brevity. This formula nullifies at $\ln(k_0 a) = A_0/A_1 \cong \ln(0.45\pi)$ and exhibits a singularity at $\ln(k_0 a) = \left(B_1 + \sqrt{B_1^2 + 4B_0 B_2}\right)/(2B_2) \cong \ln(1.04\pi)$ while $\mathrm{Im}[\sigma\eta_0]$ remains negative between these two points.

In Fig. 6.3(b), we depict the results corresponding to TE excitation. It is evident that the most substantial performance is recorded, greater than all other competing setups. In particular, the radiated power is up to 3 orders of magnitude higher than the power of a free-standing source, for several textural and structural combinations. Additionally, no blockage effect can be observed, contrary to the suffocation of the source in the cases of Fig. 6.2(a), 6.2(b) and 6.3(a). As far as the most successful superradiating paired nanotube configurations are concerned, they can be either dieletric or plasmonic, appearing around two specific optical radii, namely at $a \cong 0.21\lambda$ and $a \cong 0.62\lambda$.

6.3 Selected Optimal Designs

Up to now mainly optimizations are executed as indicated in (3.39) and the definition of $\rho_{\max}$; tight parametric sweeps have been performed with respect to the structural and textural characteristics for each of the considered setups. Therefore, it would be interesting to examine specific designs that deliver huge radiation enhancement and identify the influence of geometrical, material and source features on their operation. By inspection of Fig. 6.3, we pick highly performing superradiating setups corresponding to $a \cong 0.62\lambda$, since that optical size gives significant $\rho_{\max}$ for both polarizations in coupled concentric nanotubes. As far as the surface conductivity is concerned, we avoid extreme values and select dielectric or plasmonic nanotubes with $\mathrm{Im}[\sigma\eta_0] = \pm 20$ that correspond to the mean of the respective ranges of Fig. 6.3 for each type of material.

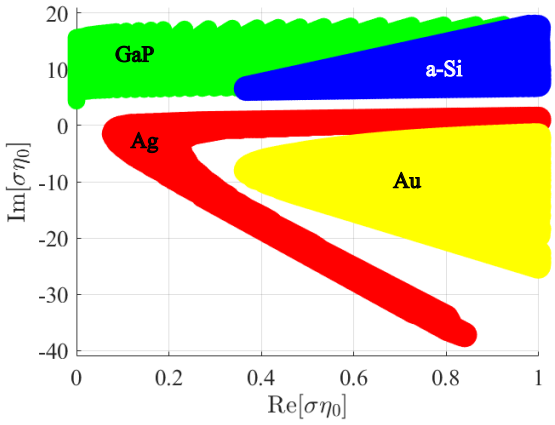

Figure 6.4: The response of various materials in the visible frequency range (300 nm $< \lambda <$ 500 nm), according to (6.1). We consider the homogenized behavior, dictated by (6.1), for media filling a thin slab of thickness $d = 55$ nm.

It would be meaningful to describe the kinds of materials that can have this specific response at optical frequencies. The simplest case would be to use a homogeneous flake layer of a dielectric or plasmonic medium. The resulting surface

conductivity will be given by (6.1). In Fig. 6.4, we represent the complex conductivities obtainable in various media, excited by sources in the visible spectrum (300 nm $< \lambda <$ 500 nm). We notice that gallium phosphide layers can mimic metasurfaces with conductivities having high positive imaginary part and minuscule real part. Silver on the other hand can exhibit a similar behavior, while retaining its metallic nature. Furthermore, in the cases of designs that can tolerate high losses, amorphous silicon layers may be used for dielectric setups, while golden slabs are suitable for plasmonic ones.

Alternatively, similar characteristics for the conductivity may be achiebed by patterning surfaces with various nanostructures and operating them under resonant regimes. More specifically, one ca use hafnium oxide nanoposts fabricated using atomic layer deposition [68] or discretized metatoms optimally coupled to work under visible light with suppressed losses [69]. Furthermore, silicon metasurfaces comprising nanoblocks constructed at a single lithographical step can reach high efficiency in optical frequencies [70] while monolithic MEMS reflectarrays can achieve extremely low-losses in the microwave regime [71].

In Fig. 6.5, we represent the radiation enhancement $P_{\text{rad}}/P_{\text{inc}}$ across the implicit optimization map for each of the four selected designs ($a \cong 0.62\lambda$, $\text{Im}[\sigma\eta_0] = \pm 20$, TM waves, TE waves). The horizontal axis indicates how far from the internal nanotube the source is placed g/L and the vertical axis shows the respective relative distance L/a from the external one. It is important to note that the these ratios of distances g/L, L/a take values strictly between 0 and 1 and each combination of them corresponds to source placements between the cylindrical metasurfaces. Additionally, one observes that the peak performing configurations lie along hyperbolic parametric strips. Such a feature offers extra degrees of freedom in the photonic design process of superradiating nanotubes. In Fig. 6.5(a) and Fig. 6.5(b), we notice that the optimal setups have almost the same L/a; this is not the case if TE waves (Figs. 6.5(c), 6.5(d)) are considered, where the relative position of the source with the external boundary changes dramatically in proportion to the nature (dielectric/plasmonic) of the employed medium. Indeed, the TM-excited setups prefer to leave larger gaps between the source and the two boundaries; on the contrary, the optimal source placements under TE illumination are very close to the nanotubes. Specifically, the emitter is positioned close to the external nanotube in the optimized structure of Fig. 6.5(c) and near the internal one in that of Fig. 6.5(d). That happens because dipoles in the vicinity of dense media (either dielectric or plasmonic) enhance the radiated power once they are normal to the interface.

6.4 Images of a Line Source above a Metasurface

In order to interpret the behavior of the source between the two boundaries in the optimal designs, we employ image theory once again. In the case where the source is placed in the vicinity of a cylindrical boundary, it senses it as an infinite plane; for this reason, we will study the behavior of a line source placed at distance d above an infinite metasurface of complex surface conductivity σ, as shown in Fig. 6.6.

The incident field, utilizing the integral representation of the $H_0^{(2)}(k_0 r)$ function,

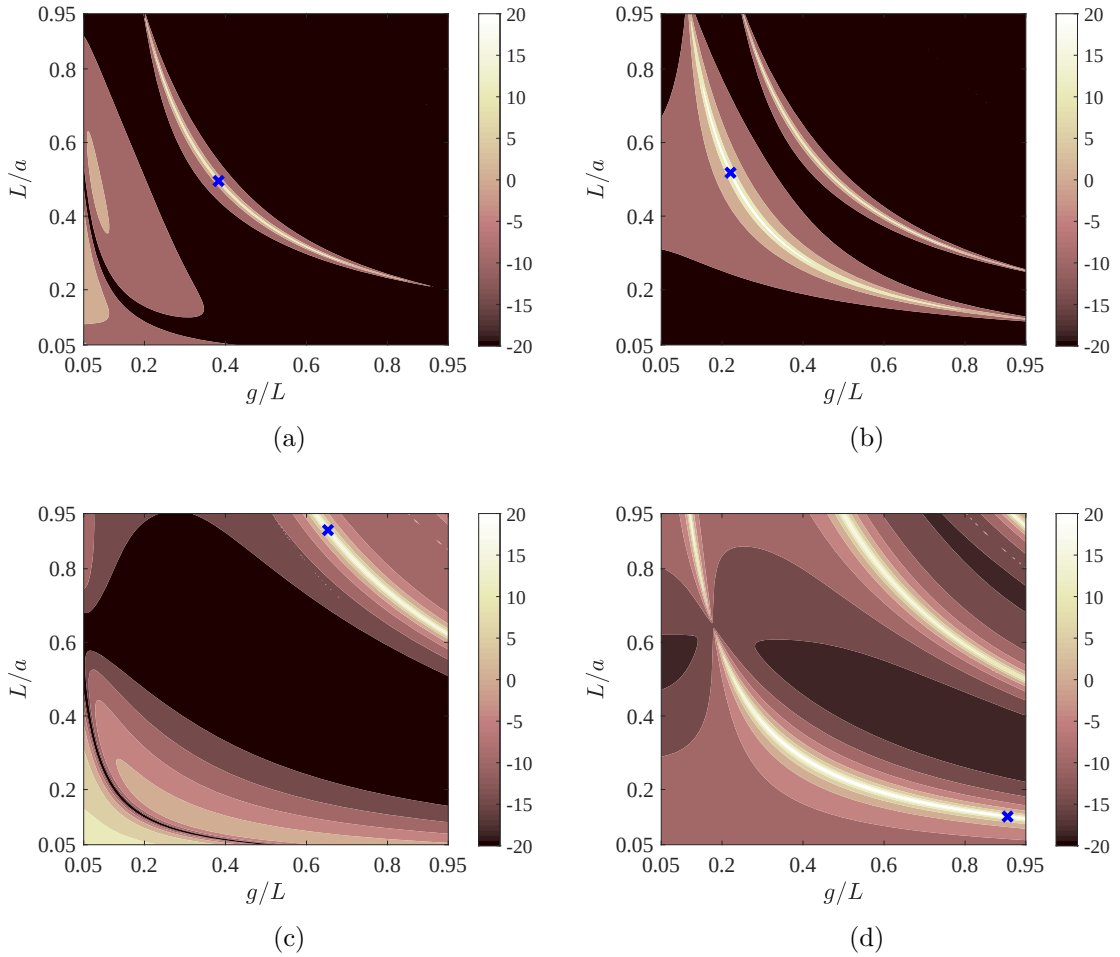

Figure 6.5: Relative radiating power $P_{\text{rad}}/P_{\text{inc}}$ (in decibels) depicted on the implicit optimization plane $(g/L, L/a)$ for $a/\lambda = 0.62$. (a) $\text{Im}[\sigma\eta_0] = 20$ (dielectric), under TM waves, (b) $\text{Im}[\sigma\eta_0] = -20$ (plasmonic), under TM waves (c) $\text{Im}[\sigma\eta_0] = 20$ (dielectric), under TE waves, (d) $\text{Im}[\sigma\eta_0] = -20$ (plasmonic), under TE waves. The blue crosses mark the selected optimal designs.

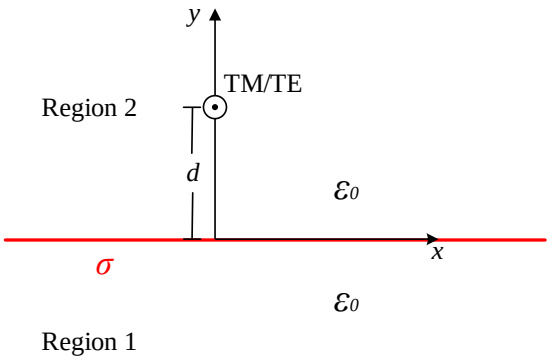

Figure 6.6: A line source of either TM or TE polarization, positioned at distance d above an infinite metasurface of complex surface conductivity σ.

is given by $\mathbf{F}_{\text{inc}}^{\text{TM/TE}} = F_{\text{inc}}^{\text{TM/TE}}\hat{\boldsymbol{z}}$, where:

$$F_{\text{inc}}^{\text{TM}} = -\frac{\mathrm{i}k_0\eta_0 I}{4\pi}\int_{-\infty}^{+\infty}\frac{e^{-|y-d|\kappa(\beta)}e^{-\mathrm{i}\beta x}}{\kappa(\beta)}\mathrm{d}\beta, \tag{6.4}$$

$$F_{\text{inc}}^{\text{TE}} = -\frac{\mathrm{i}k_0 V}{4\pi\eta_0}\int_{-\infty}^{+\infty}\frac{e^{-|y-d|\kappa(\beta)}e^{-\mathrm{i}\beta x}}{\kappa(\beta)}\mathrm{d}\beta, \tag{6.5}$$

where I is an electric current (in A), V is a magnetic current (in V) and $\kappa(\beta) = (\beta^2 - k_0^2)^{1/2}$.

In this scenario, the reflected and transmitted waves can be described using effective image sources, as in the PEC case. Using our intuition, we expect that for the case of the transmitted wave in the lower half-space, an image source should be placed at $y = -d$. On the other hand, the reflected wave will be given by an effective image placed at $y = d$. Furthermore, we expect these to not behave as images in the traditional sense; as a result of the integration, their excitations will naturally be functions of the spectral variable β and to calculate their contribution we will have to calculate the corresponding improper integral. Therefore, the transmitted components will be given by:

$$F_{\text{t}}^{\text{TM}} = -\frac{\mathrm{i}k_0\eta_0}{4\pi}\int_{-\infty}^{+\infty} I'(\beta)\frac{e^{-|y-d|\kappa(\beta)}e^{-\mathrm{i}\beta x}}{\kappa(\beta)}\mathrm{d}\beta, \tag{6.6}$$

$$F_{\text{t}}^{\text{TE}} = -\frac{\mathrm{i}k_0}{4\pi\eta_0}\int_{-\infty}^{+\infty} V'(\beta)\frac{e^{-|y-d|\kappa(\beta)}e^{-\mathrm{i}\beta x}}{\kappa(\beta)}\mathrm{d}\beta, \tag{6.7}$$

while the reflected ones are obtained from:

$$F_{\text{r}}^{\text{TM}} = -\frac{\mathrm{i}k_0\eta_0}{4\pi}\int_{-\infty}^{+\infty} I''(\beta)\frac{e^{-|y+d|\kappa(\beta)}e^{-\mathrm{i}\beta x}}{\kappa(\beta)}\mathrm{d}\beta, \tag{6.8}$$

$$F_{\text{r}}^{\text{TE}} = -\frac{\mathrm{i}k_0}{4\pi\eta_0}\int_{-\infty}^{+\infty} V''(\beta)\frac{e^{-|y+d|\kappa(\beta)}e^{-\mathrm{i}\beta x}}{\kappa(\beta)}\mathrm{d}\beta. \tag{6.9}$$

Enforcing the boundary conditions for the continuity of the tangential component of the electric field and the discontinuity of the tangential component of the magnetic field, we arrive at the following expressions for the TM images:

$$I'(\beta) = \frac{2\kappa(\beta)}{2\kappa(\beta) + \mathrm{i}k_0\sigma\eta_0} I, \tag{6.10a}$$

$$I''(\beta) = \frac{-\mathrm{i}k_0\sigma\eta_0}{2\kappa(\beta) + \mathrm{i}k_0\sigma\eta_0} I, \tag{6.10b}$$

while for the TE ones:

$$V'(\beta) = \frac{2k_0}{2k_0 - \mathrm{i}\sigma\eta_0\kappa(\beta)} V, \tag{6.11a}$$

$$V''(\beta) = \frac{-\mathrm{i}\sigma\eta_0\kappa(\beta)}{2k_0 - \mathrm{i}\sigma\eta_0\kappa(\beta)} V. \tag{6.11b}$$

Observing these equations, we notice that when $\sigma \to \infty$ (PEC case), we arrive at the expression for the image currents of the PEC case, previously studied in this thesis. Therefore, it is safe to assume that in the vicinity of dense media, image theory holds and the conclusions made in the previous section are valid.

6.5 Wavelength Dispersion and Spatial Variation

At this point, it would be interesting to study the performance characterictics of the selected optimal setups. Specifically, we would like to study their behavior under excitations of varying wavelength as well as the spatial distribution of the radiated far-field.

In Fig. 6.7, we present the relative emitted power $P_{\text{rad}}/P_{\text{inc}}$ (in dB) as a function of the normalized wavelength λ/λ_0, where λ_0 is the optimal operation point, for the four selected designs from Fig. 6.5. Additionally, in each of the aforementioned scenarios, we investigate the effects of significant losses ($\text{Re}[\sigma\eta_0] \cong 2.8$) and the response of the systems when subjected to the opposite polarization. One readily observes a sharp resonance at $\lambda = \lambda_0$ for all cases in which the nanotubes are illuminated by waves of the favorable polarization; naturally, when losses are introduced this effect is significantly diminished. However, in Fig. 6.7(c), where the dielectric, TE-excited setup is considered, a noticeably less sharp response can be observed. However, in Fig. 6.7(c), where the dielectric, TE-excited setup is considered, a noticeably less sharp response can be observed. Furthermore, it is evident that non-optimally polarized radiation is essentially blocked by dielectric designs operating around $\lambda = \lambda_0$ (Figs. 6.7(a), 6.7(c)); such a feature may be critical when designing polarization sensors. On the contrary, plasmonic ones (Figs. 6.7(b), 6.7(d)) are less polarization-sensitive and can boost both TM and TE radiation, even though they are optimized for only one type of waves. Finally, oscillations of the response occur owning to the periodic excitation which leads to the emergence of secondary peaks outside of the considered band, as revealed by Fig. 6.7(b).

In order to acquire more information regarding the operation of the optimized superradiating designs of Figs. 6.5, 6.7 it would be interesting to study the spatial distribution of emitted power around the respective structures. Therefore, we define the azimuthally-dependent power profile $p(\varphi)$ so that it is a dimensionless quantity, whose mean value gives the relative emitted power:

$$\frac{P_{\text{rad}}}{P_{\text{inc}}} = \frac{1}{2\pi}\int_0^{2\pi} p(\varphi)\mathrm{d}\varphi. \tag{6.12}$$

The analytical form of $p(\varphi)$ can easily be derived using the formulas developed in Chapter 3 of this thesis. More specifically, using (3.33) and (3.34), we obtain:

$$p(\varphi) = \left|\sum_{n=-\infty}^{+\infty} \mathrm{i}^n C_n e^{\mathrm{i}n\varphi}\right|^2. \tag{6.13}$$

In Fig. 6.8(a), we represent $p(\varphi)$ for each of the four variants of Fig. 6.7(a) in polar plots with respect to angle φ. Surprisingly, one observes that the radiation pattern corresponding to the optimized radiator of Fig. 6.7(a) is omnidirectional. This is attributed not to a central placement of the source ($L = 0$), since the presented emitter outperforms every single centrally-fed design of similar complexity. In fact, the interference of the developed waves between the two nanotubes effectively cancels out all the higher-order azimuthal harmonics ($e^{\mathrm{i}n\varphi}$, for $n \neq 0$) and boosts exclusively the isotropic one ($n = 0$). Moreover, the TE-excited radiation is negligible, which demonstrates the polarization sensitivity of our setup.

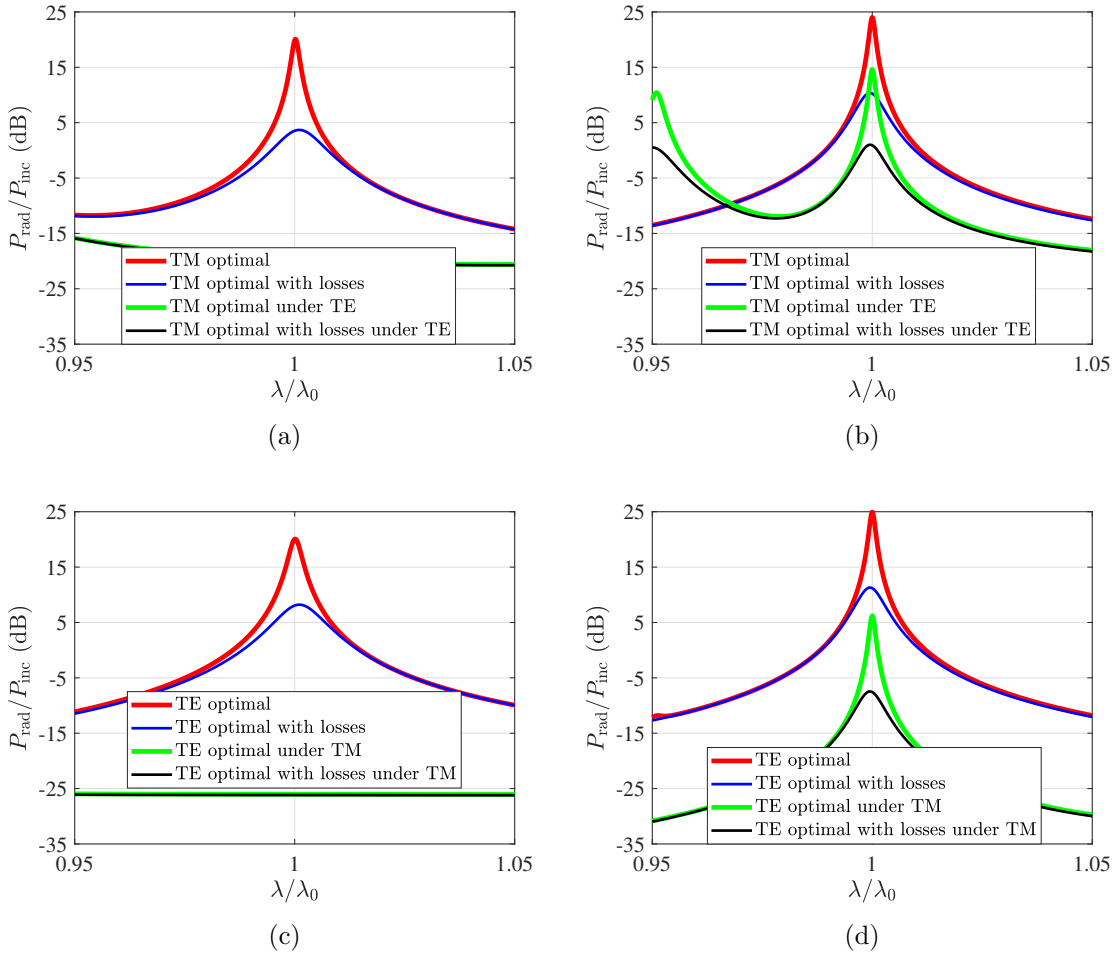

Figure 6.7: Relative radiated power $P_{\rm rad}/P_{\rm inc}$ (in decibels) as a function of the normalized wavelength λ/λ_0, around the optimal operation point $\lambda = \lambda_0$, for the designs selected from: (a) Fig. 6.5(a), (b) Fig. 6.5(b), (c) Fig. 6.5(c), (d) Fig. 6.5(d) and their lossy counterparts, when excited by both wave polarizations. The losses typically make the resonances less sharp.

In Fig. 6.8(b), where the emitter of Fig. 6.7(b) is examined, we realize that the optimal response is a dipolar one. Such a feature can be explained in a similar manner as the omnidirectional radiation of Fig. 6.8(a); indeed, all the other modes $e^{in\varphi}$ with $n \neq \pm 1$ are suppressed. Note that the bipolar radiation pattern is maximized along the horizontal x axis, since the source is positioned on it creating interference at this direction. Remarkably, the design reacts isotropically under TE illumination, leading to significant radiation enhancement which surpasses its TM counterpart in the vicinity of the vertical y axis. Such a behavior is counterintuitive, since a similar cancellation of modes (leaving only a strong $n = 0$ term) holds even for the type of waves with respect to which the design is not optimized.

In Fig. 6.8(c), we depict the radiation pattern corresponding to the setup of Fig. 6.7(c). Contrary to the previously examined designs, we notice that more than one and higher-order terms ($|n| \geq 2$) contribute to the far field emission, resulting in increased robustness in the presence of a perturbed excitation; that is why a less narrowband response is recorded in Fig. 6.7(c). As far as the TM waves are

considered, they are treated like the TE fields in Fig. 6.8(a), where the huge response contrast for different polarizations is once again exhibited. Where it comes to Fig. 6.8(d), we consider the remaining TE-optimized structure of Fig. 6.7(d) and we notice a powerful isotropic emission as that of Fig. 6.8(a). However, when fed with the other sort of waves (TM) an enhanced dipolar pattern emerges resembling the operational characteristics of the emitter of Fig. 6.8(b).

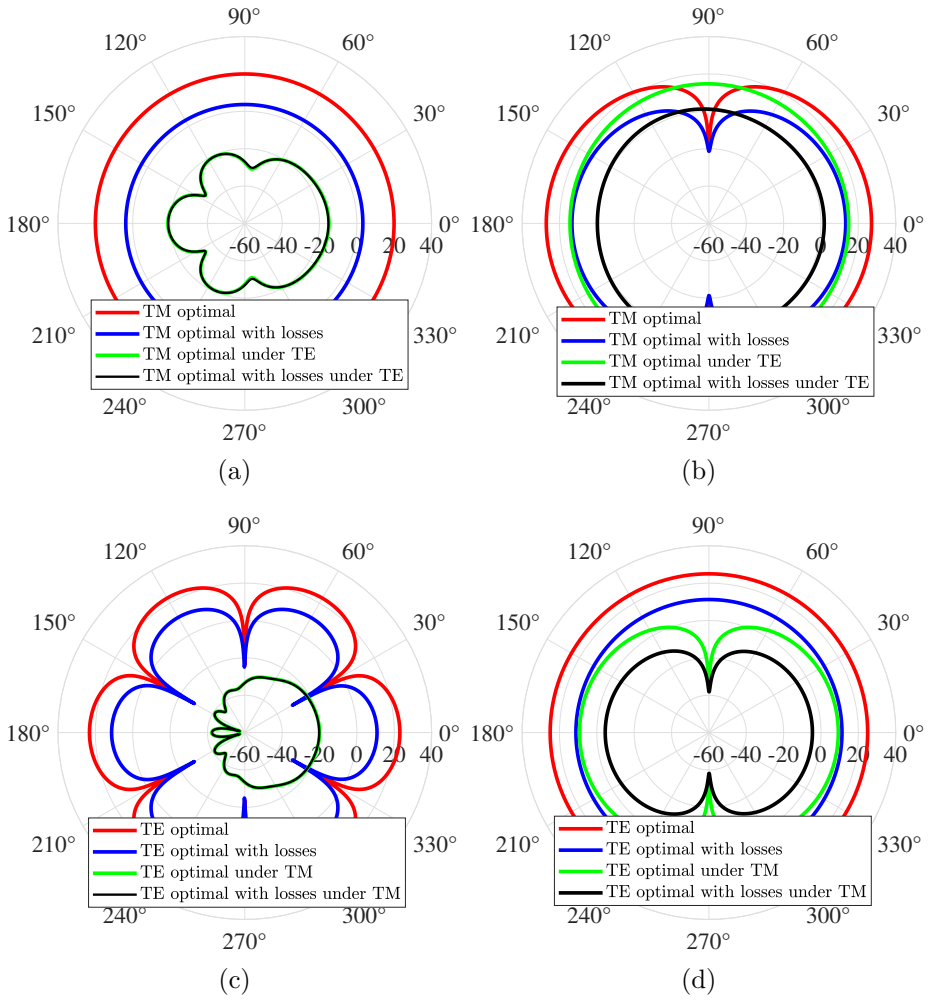

Figure 6.8: The power azimuthal profile $p(\varphi)$ from (6.13) (in decibels), presented on a polar plot with respect to angle φ for the designs selected from: (a) Fig. 6.5(a), (b) Fig. 6.5(b), (c) Fig. 6.5(c), (d) Fig. 6.5(d) and their lossy counterparts, when excited by both the wave polarizations. Strong omnidirectional, dipolar and multiharmonic azimuthal patterns are obtained.

6.6 Validation with Commercial Software

In order to strengthen the credibility of our theoretical findings, we perform numerical simulations to validate the far-field patterns presented above. To this end, we employ the COMSOL Multiphysics [5] commercial software.

In Fig. 6.9(a), we present the radiation pattern of the free-standing line source, simulated using the commercial software. It is evident that the total emitted power

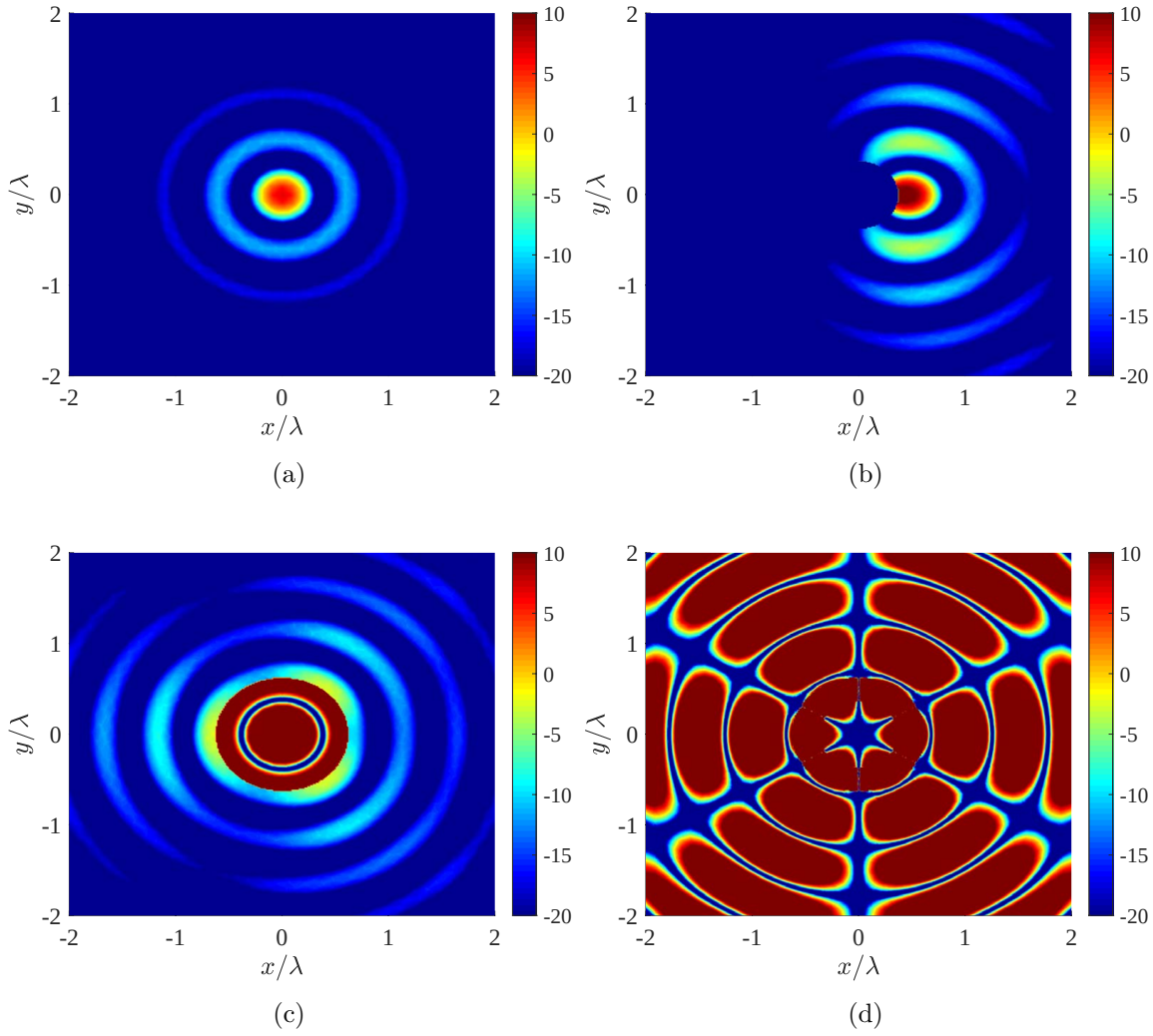

Figure 6.9: Results for a TE-excited, dielectric setup using a commercial software. The absolute value of the real part of the sole component of the magnetic field $|\mathrm{Re}[H_z(x,y)]|$, in dB, depicted across the xy plane, in the case of Fig. 6.5(c), when: (a) only the primary excitation dipole radiates, (b) only the internal nanotube is present, (c) only the external nanotube is present, (d) the optimal design is employed.

is indeed minuscule. This is also the case in Fig. 6.9(b), where we place the source in the optimal position of Fig. 6.5(c) but with only the internal boundary present. Since the dipole is positioned externally ($L > g$), we notice the poor penetration into the core combined with negligible radiation to the far-field. In Fig. 6.9(c), where only the external boundary is present, with the emitter positioned within the created cavity, we notice that the field is confined inside the cylinder and the penetration to the outside is poor. Finally, in Fig. 6.9(d), the exact setup of Fig. 6.5(c) is simulated. We notice a substantial radiation to the far-field, with a similar profile to that of Fig. 6.8(c). The average magnitude of the local signal is very close to the one indicated by the maximum of the red curve of Fig. 6.8(c) concerning the same design. In this way, we show how two nanotubes that cannot enhance the radiated power alone, can act collectively in an extremely successful manner that

multiplies the power of the source and validates the proposed concept.

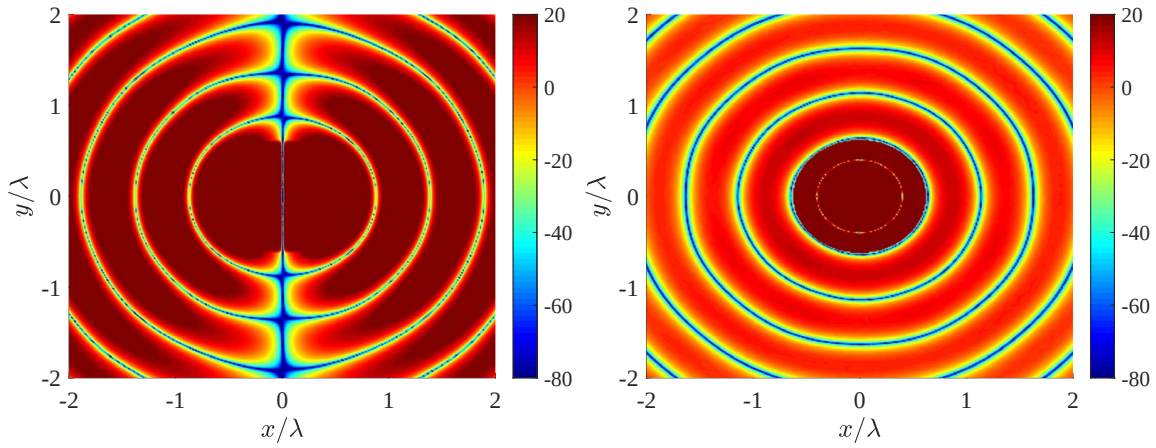

Figure 6.10: Results for the TM-optimized plasmonic setup of Fig. 6.5(b), using a commercial software, for: (a) TM excitation, represented quantity $|\mathrm{Re}[E_z(x,y)]|$ in dB, (b) TE excitation, represented quantity $|\mathrm{Re}[H_z(x,y)]|$ in dB.

It would also be interesting to investigate the response of a system that amplifies both polarizations concurrently. For this reason, we pick the TM- optimized, plasmonic design of Fig. 6.8(b) and simulate it under both TM and TE excitations. In Fig. 6.10(a), we present the simulation results for TM polarization ($|\mathrm{Re}[E_z(x,y)]|$ in dB). We notice a powerful bipolar pattern, thus validating the theoretical result of Fig. 6.8(b). Furthermore, the simulation of the TE-excited, TM-optimized plasmonic setup shown in Fig. 6.10(b), reveals a strong omnidirectional pattern, also present in Fig. 6.8(b) for the same case. As a result, our conclusions based on analytical computations of the signal in the far-field have been verified by an independent commercial software, revealing the validity of our approach.

Chapter 7

Conclusion

Extensive quests towards structural and textural combinations of simple cylindrical setups have been performed; they result in significant enhancement of the power radiated from a line source, under both polarizations. Such a choice for the excitation results in the problems being analytically solvable while also providing important physical intuition which may be lost when more complex, 3D excitations are considered. Once the line source is positioned inside plasmonic shells or between a pair of concentric nanotubes, electromagnetic superradiation is detected for several designs. In these cases, the mutual interference of the emitter with the surrounding boundaries can give an emission improvement of up to three orders of magnitude, compared to the radiation of the free-standing antenna. The performance of the most promising of these configurations exhibit sharp resonances, particularly befitted to ultra-sensitive filters. Furthermore, the spatial distribution of the power emitted from the aforementioned cylinders reveals strong omnidirectional or bipolar patterns different for each wave type (TM/TE); such a feature can be utilized towards polarization encoding for analog information processing. The radiation characteristics of the proposed designs have been validated using finite element simulations with the COMSOL Multiphysics [5] commercial software. Furthermore, our plasmonic structures have several benefits over previously proposed plasmonic nanoantennas. More specifically, our designs can enhance both polarizations concurrently, unlike traditional narrow-gap bowtie and dimer antennas while enhancing radiation to levels comparable to or even higher than the widespread plasmonic nanoantennas. Moreover, the superradiating setups are less bulky and hence easier to fabricate while also being less sensitive to nonlocal effects.

In addition to the above mentioned properties, the present work may be extended to inherit similar setups with desirable features that offer even more fascinating capabilities. In particular, adding nonlinearities to our cylindrical metasurfaces may assist in modeling memory elements with suppressed vulnerability to noise [6]. Moreover, one can regard a superradiating finite or infinite grating [7] from the proposed cylindrical structures operating collectively with each other; progressive changes in the phase of the current that feeds each element can result in complex wavefronts since the response from each emitter interferes in a different manner for each direction. In this way, various aims like beamforming, waveshaping and tailoring the radiation pattern can be well-served by modules that have been optimized in our study, simply fed by easy-to-find, weak and isotropic sources. Furthermore, ensembles of cylindrical metamaterial particles, within the framework of effective

medium theory, have been found to exhibit desirable electromagnetic features, such as tunable hyperbolic dispersion, double negative and epsilon-near-zero responses [72], [73]. The present work may be expanded to investigate the collective response of an ensemble of superradiating cylinders, offering insight into the behavior of the designs and extended tunability of their electromagnetic features. Finally, it would be interesting to expand this work to investigate the natural modes of the cylinders, in the framework of Mie theory. By systematically examining these modal characteristics, one can unveil additional functionalities and wave manipulation capabilities, such as selective enhancement, confinement, or directional emission.

Appendix A

Solution of the Scalar Helmholtz Equation

In order to solve the partial differential equation (3.17), we will utilize the method of separation of variables; we select two functions $R(r)$ and $F(\varphi)$ of the two independent variables r and φ respectively, such that $\psi(r,\varphi) = R(r)F(\varphi)$. Plugging this expression in (3.17), we obtain:

$$\frac{1}{r}\left[rR'(r)\right]'F(\varphi) + \frac{1}{r^2}R(r)F''(\varphi) + k^2R(r)F(\varphi) = 0 \tag{A.1}$$

where the prime symbol indicates differentiation with respect to r in the case of R and to φ in the case of F. Further algebraic manipulations yield:

$$\left(\frac{1}{r}R'(r)F(\varphi) + R''(r)F(\varphi) + k^2R(r)F(\varphi)\right) + \frac{1}{r^2}R(r)F''(\varphi) = 0. \tag{A.2}$$

By multiplying the above equation with $r^2/(R(r)F(\varphi))$, we arrive at:

$$\left(r^2\frac{R''(r)}{R(r)} + r\frac{R'(r)}{R(r)} + (kr)^2\right) + \left(\frac{F''(\varphi)}{F(\varphi)}\right) = 0. \tag{A.3}$$

We notice that the right hand side of (A.3) is independent of both r and φ. Additionally, the two terms inside the parentheses in the left hand side are functions of only one of the two independent variables respectively. Therefore, they should both be constant. We select:

$$\frac{F''(\varphi)}{F(\varphi)} = -n^2. \tag{A.4}$$

Since the solution we seek needs to be 2π-periodic with respect to φ, as a result of the structures being cylindrically symmetric, n should be an integer. Therefore, the functions F_n will be complex exponentials of the form $\exp(in\varphi)$, satisfying the periodicity condition. Substituting (A.4) in (A.3), we get the following differential equation that R should satisfy:

$$r^2R_n''(r) + rR_n'(r) + \left((kr)^2 - n^2\right)R_n(r) = 0. \tag{A.5}$$

The above equation is known as the Bessel equation of order n. Its solution is a linear combination of the Bessel function of the first kind and order n (J_n) and the Bessel function of the second kind and order n (Y_n) [62]. Therefore, the eigensolutions ψ_n

of the scalar Helmholtz equation, when a 2π-periodicity is imposed with respect to the azimuthal angle φ, read:

$$\psi_n(r,\varphi) = \left(A_n J_n(kr) + B_n Y_n(kr)\right) e^{\mathrm{i}n\varphi}, \quad n \in \mathbb{Z}. \tag{A.6}$$

To obtain the general solution, we observe that the differential operator $L = (\nabla^2 + k^2)$ appearing in (3.16) is linear; therefore, the general solution ψ may be found by superimposing all of the eigenfunctions ψ_n. As a result, the solution reads:

$$\psi(r,\varphi) = \sum_{n=-\infty}^{+\infty} \left(A_n J_n(kr) + B_n Y_n(kr)\right) e^{\mathrm{i}n\varphi}. \tag{A.7}$$

Appendix B

Analytical Solution and Calculation of the Total Field

In this section, we will give a detailed analysis of the analytical methods used to solve the various boundary value problems. This essential for finding the complex coefficients C_n used in the evaluation of the radiation enhancement ($P_{\text{rad}}/P_{\text{inc}} = \sum_{n=-\infty}^{+\infty} |C_n|^2$).

In Appendix A, we have solved the scalar Helmholtz equation in polar coordinates. This equation is satisfied by the z components of the fields. Therefore, when TM waves are considered we solve it for E_z, while in TE-excited setups we solve it for H_z. The critical point is selecting the types of Bessel functions in each region of the geometry, since various boundary conditions have to be satisfied. Additionally, the incident (background) field must be superimposed to the chosen eigensolution in the region the source is placed in, in order to satisfy the boundary condition (singularity) on the source.

We will now describe the eigensolutions selected in each region. Since the structures are cylindrically symmetric, we are only concerned with the in-plane position vector $\mathbf{r}$. In general, we do not want singularities to occur in points where no source is present. Additionally, we would like the field that is external to the source to have a form that corresponds to a cylindrical wave, travelling outwards towards infinity.

Let us suppose that $r \in D$, where $D \subseteq \mathbb{R}^2$. If $r = 0$ is present in this domain D, then we cannot select Y_n as a solution in D, since $Y_n(x \to 0) \to -\infty$, leading to a singularity. Therefore, in these internal domains that are of the $[0, g]$ form, a solution of the following form is selected:

$$\psi_{0\leq r\leq g}(k_0 r) = \sum_{n=-\infty}^{+\infty} A_n J_n(k_0 r) e^{\mathrm{i}n\varphi}. \tag{B.1}$$

Furthermore, in external domains ($D = [a, +\infty)$) the Hankel function of second order is selected, in order to represent a wave travelling to infinity (and thus satisfy the Sommerfeld radiation condition):

$$\psi_{0\leq r\leq g}(k_0 r) = \sum_{n=-\infty}^{+\infty} A_n H_n(k_0 r) e^{\mathrm{i}n\varphi}. \tag{B.2}$$

Finally, in domains of the form $D = [g, a]$, we can directly use A.7, since we do not have a singularity nor do we need to satisfy a radiation condition.

Using the above points, we will now give the form of the fields in the most complex of cases studied, which is depicted in Fig. 3.3(b), where we have three domains $[0, g]$, $[g, a]$ and $[a, +\infty]$ and the source is placed in the second one. We once again remind the reader that we use F to denote either E_z in the TM case of H_z in the TE one. We have:

$$F_{0\leq r\leq g^-} = \sum_{n=-\infty}^{+\infty} A_{1,n} J_n(k_0 r) e^{\mathrm{i}n\varphi}, \tag{B.3}$$

$$F_{g^+\leq r\leq a^-} = F_{\text{inc}} + \sum_{n=-\infty}^{+\infty} \left(A_{2,n} J_n(k_0 r) + B_{2,n} Y_n(k_0 r)\right) e^{\mathrm{i}n\varphi}, \tag{B.4}$$

$$F_{a^+\leq r} = \sum_{n=-\infty}^{+\infty} C_n H_n(k_0 r) e^{\mathrm{i}n\varphi}. \tag{B.5}$$

The fields are developed in a similar manner for other, less complex solutions. In the TM case, the corresponding magnetic field for each region is found by using the Faraday equation, while the electric field in the TE case is calculated using the Ampere-Maxwell equation.

Now, to calculate the unknown coefficients the boundary conditions discussed in Chapter 3 must be satisfied. After substituting the chosen solutions, we obtain a linear system of the form:

$$\mathbb{M}_n \cdot \mathbf{x}_n = \mathbf{b}_n, \tag{B.6}$$

where $\mathbb{M}_n$ is a square matrix, $\mathbf{x}_n$ is the unknown coefficient vector (for example, in the three-domain case given above, $\mathbf{x}_n = [A_{1,n}, A_{2,n}, B_{2,n}, C_n]^T$) and $\mathbf{b}$ is a vector resulting from the excitation, giving rise to the inhomogeneous system of linear equations. By solving this linear system, we have completely solved the electromagnetic problem, having found the fields in each domain of $\mathbb{R}^2$.

Bibliography

[1] C. A. Valagiannopoulos, "Arbitrary currents on circular cylinder with inhomogeneous cladding and RCS optimization", *J. Electromagn. Waves Appl.*, vol. 21, no. 5, pp. 665–680, Jan. 2007.

[2] M. Abramowitz and I. A. Stegun, Eds., *Handbook of Mathematical Functions* (Dover Books on Mathematics). Mineola, NY: Dover Publications, Jun. 1965.

[3] C. Valagiannopoulos, "Photonic inverse design of simple particles with realistic losses in the visible frequency range", *Photonics*, vol. 6, no. 1, p. 23, Feb. 2019.

[4] D. Tulegenov and C. Valagiannopoulos, "Meta-bubbles: Spherical metasurfaces as electromagnetic energy accumulators", *J. Appl. Phys.*, vol. 131, no. 9, p. 093 103, Mar. 2022.

[5] *COMSOL Multiphysics® v. 6.2*, `www.comsol.com`, COMSOL AB, Stockholm, Sweden.

[6] A. Abrashuly and C. A. Valagiannopoulos, "Photonic memory with nonlinear plasmonic nanotubes", *APL Mater.*, vol. 9, p. 101 111, 2021.

[7] C. A. Valagiannopoulos and S. A. Tretyakov, "Symmetric absorbers realized as gratings of pec cylinders covered by ordinary dielectrics", *IEEE Trans. Antennas Propag.*, vol. 62, no. 10, pp. 5089–5098, 2014.

[8] R. H. Dicke, "Coherence in spontaneous radiation processes", *Phys. Rev.*, vol. 93, pp. 99–110, 1 Jan. 1954.

[9] M. Gross and S. Haroche, "Superradiance: An essay on the theory of collective spontaneous emission", *Physics Reports*, vol. 93, no. 5, pp. 301–396, 1982.

[10] E. Jaynes and F. Cummings, "Comparison of quantum and semiclassical radiation theories with application to the beam maser", *Proceedings of the IEEE*, vol. 51, no. 1, pp. 89–109, 1963.

[11] J. C. MacGillivray and M. S. Feld, "Theory of superradiance in an extended, optically thick medium", *Phys. Rev. A*, vol. 14, pp. 1169–1189, 3 Sep. 1976.

[12] T. Brandes, "Coherent and collective quantum optical effects in mesoscopic systems", *Physics Reports*, vol. 408, no. 5, pp. 315–474, 2005.

[13] J. Pan, S. Sandhu, Y. Huo, *et al.*, "Experimental demonstration of an all-optical analogue to the superradiance effect in an on-chip photonic crystal resonator system", *Phys. Rev. B*, vol. 81, p. 041 101, 4 Jan. 2010.

[14] J. A. Mlynek, A. A. Abdumalikov, C. Eichler, and A. Wallraff, "Observation of dicke superradiance for two artificial atoms in a cavity with high decay rate", *Nat. Commun.*, vol. 5, no. 1, p. 5186, Nov. 2014.

[15] S. J. Masson and A. Asenjo-Garcia, "Universality of Dicke superradiance in arrays of quantum emitters", *Nat. Commun.*, vol. 13, no. 1, p. 2285, Apr. 2022.

[16] M. Scheibner, T. Schmidt, L. Worschech, *et al.*, "Superradiance of quantum dots", *Nat. Phys.*, vol. 3, no. 2, pp. 106–110, Feb. 2007.

[17] M. O. Scully and A. A. Svidzinsky, "The super of superradiance", *Science*, vol. 325, no. 5947, pp. 1510–1511, 2009.

[18] J. G. Bohnet, Z. Chen, J. M. Weiner, D. Meiser, M. J. Holland, and J. K. Thompson, "A steady-state superradiant laser with less than one intracavity photon", *Nature*, vol. 484, no. 7392, pp. 78–81, Apr. 2012.

[19] S. Kang, S. Jeong, W. Choi, *et al.*, "Imaging deep within a scattering medium using collective accumulation of single-scattered waves", *Nat. Photonics*, vol. 9, no. 4, pp. 253–258, Apr. 2015.

[20] R. Fleury and A. Alù, "Enhanced superradiance in epsilon-near-zero plasmonic channels", *Phys. Rev. B*, vol. 87, p. 201 101, 20 May 2013.

[21] P. Solano, P. Barberis-Blostein, F. K. Fatemi, L. A. Orozco, and S. L. Rolston, "Super-radiance reveals infinite-range dipole interactions through a nanofiber", *Nat. Commun.*, vol. 8, no. 1, Dec. 2017.

[22] D. Martin-Cano, L. Martin-Moreno, F. J. Garcia-Vidal, and E. Moreno, "Resonance energy transfer and superradiance mediated by plasmonic nanowaveguides", *Nano Letters*, vol. 10, no. 8, pp. 3129–3134, 2010.

[23] A. Goban, C.-L. Hung, J. D. Hood, *et al.*, "Superradiance for atoms trapped along a photonic crystal waveguide", *Phys. Rev. Lett.*, vol. 115, p. 063 601, 6 Aug. 2015.

[24] S. John and T. Quang, "Localization of superradiance near a photonic band gap", *Phys. Rev. Lett.*, vol. 74, pp. 3419–3422, 17 Apr. 1995.

[25] Y. Sonnefraud, N. Verellen, H. Sobhani, *et al.*, "Experimental realization of subradiant, superradiant, and Fano resonances in ring/disk plasmonic nanocavities", *ACS Nano*, vol. 4, no. 3, pp. 1664–1670, 2010.

[26] V. N. Pustovit and T. V. Shahbazyan, "Cooperative emission of light by an ensemble of dipoles near a metal nanoparticle: The plasmonic Dicke effect", *Phys. Rev. Lett.*, vol. 102, p. 077 401, 7 Feb. 2009.

[27] P. A. Huidobro, A. Y. Nikitin, C. Gonzalez-Ballestero, L. Martin-Moreno, and F. J. Garcia-Vidal, "Superradiance mediated by graphene surface plasmons", *Phys. Rev. B*, vol. 85, p. 155 438, 15 Apr. 2012.

[28] D. Dzsotjan, A. S. Sorensen, and M. Fleischhauer, "Quantum emitters coupled to surface plasmons of a nanowire: A Green's function approach", *Phys. Rev. B*, vol. 82, p. 075 427, 7 Aug. 2010.

[29] C. A. Valagiannopoulos and S. A. Tretyakov, "Theoretical concepts of unlimited-power reflectors, absorbers, and emitters with conjugately matched layers", *Phys. Rev. B*, vol. 94, p. 125 117, 12 Sep. 2016.

[30] C. A. Valagiannopoulos, M. S. Mirmoosa, I. S. Nefedov, S. A. Tretyakov, and C. R. Simovski, "Hyperbolic-metamaterial antennas for broadband enhancement of dipole emission to free space", *J. Appl. Phys.*, vol. 116, no. 16, p. 163 106, Oct. 2014.

[31] P. Retif, S. Pinel, M. Toussaint, *et al.*, "Nanoparticles for radiation therapy enhancement: The key parameters", *Theranostics*, vol. 5, no. 9, pp. 1030–1044, Jun. 2015.

[32] M. J. Maryanski, J. C. Gore, R. P. Kennan, and R. J. Schulz, "NMR relaxation enhancement in gels polymerized and cross-linked by ionizing radiation: A new approach to 3D dosimetry by MRI", *Magnetic Resonance Imaging*, vol. 11, no. 2, pp. 253–258, 1993.

[33] X. Huang, S. Neretina, and M. A. El-Sayed, "Gold nanorods: From synthesis and properties to biological and biomedical applications", *Adv. Mater.*, vol. 21, no. 48, pp. 4880–4910, Dec. 2009.

[34] W. U. Huynh, J. J. Dittmer, and A. P. Alivisatos, "Hybrid nanorod-polymer solar cells", *Science*, vol. 295, no. 5564, pp. 2425–2427, Mar. 2002.

[35] M. Caldarola, P. Albella, E. Cortés, *et al.*, "Non-plasmonic nanoantennas for surface enhanced spectroscopies with ultra-low heat conversion", *Nat. Commun.*, vol. 6, no. 1, p. 7915, Aug. 2015.

[36] M. H. Huang, S. Mao, H. Feick, *et al.*, "Room-temperature ultraviolet nanowire nanolasers", *Science*, vol. 292, no. 5523, pp. 1897–1899, Jun. 2001.

[37] W. Cai, U. K. Chettiar, A. V. Kildishev, and V. M. Shalaev, "Optical cloaking with metamaterials", *Nat. Photonics*, vol. 1, no. 4, pp. 224–227, Apr. 2007.

[38] D. Schurig, J. J. Mock, B. J. Justice, *et al.*, "Metamaterial electromagnetic cloak at microwave frequencies", *Science*, vol. 314, no. 5801, pp. 977–980, Nov. 2006.

[39] M. F. L. De Volder, S. H. Tawfick, R. H. Baughman, and A. J. Hart, "Carbon nanotubes: Present and future commercial applications", *Science*, vol. 339, no. 6119, pp. 535–539, Feb. 2013.

[40] J. Kong, N. R. Franklin, C. Zhou, *et al.*, "Nanotube molecular wires as chemical sensors", *Science*, vol. 287, no. 5453, pp. 622–625, Jan. 2000.

[41] C. P. Mavidis, A. C. Tasolamprou, E. N. Economou, C. M. Soukoulis, and M. Kafesaki, "Single scattering and effective medium description of multilayer cylinder metamaterials: Application to graphene- and to metasurface-coated cylinders", *Phys. Rev. B*, vol. 107, p. 134 120, 13 Apr. 2023.

[42] S. M. Kamali, A. Arbabi, E. Arbabi, Y. Horie, and A. Faraon, "Decoupling optical function and geometrical form using conformal flexible dielectric metasurfaces", *Nat. Commun.*, vol. 7, no. 1, p. 11 618, Sep. 2016.

[43] D. Yoo, T. W. Johnson, S. Cherukulappurath, D. J. Norris, and S.-H. Oh, "Template-stripped tunable plasmonic devices on stretchable and rollable substrates", *ACS Nano*, vol. 9, no. 11, pp. 10 647–10 654, Nov. 2015.

[44] M. Massaouti, A. A. Basharin, M. Kafesaki, *et al.*, "Eutectic epsilon-near-zero metamaterial terahertz waveguides", *Opt. Lett.*, vol. 38, no. 7, pp. 1140–1142, Apr. 2013.

[45] A. Reyes-Coronado, M. F. Acosta, R. I. Merino, *et al.*, "Self-organization approach for THz polaritonic metamaterials", *Opt. Express*, vol. 20, no. 13, pp. 14 663–14 682, Jun. 2012.

[46] G. Sun, J. B. Khurgin, and R. A. Soref, "Plasmonic light-emission enhancement with isolated metal nanoparticles and their coupled arrays", *J. Opt. Soc. Am. B*, vol. 25, no. 10, pp. 1748–1755, Oct. 2008.

[47] C. Guclu, T. S. Luk, G. T. Wang, and F. Capolino, "Radiative emission enhancement using nano-antennas made of hyperbolic metamaterial resonators", *Appl. Phys. Lett.*, vol. 105, no. 12, p. 123 101, Sep. 2014.

[48] A. Houard, Y. Liu, B. Prade, V. T. Tikhonchuk, and A. Mysyrowicz, "Strong enhancement of terahertz radiation from laser filaments in air by a static electric field", *Phys. Rev. Lett.*, vol. 100, p. 255 006, 25 Jun. 2008.

[49] A. Mekawy, H. Li, Y. Radi, and A. Alù, "Parametric enhancement of radiation from electrically small antennas", *Phys. Rev. Appl.*, vol. 15, p. 054 063, 5 May 2021.

[50] P. Biagioni, J.-S. Huang, and B. Hecht, "Nanoantennas for visible and infrared radiation", *Rep. Prog. Phys.*, vol. 75, no. 2, p. 024 402, Feb. 2012.

[51] E. B. Ureña, M. P. Kreuzer, S. Itzhakov, *et al.*, "Excitation enhancement of a quantum dot coupled to a plasmonic antenna", *Advanced Materials*, vol. 24, no. 44, pp. 314–320, 2012.

[52] E. Rusak, I. Staude, M. Decker, *et al.*, "Hybrid nanoantennas for directional emission enhancement", *Appl. Phys. Lett.*, vol. 105, no. 22, p. 221 109, Dec. 2014.

[53] M. S. Eggleston, K. Messer, L. Zhang, E. Yablonovitch, and M. C. Wu, "Optical antenna enhanced spontaneous emission", *Proc. Natl. Acad. Sci. U.S.A.*, vol. 112, no. 6, pp. 1704–1709, 2015.

[54] C. Huck, F. Neubrech, J. Vogt, *et al.*, "Surface-enhanced infrared spectroscopy using nanometer-sized gaps", *ACS Nano*, vol. 8, no. 5, pp. 4908–4914, 2014.

[55] H. Aouani, O. Mahboub, E. Devaux, H. Rigneault, T. W. Ebbesen, and J. Wenger, "Plasmonic antennas for directional sorting of fluorescence emission", *Nano Letters*, vol. 11, no. 6, pp. 2400–2406, 2011.

[56] G. Toscano, S. Raza, A.-P. Jauho, N. A. Mortensen, and M. Wubs, "Modified field enhancement and extinction by plasmonic nanowire dimers due to nonlocal response", *Opt. Express*, vol. 20, no. 4, pp. 4176–4188, Feb. 2012.

[57] T. B. Hoang, G. M. Akselrod, C. Argyropoulos, J. Huang, D. R. Smith, and M. H. Mikkelsen, "Ultrafast spontaneous emission source using plasmonic nanoantennas", *Nat. Commun.*, vol. 6, no. 1, p. 7788, Jul. 2015.

[58] A. Rakovich, P. Albella, and S. A. Maier, "Plasmonic control of radiative properties of semiconductor quantum dots coupled to plasmonic ring cavities", *ACS Nano*, vol. 9, no. 3, pp. 2648–2658, 2015.

[59] S. Arslanagic, Y. Liu, R. Malureanu, and R. W. Ziolkowski, "Impact of the excitation source and plasmonic material on cylindrical active coated nanoparticles", *Sensors (Basel)*, vol. 11, no. 9, pp. 9109–9120, Sep. 2011.

[60] R. W. Ziolkowski and E. Heyman, "Wave propagation in media having negative permittivity and permeability", *Phys. Rev. E*, vol. 64, p. 056 625, 5 Oct. 2001.

[61] F. Zolla, S. Guenneau, A. Nicolet, and J. B. Pendry, "Electromagnetic analysis of cylindrical invisibility cloaks and the mirage effect", *Opt. Lett.*, vol. 32, no. 9, pp. 1069–1071, May 2007.

[62] W. C. Chew, *Waves and Fields in Inhomogenous Media* (IEEE Press Series on Electromagnetic Wave Theory). Piscataway, NJ: IEEE Publications, Jan. 1999.

[63] J. D. Jackson, *Classical Electrodynamics*, 3rd ed. Nashville, TN: John Wiley & Sons, May 2021.

[64] C. A. Balanis, *Advanced Engineering Electromagnetics*, 2nd ed. Chichester, England: John Wiley & Sons, Jan. 2012.

[65] C. Pfeiffer and A. Grbic, "Metamaterial Huygens' surfaces: Tailoring wave fronts with reflectionless sheets", *Phys. Rev. Lett.*, vol. 110, p. 197 401, 19 May 2013.

[66] G. N. Watson, *A Treatise on the Theory of Bessel Functions* (Cambridge mathematical library), 2nd ed. Cambridge, England: Cambridge University Press, Aug. 1995.

[67] C. A. Balanis, *Antenna Theory*, 4th ed. Hoboken, NJ: Wiley-Blackwell, Jan. 2016.

[68] C. Zhang, S. Divitt, Q. Fan, *et al.*, "Low-loss metasurface optics down to the deep ultraviolet region", *Light Sci. Appl.*, vol. 9, p. 55, 2020.

[69] Y. Gao, "Low-loss metasurfaces based on discretized metaatoms", *Commun. Phys.*, vol. 7, p. 320, 2024.

[70] M. I. Shalaev, J. Sun, A. Tsukernik, A. Pandey, K. Nikolskiy, and N. M. Litchinitser, "High-efficiency all-dielectric metasurfaces for ultracompact beam manipulation in transmission mode", *Nano Letters*, vol. 15, no. 9, pp. 6261–6266, 2015.

[71] T. Debogovic and J. Perruisseau-Carrier, "Low loss mems-reconfigurable 1-bit reflectarray cell with dual-linear polarization", *IEEE Trans. Antennas Propag.*, vol. 62, no. 10, pp. 5055–5060, 2014.

[72] C. P. Mavidis, A. C. Tasolamprou, E. N. Economou, C. M. Soukoulis, and M. Kafesaki, "Polaritonic cylinders as multifunctional metamaterials: Single scattering and effective medium description", *Phys. Rev. B*, vol. 102, p. 155 310, 15 Oct. 2020.

[73] C. P. Mavidis, A. C. Tasolamprou, E. N. Economou, C. M. Soukoulis, and M. Kafesaki, "Single scattering and effective medium description of multilayer cylinder metamaterials: Application to graphene- and to metasurface-coated cylinders", *Phys. Rev. B*, vol. 107, p. 134 120, 13 Apr. 2023.